

UNIVERSIDADE DE SÃO PAULO  
ESCOLA DE ENGENHARIA DE SÃO CARLOS  
DEPARTAMENTO DE ENGENHARIA ELÉTRICA E COMPUTAÇÃO  
PROGRAMA DE PÓS-GRADUAÇÃO EM ENGENHARIA ELÉTRICA

JAVIER AUGUSTO JURADO MONCADA

Aplicação da técnica de contraste de fase da ordem zero na geração de  
pinças ópticas multi-feixe

SÃO CARLOS

2017



JAVIER AUGUSTO JURADO MONCADA

Aplicação da técnica de contraste de fase da ordem zero na geração de pinças ópticas multi-feixe

Mestre em Ciências, Programa de Engenharia Elétrica.

Área de Concentração: Telecomunicações

Orientador: Prof. Dr. Luiz Gonçalves Neto

**Trata-se da versão corrigida da dissertação. A versão original se encontra disponível na EESC/USP que aloja o programa de Pos-Graduação de Engenharia Elétrica.**

SÃO CARLOS

2017

AUTORIZO A REPRODUÇÃO TOTAL OU PARCIAL DESTE TRABALHO,  
POR QUALQUER MEIO CONVENCIONAL OU ELETRÔNICO, PARA FINS  
DE ESTUDO E PESQUISA, DESDE QUE CITADA A FONTE.

JJ96a Jurado Moncada, Javier Augusto  
Aplicação da técnica de contraste de fase da ordem  
zero na geração de pinças ópticas multi-feixe / Javier  
Augusto Jurado Moncada; orientador Luiz Gonçalves  
Neto. São Carlos, 2017.

Dissertação (Mestrado) - Programa de Pós-Graduação  
em Engenharia Elétrica e Área de Concentração em  
Telecomunicações -- Escola de Engenharia de São Carlos  
da Universidade de São Paulo, 2017.

1. pinças ópticas. 2. óptica de Fourier. 3.  
contraste de fase. 4. modulador espacial de luz. I.  
Título.

## FOLHA DE JULGAMENTO

Candidato: Bacharel **JAVIER AUGUSTO JURADO MONCADA**.

Título da dissertação: "Aplicação da técnica de contraste de fase da ordem zero na geração de pinças ópticas multifeixe".

Data da defesa: 23/11/2017.

### Comissão Julgadora:

### Resultado:

Prof. Associado **Luiz Gonçalves Neto**  
**(Orientador)**  
(Escola de Engenharia de São Carlos/EESC)

Aprovado

Prof. Dr. **Sérgio Ricardo Muniz**  
(Instituto de Física de São Carlos/IFSC-USP)

Aprovado

Prof. Dr. **José Carlos Pizolato Junior**  
(Universidade Federal de São Carlos/UFSCar)

Aprovado

Coordenador do Programa de Pós-Graduação em Engenharia Elétrica:  
Prof. Associado **Luís Fernando Costa Alberto**

Presidente da Comissão de Pós-Graduação:  
Prof. Associado **Luís Fernando Costa Alberto**



## AGRADECIMENTOS

---

A realização deste objetivo profissional e acadêmico é o resultado não somente do meu trabalho, mas também do apoio inabalável de várias pessoas que de uma forma ou outra fizeram parte deste projeto.

Agradeço ao Prof. Luiz pela orientação do meu mestrado, e por ter compartilhado comigo a sua sabedoria acadêmica e em questões da vida.

À minha mãe, Cruz Marina, e às minhas irmãs, Daniela e Vicky, por estarem sempre comigo apesar da distância.

À minha esposa, Maria, pela paciência e companheirismo tanto nos melhores quanto nos mais difíceis momentos.

Ao meu colega e amigo, Fabriciu, pelo bom humor e pelas conversas que sempre fizeram o meu trabalho no laboratório mais agradável.

Aos meus colegas do Departamento de Telecomunicações, Talita e Augusto, por sempre estarem dispostos a ajudar.

Aos meus colegas do LAT, pelo agradável ambiente de trabalho.

Ao Prof. Sérgio Muniz e Charlie Oncebay, pelo apoio técnico e pela confiança.

Ao CEPOF, pelo apoio financeiro que fez possível a minha participação em eventos internacionais.



*“There are two goddesses in your heart. The Goddess of Wisdom and the Goddess of Wealth. Everyone thinks they need to get wealth first, and wisdom will come. So they concern themselves with chasing money. But they have it backwards. You have to give your heart to the Goddess of Wisdom, give her all your love and attention, and the Goddess of Wealth will become jealous, and follow you.”*

*-Joe Vigil*



JURADO, Javier. **Aplicação da técnica de contraste de fase da ordem zero na geração de pinças ópticas multi-feixe.** 96 páginas. Dissertação de Mestrado. Escola de Engenharia de São Carlos, 2017.

Um sistema multi-feixe de pinças ópticas baseado na técnica de contraste de fase da ordem zero pode apresentar vantagens significativas sobre sistemas mecanicamente complexos e sensíveis ao alinhamento, e sobre tecnologias que, apesar de serem similares, requerem a customização de componentes ópticos. Porém, ao nosso conhecimento, este sistema até agora não tem sido implementado experimentalmente. Neste trabalho tem-se desenvolvido, como prova de princípio, o primeiro sistema baseado na técnica de contraste de fase da ordem zero gerador de múltiplas pinças ópticas. Esta técnica da óptica de Fourier utiliza conceitos do contraste de fase de Zernike e técnicas de codificação de dois pixels para gerar padrões de intensidade no plano da imagem que são diretamente relacionados a distribuições de fase no plano de entrada do sistema, o qual é formado por um modulador espacial de luz (SLM). Esta dissertação de mestrado descreve detalhadamente os passos tomados com o propósito de utilizar os campos estruturados de luz gerados pelo sistema de contraste de fase da ordem zero para aprisionar esferas de 2  $\mu\text{m}$  de diâmetro de sílica fundida. Neste trabalho apresentamos os fundamentos teóricos do aprisionamento óptico e da técnica de contraste de fase da ordem zero, seguidos pela implementação de experimentos independentes em cada modalidade, e finalmente apresentamos a integração de ambos os sistemas dentro um sistema único de pinças ópticas multi-feixe. Apesar da baixa eficiência óptica do sistema, foi possível implementar um sistema de pinças ópticas duplas. Finalizamos o nosso trabalho na discussão detalhada das limitações do nosso arranjo óptico e comentamos sobre potenciais melhorias para aumentar a rigidez das pinças ópticas e a qualidade geral do sistema.

**Palavras-chave:** pinças ópticas, óptica de Fourier, contraste de fase, modulador espacial de luz.



## ABSTRACT

---

JURADO, Javier. **Application of the zero order phase contrast technique in the generation of multi-beam optical traps.** 96 pages. Master's dissertation. São Carlos School of Engineering, University of São Paulo, 2017.

A multi-beam optical trapping system based on the zero order phase contrast technique may offer significant advantages over mechanically-complex, alignment-sensitive optical trapping systems, and over technologies that, though similar, require the customization of optics components. However, to our knowledge, such a system has not been yet implemented experimentally. We have developed, as a proof of principle, what we think is the first system based on the zero order phase contrast technique to successfully generate multiple optical traps. This Fourier optics technique makes use of existing concepts of Zernike phase contrast and two-pixel encoding techniques to generate intensity patterns in the image plane that are directly related to phase distributions in the input plane, which is comprised by a spatial light modulator (SLM). This master's dissertation describes in detail the steps taken towards using the structured light fields generated by a zero order phase contrast system to trap 2  $\mu\text{m}$  diameter fused silica beads. We present the theoretical foundations of optical trapping and the zero order phase contrast technique, followed by the implementation of independent laboratory experiments in each modality, and finally integrate both systems into a single optical setup for multi-beam trapping. In spite of the low optical efficiency of the system, we were able to implement dual optical traps. We finalize by discussing in detail the limitations of our experimental setup in and comment on potential improvements to increase the stiffness of the optical traps and the overall quality of the system.

**Keywords:** optical tweezers, Fourier optics, phase contrast, spatial light modulator.



## LIST OF FIGURES

---

- Figure 2.1. Illustration of acceleration of a particle in a glass cell of thickness  $t = 120 \mu\text{m}$ . The forward propagation of the particles generated by the focused laser light is observed through a microscope (M) (Ashkin, 1970)..... 8
- Figure 2.2. Ray optics portrayal of the net force on a transparent dielectric particle as a result of the light intensity gradient (shown in red). An optical intensity gradient concentrated to the right causes the particle in (a) to experience a net force (depicted in yellow arrows) to the right and slightly down. The particle in (b), experiences a net force towards the focus of the beam as a result of the radial intensity profile (Neuman; Block, 2004). ..... 9
- Figure 2.3. Map of regimes of validity of methods for computing the scattering of light by particles based on their size and refractive index. The typical size of the particles used in optical trapping experiments falls outside the domain of approximate methods, requiring direct solution of either Maxwell equations or the vector Helmholtz equation (Nieminen et al., 2007a)..... 10
- Figure 2.4. Changes in momentum flux of a trapping beam depending on the location of the lens. (a) When located at the center of the focus, the lens does not cause momentum flux changes in the trapping beam. (b) A reaction force in the direction of propagation results when the particle is located above the beam focus. (c) If the lens is located after the focus, it increases the momentum flux of the beam, resulting in a reaction force towards the focus. (d) A reaction force directed towards the beam axis results when the particle is displaced sideways (Nieminen et al. 2007a). ..... 12
- Figure 2.5. Geometry for calculating the force due to scattering of a single ray of power  $P$  incident on a dielectric sphere at an angle  $\theta$ . The reflected ray is represented by  $PR$  and refracted rays are represented by  $PT^2R^n$  (Ashkin, 1992)..... 13
- Figure 2.6. Values for the gradient force quality factors  $Q_s$ ,  $Q_g$  and  $Q_{mag}$  ( $Q_s + Q_g$ ) for a single ray incident on a dielectric sphere of  $n_p = 1.2$  at angle  $\theta$ .  $Q_{grad}$  values of  $\sim 0.5$  are generated at incidence angles around  $70^\circ$  (Ashkin, 1992). ..... 13
- Figure 3.1. Intensity distribution generation in a  $4f$  optical system using a Fourier filter (Adapted from Glückstad; Palima, 2009)..... 16
- Figure. 3.2. Image of living tissue culture using (a) phase contrast microscopy and (b) brightfield microscopy (Zernike, 1955)..... 16
- Figure. 3.3. Pixel representation used in the zero order phase contrast technique. (a) Geometry of a DOE composed by a matrix of  $M \times N$  pixels of size  $X \times Y$ , each with active area  $a \times b$ . (b) DOE geometry using macropixels of size  $X \times 2Y$ . Each white

subpixel is modulated by the information contained in  $a(x,y)$ , and the subpixels represented in gray color are modulated by  $e^{j\pi}$  .....18

Figure 3.4. Computational simulation of a zero-order filter. (a) Image of letter A and mesh to simulate the finite dimension of the LCTV pixels (512x512). (b) Image of the Fourier spectrum of (a). Notice the periodic peaks due to the FT of the mesh distribution. They represent the different orders of diffraction that arise from the pixelated configuration of the DOE. (c) Plot of the Fourier spectrum. (d) Zero-order filter applied to Fourier transform of (a). (e) Plot of Fourier spectrum after application of filter. Only the zero-order frequency passes through the filter. (f) Filtered image after inverse Fourier transform. ....23

Figure 3.5. Simulation of the effect of the *sinc* functions on the diffraction pattern generated by the LCTV (adapted from BANYAL; PRASAD, 2005). ....26

Figure 3.6. The different molecular organizations of (a) nematic, (b) smectic, and (c) cholesteric liquid crystals (Goodman, 2004). ....28

Figure 3.7. (a) Molecule orientation in a twisted nematic crystal with twist angle  $\theta=90^\circ$ . The outermost LCs, in contact with the alignment layers (shown in (b)), determine the overall orientation of the crystals. The conducting layers are illustrated in (b) (Saleh; Teich, 1991; Goodman, 2004). ....28

Figure 3.8. Liquid crystal molecule in tilted state.....30

The effective extraordinary index of refraction  $n_e(\zeta)$ , is given by: .....30

Figure 3.9. Polarizer-LCTV-analyzer sandwich configuration . The angles  $\psi_1$ ,  $\psi_D$ , and  $\psi_2$  correspond to the orientations with respect to the x-axis of the polarizer, the molecular director of the LCTV, and the analyzer, respectively (Neto et al., 1996).31

Figure 4.1. Basic schematic of the IFTA. The optical Fourier transform perform by the microscope objective connect the hologram and trapping planes. The FFT is used to numerically iterate between both planes (Woerdemann, 2012). ....34

Figure 4.2. Experimental setup of HOT. The phase hologram is relayed to the back aperture of a microscope objective, which then tightly focuses the intensity distribution in order to trap 1.5 um diameter spheres in water (Grier; Roichman, 2006). ....34

Figure 4.3. Two views of a rotating icosahedron of colloidal spheres (Grier; Roichman, 2006).35

Figure 4.4. A pentagonal pattern of 26 colloidal silica spheres of 0.99  $\mu\text{m}$  in diameter is dynamically transformed into a circular pattern. (a) Original configuration. (b) After 16 steps. (c) Final configuration after 38 steps (Curtis et al., 2012). ....35

Figure 4.5. Reconstructed optical trapping pattern from a binary hologram produced at the Telecommunications lab at the EESC. The strong central peak corresponds to undiffracted light from the LCTV. The twin image is generated by the presence of complex conjugate of the original trapping pattern. ....36

Figure 4.6. Spatial filtering of undiffracted central beam in a HOT system. (a) System with collimated laser input. (b) System with slightly converging beam. Notice how the focal point is displaced from the higher mode planes and the change in the profile at the sample plane. (c) Blocking of the central mode (Polin et al. 2005).....	36
Figure 4.7. Experimental setup for the simultaneous trapping of high and low-index particles. Arbitrary phase patterns are encoded onto the SLM, and a high-contrast intensity pattern is observed in the image plane (IP). A standard inverted brightfield is used to trap and observe the particles (Glückstad; Palima, 2009).....	39
Figure 4.8. (a) High-contrast intensity pattern at the IP for high and low-index particles. (b) Nearly top-hat profile used for trapping high-index particles, and (c) doughnut profile for trapping low-index particles (Glückstad; Palima, 2009).....	39
Figure 4.9. Optical steering of hollow soda lime glass spheres with a doughnut-shaped beam. The arrow indicates the user-controlled displacement of the particle at each frame. Scale bar: 10 $\mu\text{m}$ (Glückstad; Palima, 2009).....	40
Figure 4.10. Image sequence showing dynamic rotation of six and two-fold trapping geometries using the GPC technique. The outer six spheres rotate clockwise 1/8 of a full rotation while the inner two spheres rotate counter-clockwise nearly one full rotation (Eriksen et al., 2002b).....	40
Figure 5.1. Schematic of optical path used to implement a single optical trap in the Telecommunications lab at the EESC. The laser beam bounces off a 45° mirror (M) and is expanded by lenses L1 (50 mm EFL) and L2 (250 mm EFL). After passing through an iris (I), the laser beam is coupled into the microscope by the beamsplitter (BS) and focused in the trapping plane by the microscope objective (MO). The tube lens (L3) focuses the light returning through the objective, and a shortpass filter (F) filters out any light in the red spectrum before reaching the CCD camera.....	44
Figure 5.2. Experimental setup of optical path used to implement a single optical trap in the Telecommunications lab at the EESC. ....	45
Figure 5.3. Close-up of microscope setup used in single optical trapping experiments. Light from the laser can be seen being focused onto the sample plane by the microscope objective.....	45
Figure 5.4. Sample preparation kit purchased from Thorlabs Inc. used in optical trapping experiments (Image taken from <a href="http://www.thorlabs.com">www.thorlabs.com</a> , 2017.) .....	46
Figure 5.5. (A) 20x image of (b) Seiko-Epson LCTV used in the zero order phase contrast experiments. The LCTV panel measures 1.32 inches (3.4 cm) diagonally, containing 480 pixels in the horizontal direction, and 440 pixels in the vertical direction.. The center-to-center spacing between each pixel is 45 $\mu\text{m}$ vertically by 55 $\mu\text{m}$ horizontally, for an active area of 33%. ....	47

- Figure 5.6. Optical arrangement for measuring phase difference between two gray levels using a wedge shear plate interferometer. Coherent light uniformly illuminates the LCTV, onto which regions with different gray levels have been programmed (0 and 125, respectively). Upon incidence on the interferometer, light passing through the different regions interferes in the central part of the interferometer due to the double reflection of the optical element. By measuring the shift between regions a and b, the phase difference between both gray levels can be inferred (Neto, 1995). .....50
- Figure 5.7. Wedged shear plate interferometer (WSPI) used for measuring the phase modulation range of our LCTV. The top diffused window is used for viewing the interference pattern generated after laser light is reflected from the front and back surfaces of the WSPI after passing through the Polarizer-LCTV-Analyzer sandwich.....50
- Figure 5.8. Experimental setup of the zero order phase contrast technique. The output from the laser is spatially filtered using a 40x microscope objective (MO1) and a 25 $\mu$ m pinhole (SF). Lens L1 collimates and uniformly distributes the light input onto the LCTV. The phase-modulated light of the LCTV is spatially filtered by the zero order filter ZOF in the Fourier plane of the 4f correlator formed by lenses L2 and L3, producing intensity distributions in the image plane that can be recorded using a CCD camera. Polarizers P1 and P2 are used to maximize the phase modulation of the LCTV. ....52
- Figure 5.9. Experimental setup of the zero order phase contrast technique in the Telecommunications lab at the EESC. The zero order filter (ZOF) is located in back focal point of the first 4f correlator lens L2. The imaging plane is located a focal distance away from lens L3.....52
- Figure 5.10. Image coded into LCTV for implementation of the zero order phase contrast technique. Every other row in the image has the gray level value corresponding to the phase modulation  $exp(j\pi)$ . Size of image: 640 x 480 pixels.....53
- Figure 5.11. Optical path for optical trapping system based on the zero order phase contrast technique. The intensity distributions generated by the phase contrast system are coupled by lens L3 and dichroic mirror DM into an adapted upright microscope for projection onto the sample plane. ....55
- Figure 5.12. Experimental setup of the integrated zero order phase contrast and optical tweezers system. The laser source is not shown. The laser output from collimator COL (left side of figure) is directed into the zero order phase contrast system by mirror M. The 4f correlator is formed by the LCTV, L1, and L2. The zero order filter ZOF is located in the back focal plane of L1. ....56
- Figure 5.13. Adapted microscope setup for optical trapping. The output from the phase contrast system is coupled from the left onto the dichroic mirror (DM) fixed on a tip/tilt mount for alignment. The sample holder is adjusted vertically in order to

position the sample in the focal volume of the light focused by the microscope objective (MO).....	57
Figure 5.14. The butterfly type, fiber coupled laser source, shown mounted on the top left side, is driven by stand-alone current and temperature controllers. ....	57
Figure 5.15. Dual pattern used in most trapping experiments (640 x 480 pixels). The diameter of each dot is 18 pixels. (a) Original image. (b) Image projected onto LCTV.....	58
Figure 5.16. (a) 3-dot and (b) 4-dot patterns projected in trapping experiments (640 x 480 pixels). ....	58
Figure 6.1. Sequential optical results for single optical trap using 60x, 0.85 NA microscope objective. The particle is trapped in (a). Upon briefly blocking the trapping beam path the particle is released from the trap in (b), allowing visualization of the focal spot of the trapping beam. The trap exerts a transversal force onto the particle within a limited range of the laser focus, bringing the free particle (c) back towards the optical tweezer field, trapping the particle again (d).....	60
Figure 6.2. Non-sequential optical results for single optical trap using 100x, 1.3 NA microscope objective. The particles are brought close to the laser focus by gently tapping on the sample slide. The laser focus can be observed in (a) and (b). In (c), two particles are trapped in the laser focus field. ....	61
Figure 6.3. Optical setup for qualitative evaluation of single trap stiffness as a function of power at the sample plane. By rotating polarizer P from 0° to 80°, the power at the sample plane was adjusted. The trap stiffness was evaluated at several power levels.....	62
Figure 6.4. The power measurements at the sample plane were performed using a beam profiler (P/N BP209-VIS, Thorlabs Inc, New Jersey, USA) placed at the focus of the microscope objective (MO in Figure 6.3). It was necessary to remove the sample stage in order to collect the data. ....	63
Figure 6.5. Qualitative results for trap stiffness as a function of power available at the sample plane. Measurements in the green gradient field are considered to imply stable optical trapping. The observed stiffness of the optical trap was somewhat constant in the yellow-orange power range (0.70-2.30 mW), albeit with some mechanical jitter. Trap stiffness falls sharply at power values below 0.50 mW. ....	64
Figure 6.6. Quality factors for the asymmetrical (a) axial (z-direction) and symmetrical (b) radial (x-direction) forces as functions of particle position for 60x optical trapping system. Calculated from (Nieminen et al. 2007b) .....	66
Figure 6.7. Normalized transmission curves for gray levels between 0 and 175. The orientations of the polarizer and analyzer were set parallel to each other and rotated simultaneously. The dashed lines correspond to the angles $\Psi_{max} = 42^\circ$ and $\Psi_{min} = 90^\circ$ .....	67

Figure 6.8. $T_{min}/T_{max}$ vs. gray level. The dashed line at gray level indicates the gray level at which $\gamma=n\pi$ .	68
Figure 6.9. Determination of twist angle $\alpha$ . The y-intercept value of 88 corresponds to the twist angle.	68
Figure 6.10. Phase modulation curve for LCTV used in our experiments with a 633 nm HeNe laser source. The input and output polarizer angles were aligned at $-10^\circ$ and $117^\circ$ , respectively, for phase-mostly modulation.	69
Figure 6.11. WSPI image for gray scale levels 0 and 255. There is considerable distortion of the fringes due to spherical aberration from the lens system. With a measured fringe period of 4.52 mm and a fringe displacement of 3.34 mm, the resulting relative phase between the two gray scale levels is 4.64 rad.	70
Figure 6.12. Zero order phase contrast results for image of cat (640 x 480 pixels). (a) Original GSL image. (b) Macropixel configuration image used for modulation of LCTV. (c) Optical result captured with CCD camera.	71
Figure 6.13. Zero order phase contrast results for image of woman (640 x 480 pixels). (a) Original GSL image. (b) Macropixel configuration image used for modulation of LCTV. (c) Optical result captured with CCD camera.	72
Figure 6.14. Zero order phase contrast results for image of 2-trap pattern (640 x 480 pixels). (a) Original binary image. (b) Macropixel configuration image used for modulation of LCTV. (c) Optical result captured with CCD camera.	73
Figure 6.15. Zero order phase contrast results for image of 8-trap pattern (640 x 480 pixels). (a) Original binary image. (b) Macropixel configuration image used for modulation of LCTV. (c) Optical result captured with CCD camera.	74
Figure 6.16. Diffraction pattern generated by the LCTV used in our experiments projected onto an infrared-sensitive card. Energy is lost to higher diffraction orders due to the mesh structure of the LCTV.	75
Figure 6.17. Optical trapping plane images collected by CCD camera of dual beam patterns without and with macropixelation. It is clear that pattern (b) displays the most contrast between the background and the actual structured light patterns.	76
Figure 6.18. (a) three and (b) four dot pattern projections on trapping plane.	77
Figure 6.19. Implementation of weak trapping of two 2 $\mu\text{m}$ beads. The trapping laser is turned off from (a)-(c). After laser turn-on, the beads slowly align with the trapping field in (d)-(i). The laser is turned off again and the beads dissipate in the sample through Brownian motion.	78
Figure 6.20. Response of two 2 $\mu\text{m}$ particles to dual trapping field. (a) Laser is off at $t = 0.0$ s. Upon turning on the laser, the particle on the left is pulled towards the trapping field in (b)-(g). Though unstably trapped, both particles maintain their overall positions (i)-(n) until the laser is turned off at (o).	79

Figure 6.21. Ghost trap (in red) resulting from narrowing of Gaussian distribution of trapping laser. The green circles denote the location of the fields generated by the zero order phase contrast technique.....	80
Figure A.1. Huygens envelope construction of secondary wavelets originated from a primary wavefront (Goodman, 2004).....	89
Figure A.2. Diffraction geometry used to define the Huygens-Fresnel principle (Goodman, 2004).....	90
Figure A.3. Optical path with diffractive element located a distance $d$ in front of lens.....	92



## LIST OF TABLES

---

Table 6.1. Measured zero order efficiency for images obtained in the zero order phase contrast technique.....	75
---------------------------------------------------------------------------------------------------------------	----



## LIST OF ACRONYMS AND ABBREVIATIONS

---

<b>AC</b>	Alternating Current
<b>CCD</b>	Charge Coupled Device
<b>CGH</b>	Computer Generated Holograms
<b>CPI</b>	Common Path Interferometer
<b>CRT</b>	Cathode Ray Tube
<b>CW</b>	Continuous Wave
<b>DNA</b>	Deoxyribonucleic Acid
<b>DOE</b>	Diffraction Optical Element
<b>DPSS</b>	Diode Pumped Solid State
<b>EFL</b>	Effective Focal Length
<b>FC/APC</b>	Fiber-optic Connector / Angled Physical Contact
<b>FFT</b>	Fast Fourier Transform
<b>GPC</b>	Generalized Phase Contrast
<b>GSL</b>	Gray Scale Level
<b>HeNe</b>	Helium Neon
<b>HOT</b>	Holographic Optical Trap
<b>HWP</b>	Half Wave Plate
<b>IFTA</b>	Iterative Fourier Transform Algorithm
<b>LC</b>	Liquid Crystal
<b>LCTV</b>	Liquid Crystal Television
<b>NA</b>	Numerical Aperture
<b>SBP</b>	Space Bandwidth Product
<b>SLM</b>	Spatial Light Modulator
<b>SRW</b>	Synthetic Reference Wave
<b>TFT</b>	Thin Film Transistor
<b>UV</b>	Ultra Violet
<b>VCSEL</b>	Vertical Cavity Surface Emitting Laser
<b>VGA</b>	Video Graphics Array
<b>VSFW</b>	Vector Spherical Wavefunction
<b>WSPI</b>	Wedge Shear Plate Interferometer



# TABLE OF CONTENTS

---

1 INTRODUCTION.....	1
1.1. Motivation.....	3
1.2. Objectives .....	3
1.3. Organization.....	4
2 OPTICAL TRAPPING .....	7
2.1. Historical Background .....	7
2.2. Optical Trapping Theory .....	9
3 THE ZERO ORDER PHASE CONTRAST TECHNIQUE.....	15
3.1. Theory of the Zero Order Phase Contrast Technique .....	17
3.2. Efficiency of the Zero Order Phase Contrast Technique .....	23
3.3. Considerations for Determining the Size of the Zero Order Filter .....	24
3.4. Use of SLM as the Input DOE in the Zero Order Phase Contrast Technique .....	27
3.4.1 Properties of Liquid Crystals.....	27
3.4.2. Effect of the Applied Voltage on the Index of Refraction of the LC Cell .....	29
3.4.3. Mathematical Modeling of the Polarizer-LCTV-Analyzer Optical Path.....	31
4 STATE OF THE ART.....	33
4.1. Holographic Optical Trapping (HOT) .....	33
4.2. The Generalized Phase Contrast Technique (GPC) in Optical Trapping .....	37
5 METHODS AND MATERIALS .....	43
5.1. Single Optical Trap .....	43
5.2. Characterization of the Liquid Crystal Television.....	47
5.3. The Zero Order Phase Contrast Technique.....	51
5.4. Integration of the Zero Order Phase Contrast Technique in Optical Trapping System.....	54
6 RESULTS.....	59
6.1. Single Optical Trap .....	59
6.1.1. Qualitative Evaluation of Trapping Stiffness as a Function of Laser Power .....	62
6.1.2. Quality Factor of the Forces Acting on a Micro-Particle near the Beam Focus .....	65
6.2. Characterization of Liquid Crystal Television.....	67
6.3. Optical Results of the Zero Order Phase Contrast Technique .....	71
6.4. Integration of the Zero Order Phase Contrast Technique in Optical Trapping System.....	76

7 DISCUSSION AND CONCLUSIONS .....	81
7.1. Discussion .....	81
7.2 Conclusions and Future Perspectives .....	84
BIBLIOGRAPHY .....	85
APPENDIX 1: PROJECTION OF A FRAUNHOFER DIFFRACTION PATTERN USING A FOURIER LENS.....	89
A.1. Mathematical Expression of the Huygens-Fresnel Principle .....	89
A.2. The Fresnel Approximation.....	90
A.3.The Fraunhofer Approximation.....	91
A.4. Projection of a Fraunhofer Diffraction Pattern using a Fourier Lens.....	91
APPENDIX 2: JONES MATRIX CALCULUS OF A LIQUID CRYSTAL CELL .....	95

# 1 INTRODUCTION

Optical trapping, also referred to as optical tweezers, laser tweezers, or optical micromanipulation (Woerdemann, 2012), is a technique that encompasses a great number of methods for manipulating particles ranging in size from tens of nanometers up to the micron scale domain (Ashkin, 1986; Neuman; Block, 2004; Nieminen et al., 2007a). Stemming from experimental and theoretical research by Arthur Ashkin in the 1970s and 1980s in acceleration and trapping of micron-sized particles by radiation pressure (Ashkin, 1970; Ashkin et al., 1986), this technique relies on the force exerted on a dielectric particle due to the transfer of momentum from the scattering of incident photons originating from a tightly focused laser beam. A force known as the gradient force, acting in the opposite direction of the axial scattering force, is responsible for trapping the particle within a radiation well. Thus, a stable trap in all three dimensions requires that the axial component of the force pulling the particle towards the focal region of the laser exceed the scattering force component pushing it away in the direction of light propagation (Neuman; Block, 2004). Dispensing with the need for physical contact, optical trapping has proven itself very useful in the non-invasive manipulation of particles ranging from plastic spheres to complex structures such as DNA strands, protein fibers, and other cell organelles, making it a versatile, practical tool in many applications (Grier, 2003). Moreover, the relative ease with which an optical trapping path can be integrated into a microscopy system makes it a very attractive technique across many experimental disciplines.

As a natural extension to single-beam optical traps, multi-beam traps have become very useful in situations in which arrays of particles need to be trapped simultaneously and, in some cases, controlled independently. These traps are accomplished in a number of ways. One of them is by assembling time-shared traps with optics such as beam-steering mirrors (Visscher; Brakenhoff; Krol, 1993; Fällman; Axner, 1997), or with acousto-optical deflectors (Visscher; Gross; Block, 1996). According to Padgett et al. (2010, p. 381) a single laser beam shared between many traps is indistinguishable from a true multi-beam trap as long as the refresh rate of each trap is much faster than the resonant frequency of the trap. Therefore, the speed at which the laser can be steered limits the number of traps that can be maintained. In a system based upon mechanical steering mirrors, the limit is located around tens of kHz, restricting the number of traps to ten. Another way of implementing multi-beam optical traps is by using multiple laser sources. The alignment of such systems can be complex and can

also be limited by the actual size of the lasers. Ogura et al. (2001) somewhat overcame these limitations by using arrays of vertical cavity surface-emitting lasers (VCSELs). The lasers can be switched on and off in order to activate different traps. However, the trapping geometries are limited to the size and configuration of the VCSEL array. Another novel way of generating multiple trapping patterns is by using patterns generated by the interference of annular beams (Macdonald, 2002). All of the above methods, though effective, often demand a high level of mechanical complexity, are component intensive and have limited optical throughput, and produce limited trapping geometries.

In the second half of the 1990s, the use of diffractive optical elements (DOEs) surfaced as an alternative to mirrors and acousto-optic modulators (Padgett et al., 2010, p. 382). Optical elements such as gratings and Fresnel lenses can be made in a myriad of geometries in order to generate arbitrary spot patterns in the far field, with the possibility of displacing the spots in both axial and lateral directions. An example of this method is the multi-beam optical trap implemented by Dufresne and Grier (1998), in which a single 532 nm laser is used in conjunction with a diffractive 4 x 4 square array generator to generate a hexadeca tweezer array. DOEs can also be designed by way of computer-generated holograms (CGHs), and can be patterned onto several different materials by lithography (Dufresne, 2001; Neto, 2004). Phase-only DOEs, known as kinoforms, can also be used to generate multiple optical traps (Grier, 2003). Dufresne et al. (2001) implemented optical tweezer arrays using computer-generated diffractive optical elements. In their work, they used an adaptive-additive algorithm to construct the hologram, which was etched onto a fused silica substrate.

The advent of phase-only and phase-mostly spatial light modulators (SLMs), which currently exceed diffraction efficiencies of 50% (Padgett et al., 2010, p.382), opened a new realm of possibilities in optics research. These devices are now commonplace in optical trapping applications, mainly in the implementation of holographic optical tweezers (HOTs) (Curtis et al., 2002; Grier; Roichman, 2005; Woerdemann, 2012). The main task in HOTs is to find a phase-only hologram that generates the desired intensity distribution in the focal plane of the microscope objective. To this end, algorithms such as the Gerberch-Saxton algorithm (Neto et al., 1995; Dufresne, 2001), the direct binary search algorithm, and kinoform sectioning (Padgett et al., 2010, p. 382), have been used. One inherent property of HOT applications is that a local change in the reconstruction plane generally requires a global change in the CGH, requiring the recalculation of the entire hologram (Eriksen et al., 2002a). In certain applications, this undesired feature can constitute the limiting factor for the speed at

which dynamic optical traps can be operated. Furthermore, the high space-bandwidth product (SBP) requirements of the SLM and diffraction losses place a further limitation on the generation of large trapping arrays using HOTs (Eriksen et al., 2002b; Grier; Roichman, 2006).

## 1.1. Motivation

Phase contrast techniques have been commonplace in various microscopy applications since the invention of the phase contrast method by Fritz Zernike in the 1930s (Hecht, 2002; Goodman, 2004). As an alternative to HOTs, this technique has found its way into the implementation of static and dynamic multi-beam traps by way of the generalized phase contrast (GPC) method (Eriksen et al., 2002a; Eriksen et al., 2002b) and by hybrid holographic phase contrast techniques such as that proposed by Woerdemann (2012). In this master's project, we propose a new method, which consists of the integration of the zero-order phase contrast technique (Pizolato et al., 2007) in a microscopy system for generation of static multi-beam optical traps. This technique makes use of existing concepts of Zernike phase contrast and two-pixel encoding techniques to generate intensity patterns in the image plane that are directly related to phase distributions in the input plane, which is comprised by a spatial light modulator (SLM). The non-holographic, and thus non-iterative nature of this technique has potential for applications for which SBP and computational speed are critical parameters.

## 1.2. Objectives

The main purpose of this work is to implement experimentally an optical trapping system that uses the Zero Order Phase Contrast technique as the generator of multiple optical patterns.

For the sake of clarity, specific objectives of this project are summarized as follows:

- ❖ To implement a single optical trap of 2.0  $\mu\text{m}$  diameter fused silica beads using standard microscopy and optical trapping techniques;
- ❖ To implement the Zero Order Phase Contrast Technique using a Liquid Crystal Television (LCTV) as the input DOE;
- ❖ To evaluate, in a proof-of-principle approach, the implementation of a multi-beam optical trapping system using the zero order phase contrast technique as the generator of multiple intensity patterns.

To the best of our knowledge, this project would constitute the first implementation of a multi-beam optical trapping system that integrates the zero order phase contrast technique.

### 1.3. Organization

- ❖ **Chapter 2** – Theoretical introduction to optical trapping. We provide a historical background and subsequently define the main parameters of operation, considering Rayleigh and Mie scattering theory, as well as geometrical optics as tools for describing the behavior of a particle trapped in a radiation well.
- ❖ **Chapter 3** – Theoretical treatment of the zero order phase contrast technique. Using Fourier optics and the theory proposed by Pizolato et al. (2007), we discuss the mathematical and optical details of this technique. Also, since an LCTV operating in the phase-mostly regime is used as the input DOE, we treat the main parameters of operation of this device.
- ❖ **Chapter 4** – Methods from literature regarding the use of Fourier Optics in optical trapping. The state of the art is discussed in this section.
- ❖ **Chapter 5** – Materials and Methods. Optical laboratory setups are described in detail for the implementation of a single optical trap, the characterization of the LCTV used in our experiments, the implementation of the zero order phase contrast technique, and finally for the integration of the zero order phase contrast technique into a microscopy system.
- ❖ **Chapter 6** – Results of our experiments. First, we present the optical results from the implementation of a single optical trap. Second, we present the results from the characterization of the LCTV and use these results in the implementation of the zero order phase contrast technique, for which we produce several images captured in the

imaging plane of the system. And third, we present the optical results of the integration of the zero order phase contrast technique into a microscope system for optical trapping.

- ❖ **Chapter 7** – Discussion of the results from our experiments. Our project is concluded, and potential improvements and future work are discussed.



## 2 OPTICAL TRAPPING

### 2.1. Historical Background

The concept of light pressure dates back to as early as 1619, when Kepler hypothesized about the nature of the repulsive force that the sun exerts on comet tails (Padgett et al., 2010, p.1). It was not until James Maxwell's work that the notion that light can exert force, or radiation pressure on a particle, became widely accepted (Woerdemann, 2012). In *A Treatise on Electricity and Magnetism*, published in 1873, Maxwell states: "In a medium in which the waves are propagated there is a pressure in the direction normal to the wave, and numerically equal to the energy contained in unit volume" (Padgett et al., 2010, p.1). Nichols and Hull (1901) examined the radiation pressure exerted on silvered glass vanes placed inside an elaborate apparatus at different air pressures. They minimized the effects of thermal interaction between the gas and the vanes in order to isolate the pressure exerted solely by the gas inside the chamber when exposed to a concentrated beam of light originating from a carbon arc lamp. Nevertheless, the high intensity gradients required to accelerate, effectively trap and manipulate particle are only readily achieved when using a laser as the light source.

In 1970, Arthur Ashkin started the field of optical manipulation by guiding freely suspended particles in liquid and gaseous states using a focused beam from a continuous wave (CW) laser. In one of his experiments, Ashkin used a single mode argon laser to guide micron-sized ( $\varnothing 0.59\text{-}2.68\ \mu\text{m}$ ) transparent latex spheres suspended in water. He found that "if a beam with milliwatts of power hits a  $2.68\ \mu\text{m}$  sphere off-center, the sphere is simultaneously drawn in to the beam axis and accelerated in the direction of the light (Ashkin, 1970)." The inward force experienced by the particles with higher index of refraction than that of the medium became known as the *gradient force* (Woerdemann, 2012). In his 1970 publication, Ashkin also presented the implementation of an optical trap by using two counter-propagating beams.

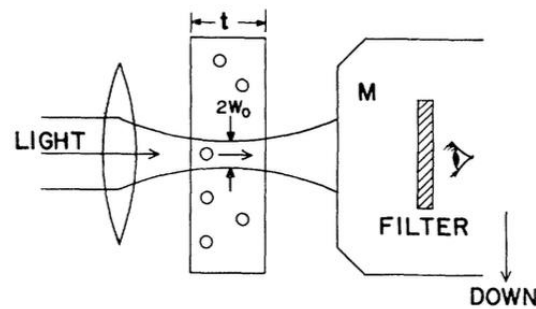


Figure 2.1. Illustration of acceleration of a particle in a glass cell of thickness  $t = 120 \mu\text{m}$ . The forward propagation of the particles generated by the focused laser light is observed through a microscope (M) (Ashkin, 1970).

In 1986, Ashkin et al. (1986) published their findings on what is considered the first reported single-beam gradient force trap. In this paper, the authors describe the optical trapping of particles in the Rayleigh (*diameter*  $\ll \lambda$ ) and Mie (*diameter*  $\gg \lambda$ ) size regimes. Given the positive and promising results, Ashkin and his colleagues foresaw potential in optical trapping for manipulation of macromolecules, colloids, aerosols, and biological particles. In fact, in 1987, Ashkin, Dziedzic, and Yamane implemented optical trapping and manipulation of viruses and bacteria using an infrared laser (Ashkin et al., 1987). These fundamental findings led to the rise of innumerable applications centered on optical manipulation. Moreover, the ease with which optical trapping systems can be integrated with other techniques made them a promising tool for applications in microscopy, spectroscopy, and microfluidics, with ever-expanding horizons. Already in the 1990s, a myriad of applications were being found for optical tweezers as micromanipulators and tensiometers (Block, 1992; Lang; Block, 2002). In (Block, 1992), the author highlights his work in the micromechanical measurement of the torsional compliance of single bacterial flagella in *escherichia coli* and *treptococcus* using optical tweezers to generate forces that overcome the torque generated by the flagellar motor. A great example of integration of optical trapping with other laser-based techniques is the use of optical tweezers with ultrapulsed microbeams. Weigand-Stubing implemented laser-assisted cell fusion by spatially approximating two cells with the use of optical tweezers and subsequently perforating their membranes using ultraviolet (UV) light (Block, 1992). These are only a couple of examples of applications in the field of biology, in which optical trapping has had the most impact over the past 10 to 15 years, especially in the field of single-molecule research, with seminal studies in kinesin, myosin, and DNA, and molecular motors (Wang et al., 1997; Grier, 2003; Padgett et al., 2012, p. 37).

## 2.2. Optical Trapping Theory

The physical principle of optical trapping can be described as follows: a dielectric particle located in the path of a tightly focused beam experiences a force due to the transfer of momentum from the incident photons (Ashkin et al., 1986; Neuman; Block, 2004; Nieminen et al., 2007a). This optical force can be thought of as consisting of two components: a scattering force, which acts in the direction of light propagation, and a gradient force, which acts in the direction of the spatial light gradient, which is highest at the focus of the beam. Figure 2.2 presents a ray optics rendition of the net force acting on a particle in response to the intensity gradient of the trapping beam. In order to effectively trap a particle, the axial gradient force pulling the particle towards the focus of the beam must overcome the axial scattering force pushing the particle away from it. More specifically, as light passes through a transparent material having an index of refraction greater than that of its surrounding medium, it induces fluctuating dipoles. These dipoles interact with the inhomogeneous electromagnetic field generated by the laser, resulting in a force directed towards regions of the light with the highest irradiance (Block, 1992; Neuman; Block, 2004). This force is proportional to two parameters: the polarizability of the dielectric particle, and the optical intensity gradient at the focus of the beam.

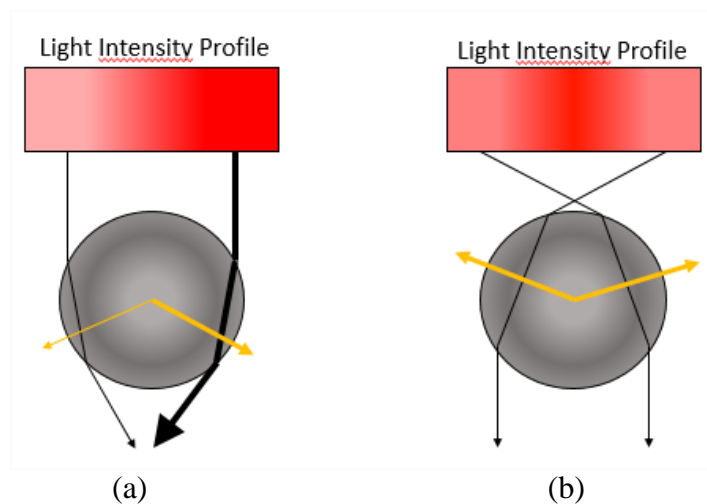


Figure 2.2. Ray optics portrayal of the net force on a transparent dielectric particle as a result of the light intensity gradient (shown in red). An optical intensity gradient concentrated to the right causes the particle in (a) to experience a net force (depicted in yellow arrows) to the right and slightly down. The particle in (b), experiences a net force towards the focus of the beam as a result of the radial intensity profile (Neuman; Block, 2004).

The implementation of a precise quantitative model that describes a particle trapped in the field gradient of a focused beam is not trivial. This difficulty is due to the fact that the trapped particles are of sizes comparable to that of the trapping laser wavelength (Padgett et al., 2010). The typical size of particles of interest in most biological and materials science applications is in the  $0.1-10\lambda$  range, which is in between the Rayleigh and Mie scattering regimes (see Figure 2.3). In this range, the particles are too large to be treated as point objects in an inhomogeneous, spatially varying field, and too small to be analyzed using ray optics (Neuman; Block, 2004; Padgett et al., 2010). It is worth noting that the main objective in this master's project is to produce qualitative results, and thus detailed quantitative analyses are outside the scope of this work and left as a future endeavor.

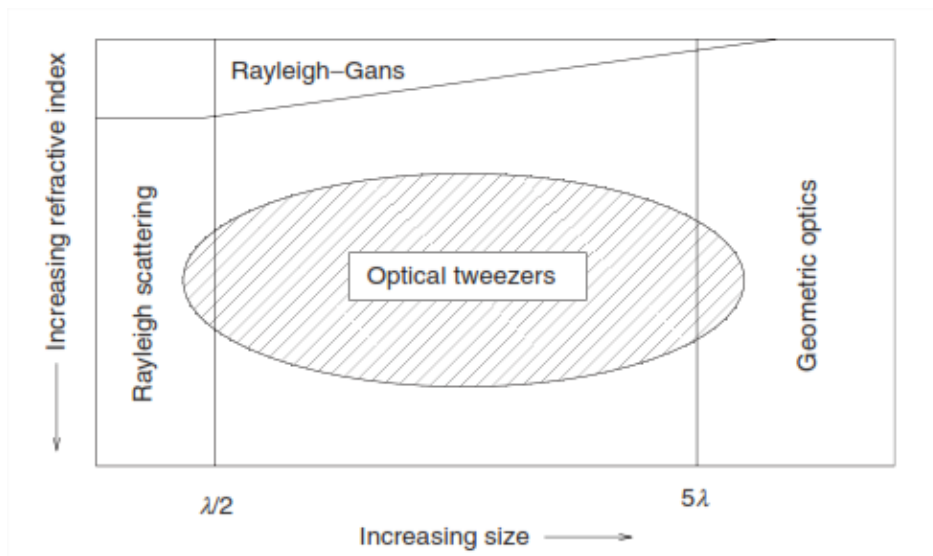


Figure 2.3. Map of regimes of validity of methods for computing the scattering of light by particles based on their size and refractive index. The typical size of the particles used in optical trapping experiments falls outside the domain of approximate methods, requiring direct solution of either Maxwell equations or the vector Helmholtz equation (Nieminen et al., 2007a).

When the radius  $a$  of the trapped particle is much smaller than the wavelength of the trapping laser ( $a \ll \lambda$ ), the scattering and gradient forces can be readily separated by using Rayleigh scattering theory, and the particle is treated as a point dipole. The equation for the gradient force  $F_{grad}$ , which as previously mentioned is a function of the polarizability  $\alpha$  of the particle and the intensity  $I_0$  of the trapping beam, can be expressed as follows (Neuman; Block, 2004):

$$F_{grad} = \frac{2\pi\alpha}{cn_m^2} \nabla I_0, \quad (2.1)$$

where  $n_m$  is the index of refraction of the medium,  $c$  is the speed of light in vacuum, and  $\nabla$  is the mathematical gradient operator. The polarizability of the particle is given by the following equation:

$$\alpha = n_m^2 a^3 \left( \frac{m^2 - 1}{m^2 + 2} \right), \quad (2.2)$$

where  $m$  is the ratio of the index of refraction of the particle ( $n_p$ ) to that of the index of the medium ( $n_p/n_m$ ).

The scattering force  $F_{scat}$  is given by

$$F_{scat} = \frac{I_0 \sigma n_m}{c}, \quad (2.3)$$

where  $\sigma$  is the scattering cross-section of the sphere:

$$\sigma = \frac{128\pi^5 a^6}{3\lambda^4} \left( \frac{m^2 - 1}{m^2 + 2} \right)^2. \quad (2.4)$$

If we let  $R$  be the ratio of the gradient force  $F_{grad}$  to the forward-scattering force  $F_{scat}$ , then it follows that for a stable optical trap this ratio needs to be greater than or equal to unity. For a Gaussian beam of focal spot size  $w_0$ , this condition is satisfied at an axial position  $z = \pi w_0^2 / (\sqrt{3}\lambda)$ , and we get the following expression for  $R$  (Ashkin et al, 1986):

$$R = \frac{F_{grad}}{F_{scat}} = \frac{3\sqrt{3}}{64\pi^5} \frac{n_m^2}{\left( \frac{m^2 - 1}{m^2 + 2} \right)} \frac{\lambda^5}{a^3 w_0^2} \geq 1. \quad (2.5)$$

The stability condition above is independent of power and constitutes a necessary but not sufficient condition for Rayleigh trapping (Ashkin et al., 1986). An additional condition is the requirement that the Boltzmann factor  $\exp(-U/k_b T)$ , where  $k_b$  is Boltzmann's constant,  $T$  is temperature, and  $U$  is the potential of the gradient force ( $U = n_m \alpha E^2 / 2$ ), be much less than unity. The factor  $k_b T$  describes the kinetic energy of the particle due to thermal fluctuations (i.e. Brownian motion). Therefore, this condition requires that the time to pull a particle into the trapping volume be much less than the time for the particle to diffuse out due to Brownian motion.

In the Mie scattering regime, in which the diameter of the particle  $2r$  is much larger than the trapping wavelength, ray optics adequately describes the physics of the force exerted on a particle in an optical tweezers system. This force can be understood in terms of changes in the momentum flux  $p$  of the trapping beam, expressed as  $p = n_m P / c$ , where  $P$  is the power

contained in the trapping beam (Nieminen et al., 2007a). Any change in the convergence or divergence of the beam modifies its axial momentum, causing a reaction force in the trapped particle.

Referring to Figure 2.4 below, the particle can be thought of as a weak positive lens. (a) If the lens is located at the beam focus, the net optical force is zero, and the rays emerge at the backside of the lens undeviated. (b) If the lens is located before the focus, it increases the convergence of the beam, therefore decreasing the momentum flux. The lost momentum is transferred to the lens, which is then displaced in the direction of propagation. (c) If the lens is located after the focus, it decreases the divergence of the beam, thus increasing the momentum flux. This results in a restoring force in the direction of the beam focus. (d) If there is a displacement of the lens in the lateral direction, the beam is deflected towards the central optical axis of the lens, gaining lateral momentum. The restoring force experience by the lens acts towards the optical axis of the beam (Nieminen et al., 2007a).

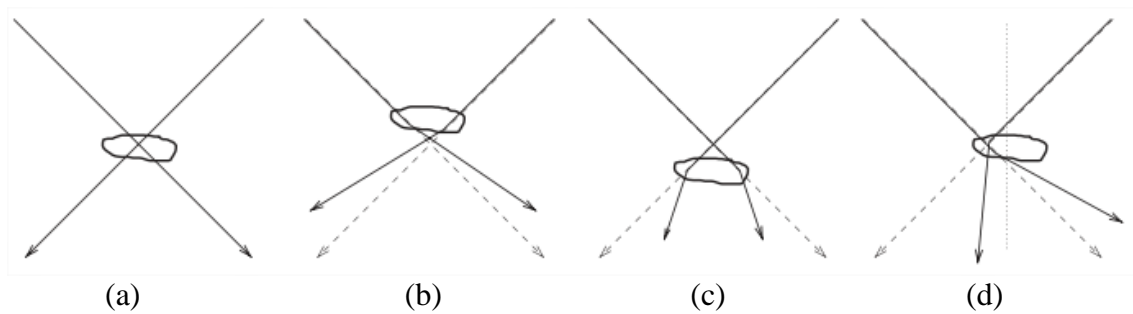


Figure 2.4. Changes in momentum flux of a trapping beam depending on the location of the lens. (a) When located at the center of the focus, the lens does not cause momentum flux changes in the trapping beam. (b) A reaction force in the direction of propagation results when the particle is located above the beam focus. (c) If the lens is located after the focus, it increases the momentum flux of the beam, resulting in a reaction force towards the focus. (d) A reaction force directed towards the beam axis results when the particle is displaced sideways (Nieminen et al. 2007a).

Ashkin (1992) derived a set of equations for the axial and lateral forces experienced by a dielectric particle in the Mie regime located in the path of a tightly focused beam. Using the geometry shown in Figure 2.4, and defining dimensionless quality factors  $Q_s$ ,  $Q_g$  and  $Q_{mag}$  ( $Q_s + Q_g$ ) appended to the scattering and gradient forces, respectively, he evaluated the magnitude of the forces as a function of the angle of incidence. His results are shown on Figure 2.5.

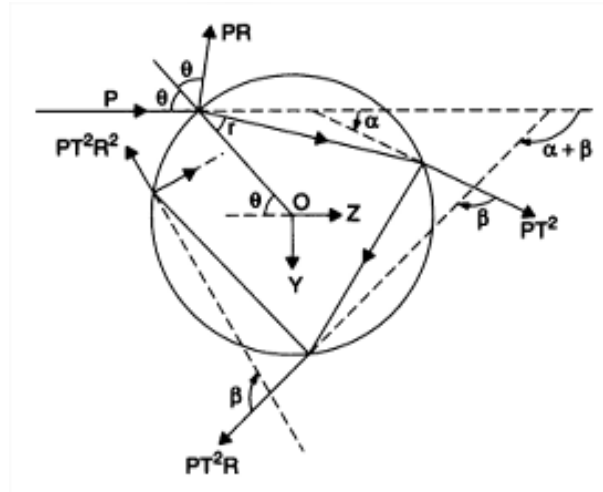


Figure 2.5. Geometry for calculating the force due to scattering of a single ray of power  $P$  incident on a dielectric sphere at an angle  $\theta$ . The reflected ray is represented by  $PR$  and refracted rays are represented by  $PT^2R^n$  (Ashkin, 1992).

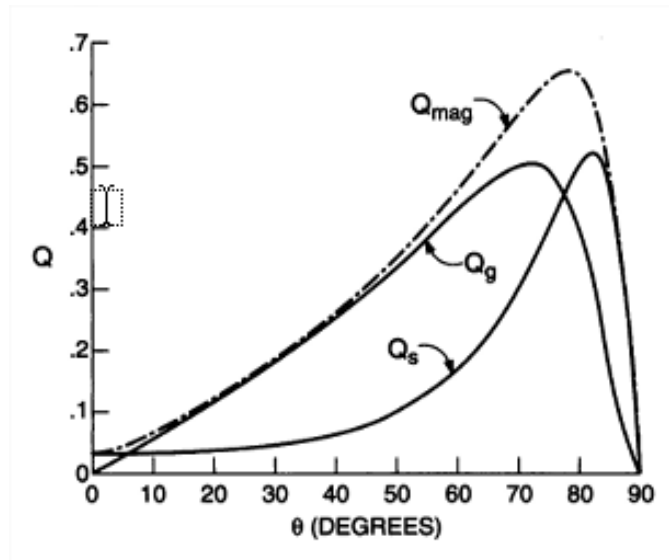


Figure 2.6. Values for the gradient force quality factors  $Q_s$ ,  $Q_g$  and  $Q_{mag}$  ( $Q_s + Q_g$ ) for a single ray incident on a dielectric sphere of  $n_p = 1.2$  at angle  $\theta$ .  $Q_{grad}$  values of  $\sim 0.5$  are generated at incidence angles around  $70^\circ$  (Ashkin, 1992).

In practice, the particles typically manipulated with optical tweezers lie in the intermediate range where the size of the particle is comparable to the wavelength of the trapping beam. In addition, given that optical trapping occurs in the vicinity of a tightly focused beam, the paraxial approximation in geometrical optics is not valid, and thus a more rigorous approach needs to be undertaken in order to fully characterize an optical trapping system. Mazolli et al. (2002) derived an explicit partial-wave representation for the force exerted on a dielectric sphere based on a Debye-type representation of a laser beam focused

by a high-numerical-aperture microscope objective. In this approach, the laser beam is treated as a superposition of plane electromagnetic waves. The authors found that the equilibrium position and trap stiffness oscillate as functions of the circumference-to-wavelength ratio, a result that was not predicted by previous theories. Moreover, partial agreement was found between the partial-wave approach and the geometrical optics approach for solving the optical forces for particles in the geometrical optics limit. Another approach uses classical Lorenz-Mie theory (Nieminen et al. 2007a; Woerdemann, 2012). This theory represents the incident and scattered electromagnetic waves as sums of vector spherical wavefunctions (VSWFs). The incident field  $E_{inc}$  and the scattered field  $E_{scat}$  can be expressed as

$$\mathbf{E}_{inc} = \sum_{n=1}^{\infty} \sum_{m=-n}^n a_{nm} \mathbf{M}_{nm}^{(3)} + b_{nm} \mathbf{N}_{nm}^{(3)} \quad (2.6)$$

and

$$\mathbf{E}_{scat} = \sum_{n=1}^{\infty} \sum_{m=-n}^n p_{nm} \mathbf{M}_{nm}^{(1)} + q_{nm} \mathbf{N}_{nm}^{(1)}, \quad (2.7)$$

Respectively, where  $n$  is the radial mode index,  $m$  is the azimuthal mode index,  $a_{nm}$ ,  $b_{nm}$ ,  $p_{nm}$ , and  $q_{nm}$  are the mode amplitudes of the incident and scattered fields, and  $\mathbf{M}_{nm}^{(3)}$ ,  $\mathbf{N}_{nm}^{(3)}$ ,  $\mathbf{M}_{nm}^{(1)}$ , and  $\mathbf{N}_{nm}^{(1)}$  are the VSWFs of the third and first type, respectively. Using the above equations as a starting point, Nieminen et al. (2001, 2003), developed numerical approaches to calculating the forces acting on spheroidal and cylindrical particles using a method known as the T-matrix method. A computational toolbox was also developed and made publicly available (Nieminen et al., 2007b). We make use this toolbox in Chapter 6.

### 3 THE ZERO ORDER PHASE CONTRAST TECHNIQUE

In 1953, the Dutch physicist Fritz Zernike was awarded the Nobel Prize in Physics for his discovery of the phase contrast microscope (Hecht, 2002). The phase contrast technique is based on spatial filtering principles, and is used in the generation of intensity patterns that are linearly related to the phase shift introduced by the object (under certain conditions). Ignoring the finite extent of the entrance and exit pupils of an image forming system, we can define the transmittance of a transparent object illuminated by a coherent wavefront of amplitude equal to unity as follows (Goodman, 2004):

$$t(x, y) = \exp[ja(x, y)] , \quad (3.1)$$

where  $a(x, y)$  is the object-induced phase shift.

In order to maintain linearity between the phase-shift and intensity, the phase shift  $a(x, y)$  is assumed small compared to  $2\pi$ , in which case we can consider only the first two terms of the Taylor series expansion of  $t(x, y)$ :

$$t(x, y) \approx [1 + ja(x, y)] . \quad (3.2)$$

The first term in the equation above represents the dominant wave component that passes through the object and undergoes a uniform phase shift, while the second, weaker term represents weaker light diffracted away from the optical axis. The intensity distribution generated by the system can be approximated as

$$I(x, y) \approx |1 + ja(x, y)|^2 \approx 1 . \quad (3.3)$$

It can be seen from Equation 3.3 that the diffracted light cannot be observed. Zernike realized that the diffracted light is not observable in the image plane because it is in phase quadrature with the background. By inserting a phase-changing plate in the focal plane of the system, the phase relation between the focused light, corresponding to the background, and the diffracted light, corresponding to higher spatial frequencies, can be modified, yielding intensity contrast that reveals the physical features of the object. Referring to the  $4f$  correlator path shown in Figure 3.1, the phase changing plate, which acts as a Fourier filter, is placed in the back focal plane of the first lens, where the Fourier transform of the phase object is located. Appendix A.1 explains in detail how positive lenses optically execute the Fourier

transform of input light distributions. The plate consists of a glass substrate with a small transparent dot with a dielectric coating designed such that the Fourier transform of the object is retarded by  $\pi/2$  radians in relation to the diffracted light.

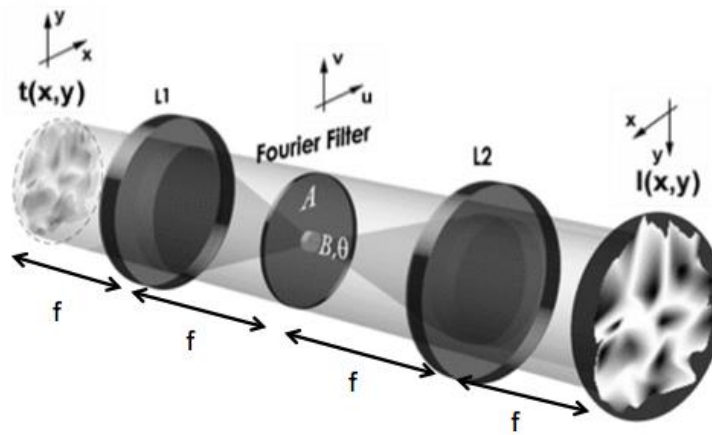


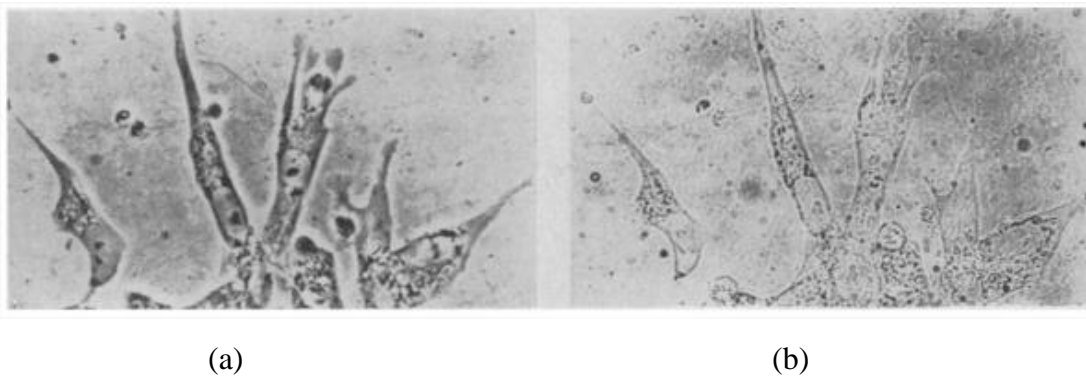
Figure 3.1. Intensity distribution generation in a  $4f$  optical system using a Fourier filter (Adapted from Glückstad; Palima, 2009)

The resulting intensity in the image plane can be expressed as follows:

$$I = \left| \exp \left[ j \left( \frac{\pi}{2} \right) \right] + ja(x,y) \right|^2 = |j(1 + a(x,y))|^2 \approx 1 + 2a(x,y). \quad (3.4)$$

It is evident that the image intensity has become linearly related to the phase shift  $a(x,y)$ .

Figure 3.2. below shows images produced by Zernike using phase contrast and brightfield microscopy.



(a)

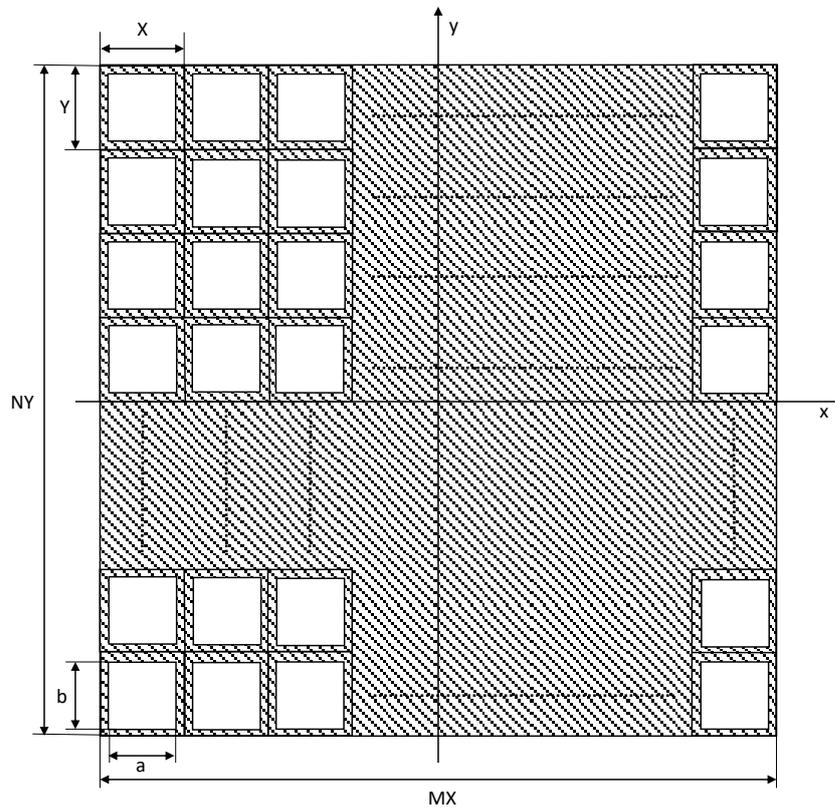
(b)

Figure. 3.2. Image of living tissue culture using (a) phase contrast microscopy and (b) brightfield microscopy (Zernike, 1955).

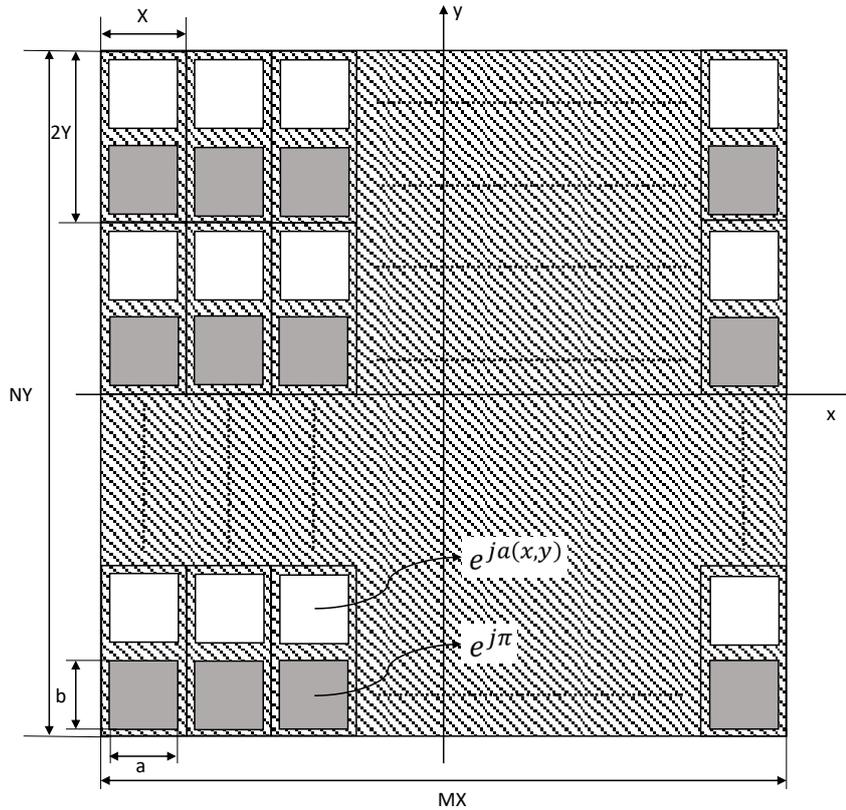
Zernike's phase contrast technique continues to be used in many applications to this day. The zero order phase contrast technique uses these same principles and modern methods to produce intensity distributions from phase distributions projected onto an LCTV operated in the phase modulation regime.

### 3.1. Theory of the Zero Order Phase Contrast Technique

Let us consider a phase distribution  $t(x,y)$  formed by an  $M \times N/2$  matrix of square macropixels, each of size  $X \times 2Y$ , representing a DOE such as an LCTV placed at the input of a  $4f$  optical correlator. The phase-encoded distribution is formed by gray-level image  $a(x,y)$ , whose phase shift is assumed to be less than one radian and is normalized in order to assure the linearity condition ( $0 \leq a(x,y) \leq 1$ ) (Neto, 1998; Goodman, 2004; Pizolato et al. 2007). Each macropixel in the diffractive element is divided into two phase regions, one that is modulated in relation to the gray-level information in  $a(x,y)$ , and the other modulated by the phase value  $\exp(j\pi)$ . Each pixel region is of finite size  $a \times b$ , as shown in Figure 3.3 below:



(a)



(b)

Figure. 3.3. Pixel representation used in the zero order phase contrast technique. (a) Geometry of a DOE composed by a matrix of  $M \times N$  pixels of size  $X \times Y$ , each with active area  $a \times b$ . (b) DOE geometry using macropixels of size  $X \times 2Y$ . Each white subpixel is modulated by the information contained in  $a(x,y)$ , and the subpixels represented in gray color are modulated by  $e^{j\pi}$ .

Considering that the system is illuminated by a uniform, coherent wave of amplitude equal to unity, and applying the Taylor series approximation used in Equation 3.2 to the  $\exp[ja(x,y)]$  term, the transmittance of  $t(x,y)$  can be expressed as follows (Banyal; Prasad, 2005; Pizolato et al. 2007):

$$t(x,y) \approx \left\{ [1 + ja(x,y)] \frac{III}{2XY} \left[ \frac{x}{X}, \frac{(y-\frac{2Y}{4})}{2Y} \right] * \text{rect} \left( \frac{x}{a}, \frac{y-\frac{2Y}{4}}{b} \right) + \exp(j\pi) \frac{III}{2XY} \left[ \frac{x}{X}, \frac{(y+\frac{2Y}{4})}{2Y} \right] * \text{rect} \left( \frac{x}{a}, \frac{y+\frac{2Y}{4}}{b} \right) \right\} \text{rect} \left( \frac{x}{MX}, \frac{y}{NY} \right) \quad (3.5)$$

where  $III(x,y)$  represents the two-dimensional comb function, defined, in its uni-dimensional form as

$$III(ax) = \frac{1}{|a|} \sum_{m=-\infty}^{\infty} \delta\left(x - \frac{m}{a}\right), \quad (3.6)$$

\* represents the convolution operation, and *rect* is the rectangular function (Bracewell, 2000):

$$rect(p, q) = \begin{cases} 0, & |p|, |q| > 1/2 \\ 1/2, & |p|, |q| = 1/2 \\ 1, & |p|, |q| < 1/2 \end{cases} \quad (3.7)$$

The intensity distribution produced at the image plane is given by

$$I(x, y) \approx \left\{ \left[ 1 + ja(x, y) \right] \frac{III}{2XY} \left[ \frac{x}{X}, \frac{(y-\frac{2Y}{4})}{2Y} \right] * rect\left(\frac{x}{a}, \frac{y-\frac{2Y}{4}}{b}\right) + exp(j\pi) \frac{III}{2XY} \left[ \frac{x}{X}, \frac{(y+\frac{2Y}{4})}{2Y} \right] * \right. \\ \left. rect\left(\frac{x}{a}, \frac{y+\frac{2Y}{4}}{b}\right) \right\} \left| rect\left(\frac{x}{MX}, \frac{y}{NY}\right) \right|^2 \approx 1. \quad (3.8)$$

Identical to the result of Eq. 3.3, the diffracted light is not observable due to its phase quadrature with the background. If the contribution of the background as well as that of the  $exp(j\pi)$  term are eliminated, then the intensity variations arising from the diffracted term can be observed. Furthermore, the pixelated structure of the DOE generates several diffraction orders in the Fourier plane (i.e. the back focal plane of the first lens in the  $4f$  correlator, see Figure 3.1). In order to suppress the first and higher diffraction orders, an aperture with the same bandwidth as that of the zero order component is placed in the center of the Fourier plane, allowing only the transmission of the zero order spectrum of the phase distribution.

Let us carry out the Fourier transform of Eq. 3.5 in order to define the complex distribution just before the aperture. First, distributing the approximated Taylor series terms, we get the following equation for  $t(x, y)$ :

$$t(x, y) \approx \left\{ \begin{array}{l} \frac{III}{2XY} \left[ \frac{x}{X}, \frac{(y-\frac{2Y}{4})}{2Y} \right] * rect\left(\frac{x}{a}, \frac{y-\frac{2Y}{4}}{b}\right) \\ + ja(x, y) \frac{III}{2XY} \left[ \frac{x}{X}, \frac{(y-\frac{2Y}{4})}{2Y} \right] * rect\left(\frac{x}{a}, \frac{y-\frac{2Y}{4}}{b}\right) \\ + exp(j\pi) \frac{III}{2XY} \left[ \frac{x}{X}, \frac{(y+\frac{2Y}{4})}{2Y} \right] * rect\left(\frac{x}{a}, \frac{y+\frac{2Y}{4}}{b}\right) \end{array} \right\} rect\left(\frac{x}{MX}, \frac{y}{NY}\right) \quad (3.9)$$

Now, let us apply the Fourier transform to  $t(x, y)$  in parts, starting with the first term in Equation 3.8, and ignoring the multiplicative *rect* term outside of the brackets, for now. We can make use of the Fourier convolution and shift theorems (Goodman, 2004), obtaining the following expressions:

$$\mathcal{F} \left\{ \frac{III}{2XY} \left[ \frac{x}{X}, \frac{(y-\frac{2Y}{4})}{2Y} \right] * \text{rect} \left( \frac{x}{a}, \frac{y-\frac{2Y}{4}}{b} \right) \right\} = abIII(Xu, 2Yv) \text{sinc}(au, bv) \exp \left( -j\frac{\pi}{2}v \right) \exp \left( -j\frac{\pi}{b}Yv \right). \quad (3.10)$$

The Fourier transform of the second term is given by

$$\mathcal{F} \left\{ ja(x, y) \frac{III}{2XY} \left[ \frac{x}{X}, \frac{(y-\frac{2Y}{4})}{2Y} \right] * \text{rect} \left( \frac{x}{a}, \frac{y-\frac{2Y}{4}}{b} \right) \right\} = ja(u, v) * abIII(Xu, 2Yv) \text{sinc}(au, bv) \exp \left( -j\frac{\pi}{2}v \right) \exp \left( -j\frac{\pi}{b}Yv \right). \quad (3.11)$$

The Fourier transform of the third term is given by

$$\mathcal{F} \left\{ \exp(j\pi) \frac{III}{2XY} \left[ \frac{x}{X}, \frac{(y+\frac{2Y}{4})}{2Y} \right] * \text{rect} \left( \frac{x}{a}, \frac{y+\frac{2Y}{4}}{b} \right) \right\} = -abIII(Xu, 2Yv) \text{sinc}(au, bv) \exp \left( j\frac{\pi}{2}v \right) \exp \left( j\frac{\pi}{b}Yv \right). \quad (3.12)$$

Finally,

$$\mathcal{F} \left\{ \text{rect} \left( \frac{x}{NX}, \frac{y}{MY} \right) \right\} = MNXY \text{sinc}(MXu, NYv). \quad (3.13)$$

The complex distribution  $S(u, v)$  just before the aperture can then be expressed as follows:

$$S(u, v) \approx abMNXY \left\{ \left[ III(Xu, 2Yv) \exp \left( -j\frac{\pi}{2}v \right) \exp \left( -j\frac{\pi}{b}Yv \right) + ja(u, v) * III(Xu, 2Yv) \exp \left( -j\frac{\pi}{2}v \right) \exp \left( -j\frac{\pi}{b}Yv \right) - III(Xu, 2Yv) \exp \left( j\frac{\pi}{2}v \right) \exp \left( j\frac{\pi}{b}Yv \right) \right] \text{sinc}(au, bv) \right\} * \text{sinc}(MXu, NYv) \quad (3.14)$$

Now, Eq. 3.13 gets a multiplicative *rect* function term when we place an aperture of size  $U \times V$  corresponding to the size of the zero-order component of the spectrum in the Fourier plane. The distribution  $S'(u, v)$  just after the aperture is then given by:

$$S'(u, v) \approx S(u, v) \text{rect} \left( \frac{u}{U}, \frac{v}{V} \right)$$

$$S'(u, v) \approx abMNXY \left\{ \left[ III(Xu, 2Yv) \exp \left( -j\frac{\pi}{2}v \right) \exp \left( -j\frac{\pi}{b}Yv \right) + ja(u, v) * III(Xu, 2Yv) \exp \left( -j\frac{\pi}{2}v \right) \exp \left( -j\frac{\pi}{b}Yv \right) - III(Xu, 2Yv) \exp \left( j\frac{\pi}{2}v \right) \exp \left( j\frac{\pi}{b}Yv \right) \right] \text{sinc}(au, bv) \right\} * \text{sinc}(MXu, NYv) \text{rect} \left( \frac{u}{U}, \frac{v}{V} \right). \quad (3.15)$$

In order to simplify the expression above, we can start by considering the effect of the aperture on the *comb* functions. Given that we are restricting the transmission to only the zero-order component, the *comb* functions are now replaced by simple *delta* functions, as follows:

$$S'(u, v) \approx abNMXY\{[\delta(u, v) + jA(u, v) * \delta(u, v) - \delta(u, v)]\text{sinc}(au, bv)\} * \text{sinc}(MXu, NYv) \quad (3.16)$$

An immediate result of this simplification is the cancelation of two delta terms. Also, considering that the convolution of a function  $f(x)$  by the *delta* function is equal to the function  $f(x)$  itself (Bracewell, 2000), we can further simplify the expression for  $S'(u, v)$ :

$$S'(u, v) \approx abMNXyjA(u, v)\text{sinc}(au, bv) * \text{sinc}(NXu, MYv) \quad (3.17)$$

In practice, the pixelated structure of the SLM generates replicas of the projected pattern in higher diffraction orders, which, depending on the size of the active area of the pixel  $a \times b$ , contribute to a decrease in the zero order efficiency by the transfer of energy to higher levels. The resulting *sinc* distributions in Equation 3.16 act as attenuation factors for the replicas. The first *sinc* distribution, arising from the discontinuous pixel size of the DOE, acts as a global attenuation factor for  $S'(u, v)$ . However, given that  $a(x, y)$  is a real distribution, most of its Fourier spectrum  $A(u, v)$  is concentrated in the center of the Fourier plane, a region smaller than the width of the attenuating *sinc* distribution (Neto et al., 2004). As a result, the *sinc* function has a negligible effect in  $A(u, v)$ . Furthermore, the second *sinc* function, in convolution with  $A(u, v)$ , also has a weak influence on the resulting distribution. This is because  $A(u, v)$  is a smooth spectrum, with no discontinuities or phase jumps (Pizolato; Neto, 2009).  $S'(u, v)$  now becomes

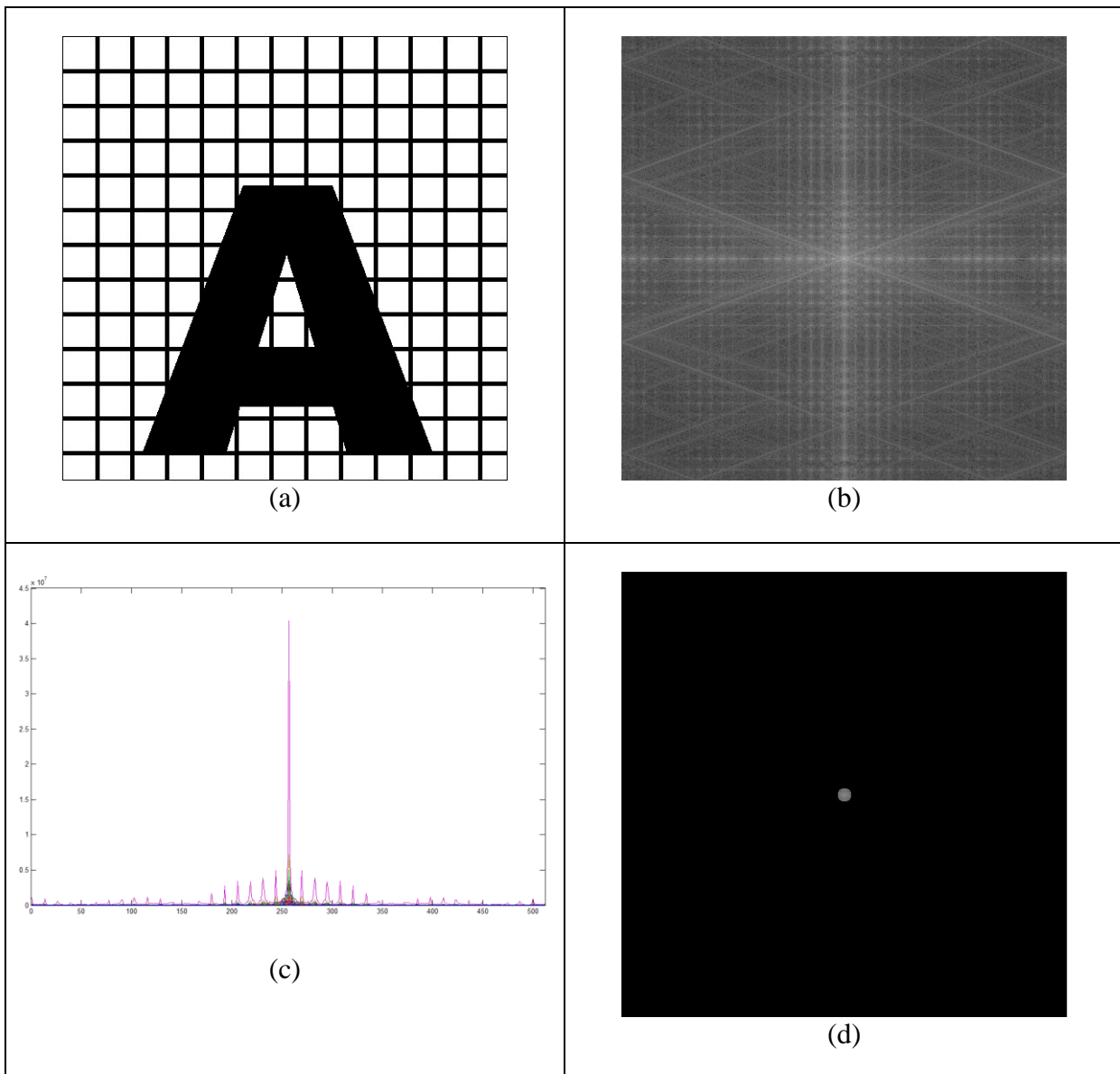
$$S'(u, v) \approx A(u, v) . \quad (3.18)$$

The second lens in the  $4f$  correlator optically performs the inverse Fourier transform of  $A(u, v)$ , and the intensity distribution in the image plane becomes

$$I(x, y) = a(x, y)^2. \quad (3.19)$$

It is evident now that the zero order phase contrast technique produces a quadratic relationship between phase and intensity. Let us illustrate the effect of this technique with an example. As was first detailed in the Abbe-Porter experiments (Hecht, 2002; Goodman, 2004), the optical Fourier transform performed by a lens of a mesh object yields a series of

isolated spectral components, each separated by a distance proportional to the separation between each mesh component. Equivalently, the LCTV in our experiments can be regarded as a mesh, or a grid, in which the pixels are not continuous but rather separated by a finite distance. Upon Fourier transforming by the first lens in the  $4f$  correlator, each spot in the diffraction pattern (Fig. 3.4(b)) corresponds to a different diffraction order  $m$  ( $m = 0, \pm 1, \pm 2, \pm 3, \dots$ ), each with its own specific spatial frequency. The zero-order phase contrast technique isolates the zero diffraction order (i.e. the zero-frequency location), which is where most of the spectrum is concentrated. Figure 3.4 illustrates a computational example of this optical principle.



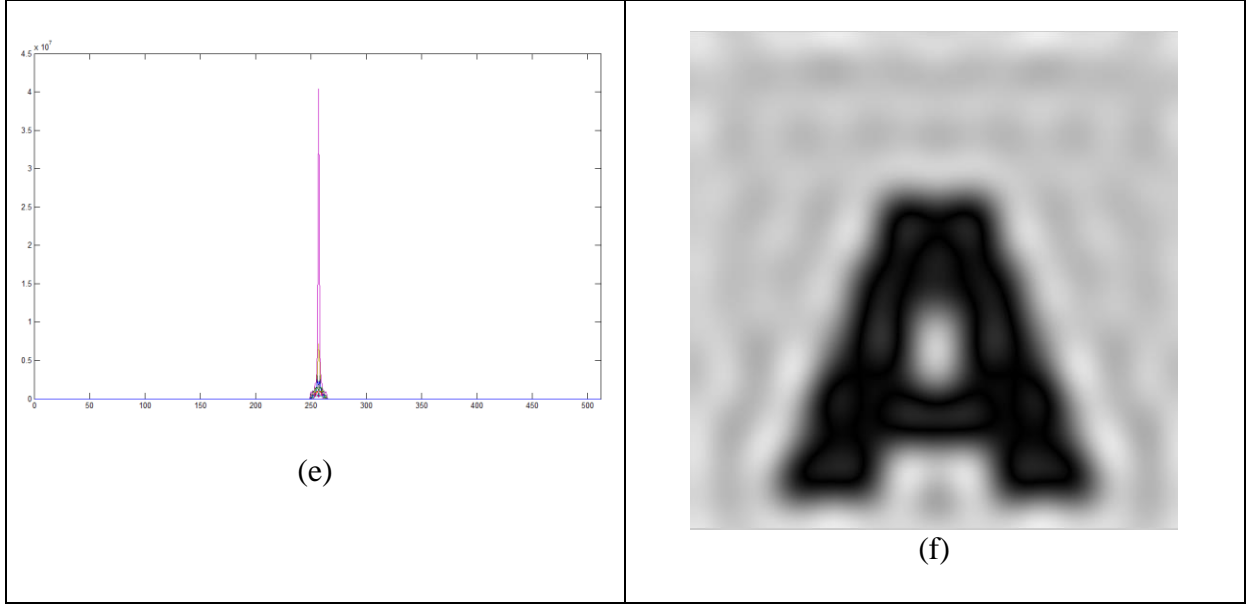


Figure 3.4. Computational simulation of a zero-order filter. (a) Image of letter A and mesh to simulate the finite dimension of the LCTV pixels (512x512). (b) Image of the Fourier spectrum of (a). Notice the periodic peaks due to the FT of the mesh distribution. They represent the different orders of diffraction that arise from the pixelated configuration of the DOE. (c) Plot of the Fourier spectrum. (d) Zero-order filter applied to Fourier transform of (a). (e) Plot of Fourier spectrum after application of filter. Only the zero-order frequency passes through the filter. (f) Filtered image after inverse Fourier transform.

### 3.2. Efficiency of the Zero Order Phase Contrast Technique

Considering the structure of the DOE and the phase distribution coded onto it, it is possible to determine the optical efficiency of the zero order phase contrast system. Using Figure 3.3a as reference, the energy of the transmitted light through a DOE formed by a matrix of  $M \times N$  pixels of size  $X \times Y$  illuminated with a coherent monochromatic plane wave is given by (Pizolato, 2006)

$$e_t = \frac{\int_{-\frac{MX}{2}}^{\frac{(M-1)X}{2}} \int_{-\frac{NY}{2}}^{\frac{(N-1)Y}{2}} t(x,y)^2 dx dy}{\int_{-\frac{MX}{2}}^{\frac{(M-1)X}{2}} \int_{-\frac{NY}{2}}^{\frac{(N-1)Y}{2}} dx dy} \times 100\% \quad (3.20)$$

We can also derive an expression for the zero order diffraction efficiency,  $e_{zero}$ :

$$e_{zero} = \frac{\int_{-\frac{MX}{2}}^{\frac{(M-1)X}{2}} \int_{-\frac{NY}{2}}^{\frac{(N-1)Y}{2}} |S(u,v)|^2 du dv}{\int_{-\infty}^{\infty} \int_{-\infty}^{\infty} |S(u,v)|^2 du dv} \times 100\%, \quad (3.21)$$

where  $S(u,v)$  is the complex Fourier spectrum of  $t(x,y)$ .

Finally, the global diffraction efficiency  $e_{global}$  is given by

$$e_{global} = e_t e_{zero} \quad (3.22)$$

For a phase-only DOE, the value for  $e_t$  is equal to unity (i.e. 100%). However, for a pixelated DOE in which the pixels are discontinuous, the maximum achievable transmitted efficiency is determined by the available active area of each pixel in the DOE.

### 3.3. Considerations for Determining the Size of the Zero Order Filter

Given the sampling nature of the zero order phase contrast technique, the spectrum of the function  $t(x,y)$  consists of replicas of the phase pattern periodically separated by the two-dimensional distances determined by the structure of the pixelated DOE. As previously mentioned, these replicas are attenuated by the resulting *sinc* distributions, which can decrease the overall efficiency of the propagated image formed by the zero diffraction order by transferring energy to higher orders (Neto et al. 2004). Furthermore, the global diffraction efficiency of the zero-order-reconstructed image is also a function of the phase distribution projected onto the DOE, which in our case is an LCTV (see Equation 3.22). Therefore, the spatial frequency components of the phase distribution projected onto the LCTV determine first, whether energy will be lost to higher orders after propagation through the zero order system, and second, the size of the filter necessary in order to generate an exact intensity distribution from the phase information.

To investigate this, we can derive an expression for the intensity distribution of the Fraunhofer diffraction pattern generated by the phase pattern projected onto our LCTV. Due to the mathematical complexity of this derivation, we implement the derivation only in one dimension, choosing the  $x$ -axis due to its slightly simpler manipulation (see Equation 3.14). For  $t(x)$ , we have then the following expression:

$$t(x) \approx \left\{ [1 + ja(x)] \frac{III}{X} \left( \frac{x}{X} \right) * \text{rect} \left( \frac{x}{a} \right) + \exp(j\pi) \frac{III}{X} \left( \frac{x}{X} \right) * \text{rect} \left( \frac{x}{a} \right) \right\} \text{rect} \left( \frac{x}{MX} \right) \quad (3.23)$$

The Fourier transform of the above equation is as follows:

$$\mathcal{F}\{t(x)\} = S(u) = [aXIII(Xu)\text{sinc}(au) + jA(u) * aXIII(Xu)\text{sinc}(au) - aXIII(Xu)\text{sinc}(au)] * MX\text{sinc}(MXu), \quad (3.24)$$

which can be further simplified to

$$S(u) = [aXjA(u) * III(Xu)\text{sinc}(au)] * MX\text{sinc}(MXx). \quad (3.25)$$

To facilitate our analysis, we can apply the following multiplication and convolution properties of the *comb* function (Bracewell, 2000):

$$III(x)f(x) = \sum_{m=-\infty}^{\infty} f(n)\delta(x - n) \quad (3.26)$$

$$III(x) * f(x) = \sum_{m=-\infty}^{\infty} f(x - n) \quad (3.27)$$

Applying Equation 3.26 first, we get the following result for  $S(u)$ :

$$S(u) = aMX \sum_{m=-\infty}^{\infty} \text{sinc}\left(m\frac{a}{X}\right) \delta\left(u - \frac{m}{X}\right) * \text{sinc}(MXu) * jA(u) \quad (3.28)$$

Now, applying Equation 3.27, we get an expression for  $S(u)$  that can be more easily analyzed:

$$S(u) = aMX \sum_{m=-\infty}^{\infty} \text{sinc}\left(m\frac{a}{X}\right) \text{sinc}\left[MX\left(u - \frac{m}{X}\right)\right] * jA(u). \quad (3.29)$$

The expression for the intensity distribution  $I(x)$  becomes:

$$I(x) = \left(\frac{aMX}{\lambda z}\right)^2 \left\{ \sum_{m=-\infty}^{\infty} \text{sinc}\left(m\frac{a}{X}\right) \text{sinc}\left[\frac{MX}{\lambda z}\left(x - m\frac{\lambda z}{X}\right)\right] * jA(u) \right\}^2, \quad (3.30)$$

where  $u=x/\lambda z$ , with  $\lambda$  defined as the wavelength of the light source and  $z$  the propagation distance.

Examining Equation 3.30 closely, we see that the intensity distribution of the Fraunhofer diffraction pattern is equal to a sum of *sinc* terms that depend on the size and number of pixels of the DOE, each with a weighing factor  $\text{sinc}\left(m\frac{a}{X}\right)$ , which is at the same time determined by the active pixel size and separation. Furthermore, the sum is convolved with the spectrum of the phase function. Noting that the weighing factor for the  $m=0$  term is independent of the ratio of  $a$  to  $X$ , the intensity of the zero diffraction order is the maximum possible value. However, as stated before, depending on the spectrum of the phase function in  $t(x)$ , energy can be lost from the zero order to  $m \neq 0$  diffraction orders. The figure below illustrates the effect of the pixelated nature of the LCTV and its finite total area on the intensity pattern, without considering the phase distribution:

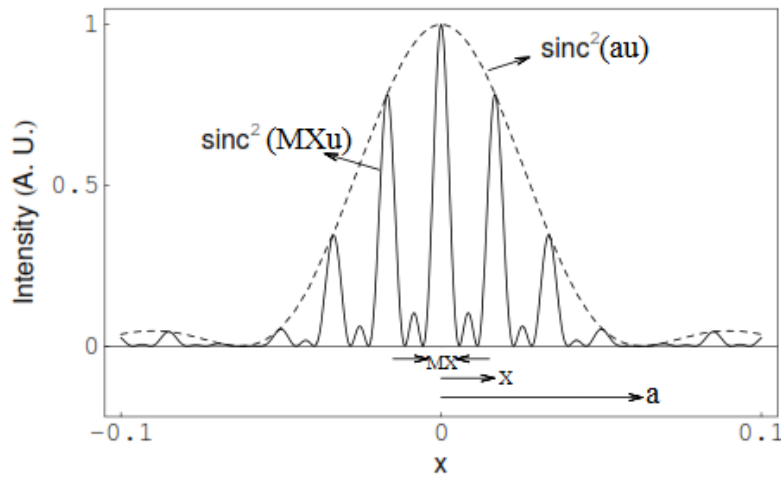


Figure 3.5. Simulation of the effect of the *sinc* functions on the diffraction pattern generated by the LCTV (adapted from BANYAL; PRASAD, 2005).

Now, looking at the  $\text{sinc} \left[ \frac{MX}{\lambda z} \left( x - m \frac{\lambda z}{X} \right) \right]$  function at  $m=0$  (i.e. the zero order), we have the width  $\Delta x$  is given by  $\Delta x = 2\lambda z / MX$ . This value dictates the maximum recommended size for the zero order filter. A zero order filter with a large diameter could potentially allow for the propagation of light originating from the side lobes of neighboring *sinc* distributions, and, more importantly, for light belonging to higher diffraction orders to propagate through the system. Conversely, a filter with too narrow a diameter could block frequencies contained in the zero diffraction order, compromising the contrast and visibility of the intensity pattern in the image plane. Moreover, from an experimental perspective, it is important to note that the Fourier lens can also compromise the size of the zero order diffraction pattern, given that it can introduce aberrations that widen the size of the focal spot. In our experiments, several pinhole sizes were tested before arriving at a reasonable image contrast at the image plane. The analysis above leads us to conclude that it is necessary to consider the physical specifications of the DOE, the optics being used, and the specific phase pattern projected onto the LCTV in order to define the appropriate diameter of the zero order filter.

### **3.4. Use of SLM as the Input DOE in the Zero Order Phase Contrast Technique**

A spatial light modulator (SLM) is an electro-optical device that can be configured in real time and is capable of modifying the amplitude, phase, or polarization of an incident optical wavefront as a function of position across the wavefront (Neff et al., 1990). These devices can be addressed optically, as is the case in SLMs in which the information is input in the form of an optical image from a CRT display, for example, or electronically, in which electrical signals are used to drive the optical response of the device. They can also perform a variety of operations, such as analog multiplication and addition (analog multiplication being an operation common to all SLMs), signal conversion, non-linear operations, and short-term storage (Neff et al., 1990). There are several types of SLMs: magnet-optic SLMs, deformable mirror SLMs, multiple-quantum-well SLMs, acousto-optic Bragg cells, and liquid crystal SLMs (Goodman, 2004), among others. In our work, we use a liquid crystal television (LCTV) SLM as the input DOE in order to project the phase patterns used in the zero order phase contrast technique. In the following subsections, we cover the operating principle of liquid crystal SLMs and how they are used in our experiments.

#### **3.4.1 Properties of Liquid Crystals**

Liquid crystals share some properties of both solid and liquid state materials. The liquid crystal state is a state of matter in which the molecules have orientational order, as is the case in crystals, but lack positional order, as is the case in liquids (Saleh; Teich, 1991). There are three phases within the liquid crystal state: nematic, smectic, and cholesteric, which are determined by the different orientation and organizational boundaries of the crystals. In nematic liquid crystals, the molecules tend to favor a parallel orientation throughout the entire volume, however their positions are random within that volume. Smectic liquid crystal molecules favor parallel orientations and possess positional order in one dimension; that is, their centers are arranged in parallel layers, with random molecule positions within each layer. Cholesteric liquid crystals are a distorted form of smectic liquid crystals, in which the molecules undergo a helical rotation about an axis from layer to layer within the volume (Goodman, 2004).

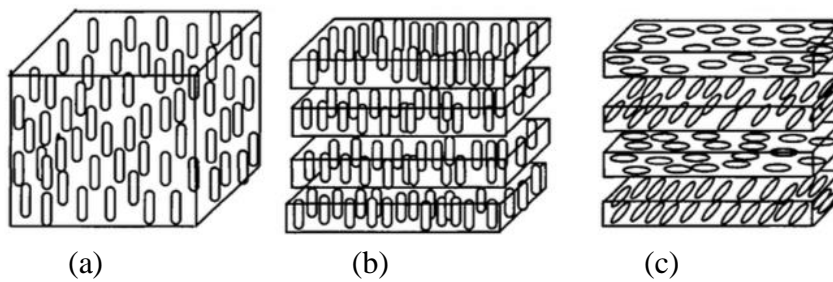


Figure 3.6. The different molecular organizations of (a) nematic, (b) smectic, and (c) cholesteric liquid crystals (Goodman, 2004).

By sandwiching nematic phase liquid crystals between two glass plates, and coating the plates with alignment layers polished in different directions (orthogonally, for example), the alignment of the molecules in contact with the alignment layers and the tendency of the molecules themselves to maintain their parallel orientations combine in order to produce a *twisted* nematic liquid crystal. The alignment layers, usually fabricated in polyimide material, are located between the liquid crystals and transparent conductive films of indium tin oxide, which are used in order to apply AC voltages to the LCs. The electric field is applied between the two glass plates, and the long axis of the molecules tends to align with the direction of the field.

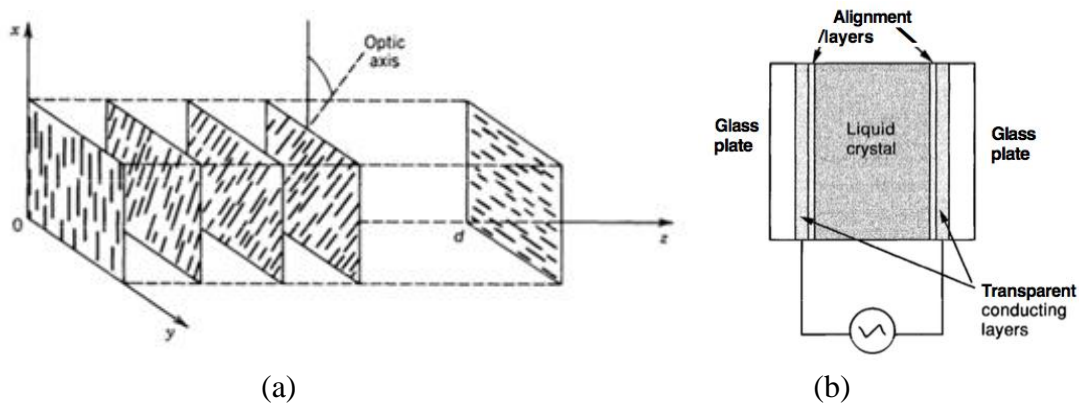


Figure 3.7. (a) Molecule orientation in a twisted nematic crystal with twist angle  $\theta=90^\circ$ . The outermost LCs, in contact with the alignment layers (shown in (b)), determine the overall orientation of the crystals. The conducting layers are illustrated in (b) (Saleh; Teich, 1991; Goodman, 2004).

Based on Figure 3.7(a), let us consider a liquid crystal volume of thickness  $d$ , with each incremental uniaxial slice of the material orthogonal to the  $z$  axis and an angle of twist  $\alpha$  which varies linearly with  $z$ . Using *Jones Calculus*, we can express the complete effect of the LC cell on incident light in matrix form (Saleh; Teich, 1991; Goodman, 2004). This mathematical tool facilitates the characterization of polarization-sensitive devices through the

implementation of matrix operations. The output polarization of such a device can be related to the input polarization vector through a 2 x 2 matrix as follows (Goodman, 2004):

$$\vec{U}' = L\vec{U} = \begin{bmatrix} l_{11} & l_{12} \\ l_{21} & l_{22} \end{bmatrix} \vec{U}, \quad (3.31)$$

where  $\vec{U}'$  is the output polarization vector,  $\vec{U}$  is the input polarization vector, and  $L$  is the polarization matrix operator.

In the case of an LCTV, the Jones matrix  $W_0$  of a single slice of a cell with  $N$  slices can be represented with the following matrix for an optical retarder:

$$W_0 = \begin{bmatrix} e^{j\frac{2\pi}{\lambda}n_e\frac{d}{N}} & 0 \\ 0 & e^{j\frac{2\pi}{\lambda}n_o\frac{d}{N}} \end{bmatrix}. \quad (3.32)$$

In the equation above,  $n_o$  and  $n_e$  are the ordinary and extraordinary indices of refraction, respectively.

By doing some mathematical manipulation (shown in Appendix), the Jones matrix  $M$  for an LC cell of  $N$  slices can be expressed as follows (Neto et al., 1996):

$$M = e^{j\phi} \begin{bmatrix} \cos\alpha & -\sin\alpha \\ \sin\alpha & \cos\alpha \end{bmatrix} \begin{bmatrix} \cos\gamma + \frac{j\beta\sin\gamma}{\gamma} & \frac{\alpha}{\gamma}\sin\gamma \\ -\frac{\alpha}{\gamma}\sin\gamma & \cos\gamma - \frac{j\beta\sin\gamma}{\gamma} \end{bmatrix}, \quad (3.33)$$

with the birefringence parameters  $\beta$  and  $\gamma$ :

$$\beta = \frac{\pi}{\lambda}d(n_e - n_o) \quad (3.34)$$

$$\gamma = \sqrt{\alpha^2 + \beta^2}. \quad (3.35)$$

It is worth noting that Eq. 3.33 remains valid assuming that the tilt of the molecules is homogeneous throughout the cell and that the twist angle is linear along the z-axis.

### 3.4.2. Effect of the Applied Voltage on the Index of Refraction of the LC Cell

Equation 3.34 describes an essential parameter in the characterization of a liquid crystal cell, as it determines its local birefringence. However, we must take into account that

the extraordinary index of refraction  $n_e$  is itself dependent upon the tilt angle  $\zeta$ , which is at the same time a function of the *rms* value of the applied voltage. Let us start with the equation for  $\zeta$  (Neto, 1995):

$$\zeta = \begin{cases} 0, & V_{rms} \leq V_c \\ \frac{\pi}{2} - \tan^{-1} \left\{ \exp \left[ -\frac{V_{rms} - V_c}{V_0} \right] \right\}, & V_{rms} > V_c \end{cases} \quad (3.36)$$

where  $V_{rms}$  is the *rms* value of the applied voltage,  $V_c$  the threshold voltage below which no tilting occurs, and  $V_0$  is the excess voltage at which the tilt angle is  $49.6^\circ$ .

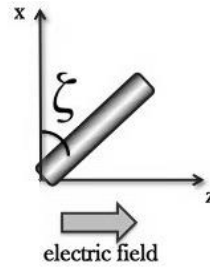


Figure 3.8. Liquid crystal molecule in tilted state.

The effective extraordinary index of refraction  $n_e(\zeta)$ , is given by:

$$\frac{1}{n_e(\zeta)} = \frac{\cos^2(\zeta)}{n_e^2} + \frac{\sin^2(\zeta)}{n_o^2}, \quad (3.37)$$

and the refraction coefficient  $\beta$  that we defined in Eq. 3.34 is redefined as

$$\beta = \frac{\pi}{\lambda} d(n_e(\zeta) - n_o). \quad (3.38)$$

From the equations above it can be deduced that the value of  $\beta$  depends on the applied voltage. With an increase in  $V_{rms}$ ,  $\beta$  decreases with an increase of the tilt angle  $\zeta$ .

### 3.4.3. Mathematical Modeling of the Polarizer-LCTV-Analyzer Optical Path

LCTVs are typically sandwiched in between two optical polarizers. In the zero order phase contrast technique, we are interested in generating phase-modulated distributions. As such, the input polarization angle  $\psi_1$  is aligned with the angle of the LCTV molecular director  $\psi_D$ , and the polarization angle of the analyzer  $\psi_2$  is aligned in parallel with the polarization orientation of the rear molecular director of the LCTV.

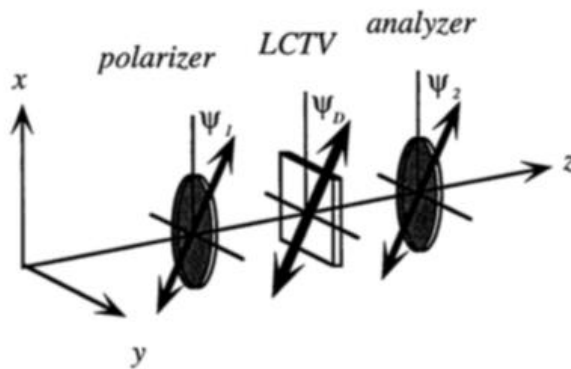


Figure 3.9. Polarizer-LCTV-analyzer sandwich configuration . The angles  $\psi_1$ ,  $\psi_D$ , and  $\psi_2$  correspond to the orientations with respect to the x-axis of the polarizer, the molecular director of the LCTV, and the analyzer, respectively (Neto et al., 1996).

We can again use Jones calculus to describe this system. The electric fields of the incident beam onto the LCTV, after passage through the polarizer, can be defined in matrix form as follows:

$$\begin{bmatrix} E_e \\ E_o \end{bmatrix} = \begin{bmatrix} \cos\theta_1 \\ \sin\theta_2 \end{bmatrix}, \quad (3.39)$$

where  $\theta_1 = \psi_1 - \psi_D$  and  $\theta_2 = \psi_2 - \psi_D$ .

The output after the analyzer is defined as:

$$\begin{bmatrix} E'_e \\ E'_o \end{bmatrix} = \begin{bmatrix} \cos^2\theta_2 & \sin\theta_2\cos\theta_2 \\ \sin\theta_2\cos\theta_2 & \sin^2\theta_2 \end{bmatrix} M \begin{bmatrix} \cos\theta_1 \\ \sin\theta_1 \end{bmatrix}, \quad (3.40)$$

where  $E'_e$  and  $E'_o$  are the electric fields of the extraordinary and ordinary axes of the analyzer, respectively, and  $M$  is the LCTV matrix given by Eq. 3.22.

The parameters for the transmittance  $T$  of the system and the phase delay  $\delta$  can be obtained from the equations above and the equations in the preceding sections:

$$T = |E'_e|^2 + |E'_o|^2$$

$$T = \left\{ \frac{\alpha}{\gamma} \sin\gamma \sin[\alpha + (\psi_1 - \psi_2)] + \cos\gamma \cos[\alpha + (\psi_1 - \psi_2)] \right\}^2 + \left\{ \frac{\beta}{\gamma} \sin\gamma \cos[\alpha - (\psi_1 + \psi_2) + 2\psi_D] \right\}^2 \quad (3.41)$$

$$\delta = \tan^{-1} \left[ \frac{\text{Im}(E'_e)}{\text{Re}(E'_e)} \right] = \tan^{-1} \left[ \frac{\text{Im}(E'_o)}{\text{Re}(E'_o)} \right]$$

$$\delta = \beta + \arctan \left\{ \frac{\frac{\alpha}{\gamma} \sin\gamma \cos[\alpha - (\psi_1 + \psi_2) + 2\psi_D]}{\frac{\alpha}{\gamma} \sin\gamma \sin[\alpha + (\psi_1 - \psi_2)] + \cos\gamma \cos[\alpha + (\psi_1 - \psi_2)]} \right\} \quad (3.42)$$

Based on these equations, it is possible to determine the theoretical regimes for amplitude-mostly and phase-mostly modulation of the polarizer-LCTV-analyzer system, given that it is not possible to achieve amplitude-only or phase-only modulation (Neto, 1995; Neto et al., 1996). As mentioned at the beginning of this section, we are interested in generating phase-modulated distributions. In phase-mostly modulation, the polarization axis of the polarizer is parallel to the front molecular director of the LCTV, and the polarization axis of the analyzer is parallel to the axis of the rear molecular director of the LCTV. Therefore,  $\psi_1 = \psi_D$ , and  $\psi_2 = \psi_D + \alpha$ , where we redefine  $\alpha$  here as the twist angle of the LCTV. We use a method proposed by Neto et al. (1996) in order to find the parameters for the molecular director angle  $\psi_D$  and  $\alpha$ , which are essential for implementing the zero order technique. The details of this method are brought forth in Chapter 5.

## 4 STATE OF THE ART

In this chapter, we focus on current applications that use Fourier optics methods in order to generate static and dynamic structured light fields for optical trapping. There are two optical trapping methods that are not only relevant but also closely related to our research: holographic optical traps (HOTs) and optical trapping using the generalized phase contrast technique. For the sake of brevity, we restrict our evaluation of these topics to the work of (Grier; Roichman, 2006) and (Curtis et al., 2012) for HOTs, and (Eriksen et al., 2002b) and (Glückstad; Palima, 2009), for the generalized phase contrast method.

### 4.1. Holographic Optical Trapping (HOT)

Holographic optical tweezers use a computer-designed DOE in order to convert a single collimated laser beam into several, arbitrarily separated beams, which are focused onto a single plane by a strong converging lens so as to produce multiple optical tweezers (Curtis et al., 2012). This is generally achieved by the use of iterative methods such as the Iterative Fourier Transform Algorithm, or IFTA. The algorithm iterates between the hologram and reconstruction (or trapping) planes through the Fast Fourier Transform (FFT) until a hologram that satisfies the constraints applied in each of the planes is found. See Figure 4.1 below. In the hologram plane, technical constraints such as pure phase modulation, plane wave or TEM<sub>00</sub> illumination, discretization of phase values, or pixelation of the SLM are taken into account (Woerdemann, 2012). In the trapping plane, the intensity distribution is set to approach the desired intensity distribution. In order to guarantee convergence of the algorithm, certain degrees of freedom, such as the phase in the trapping plane, can be used in every iteration step.

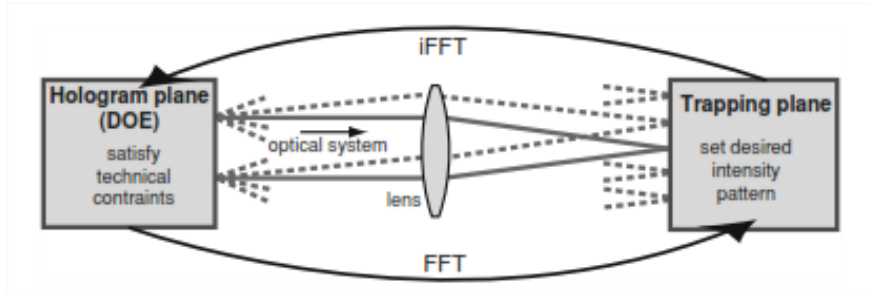


Figure 4.1. Basic schematic of the IFTA. The optical Fourier transform performed by the microscope objective connects the hologram and trapping planes. The FFT is used to numerically iterate between both planes (Woerdemann, 2012).

Grier and Roichman (2006) use an error function algorithm that seeks to improve the desired intensity distribution at the sample plane by selecting pixels at random, changing their phase values, recomputing the fields, and selecting only the changes that minimize the discrepancies between the amplitude at each trap and its corresponding field. In one experiment, the authors use a  $200 \times 200$  pixel CGH displayed by a reflective SLM to encode a pattern of 119 traps in a quasi-periodic arrangement. The optical setup used in their experiments is illustrated below:

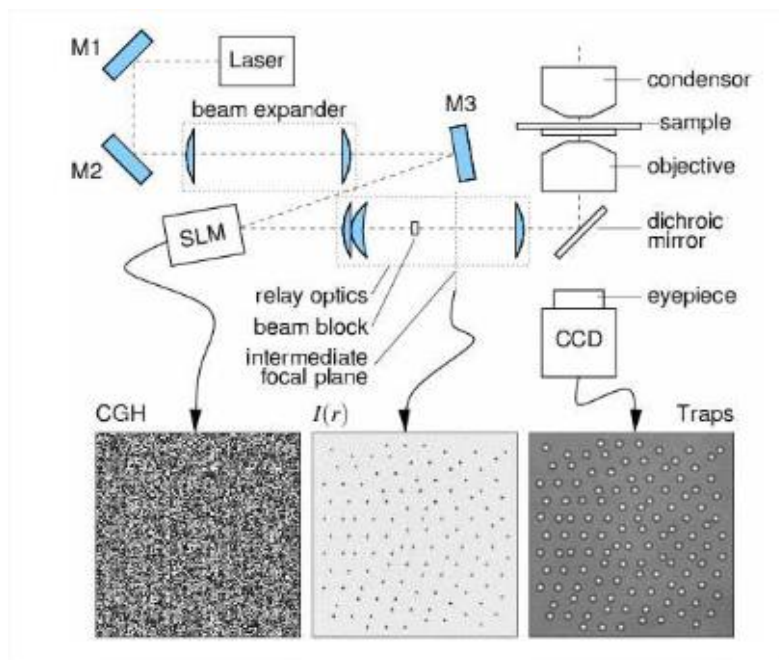


Figure 4.2. Experimental setup of HOT. The phase hologram is relayed to the back aperture of a microscope objective, which then tightly focuses the intensity distribution in order to trap  $1.5 \mu\text{m}$  diameter spheres in water (Grier; Roichman, 2006).

Using this technique, Grier and Roichman also implemented dynamic, three-dimensional manipulation over a  $100 \times 100 \times 40 \mu\text{m}^3$  volume. The optical results are shown below:

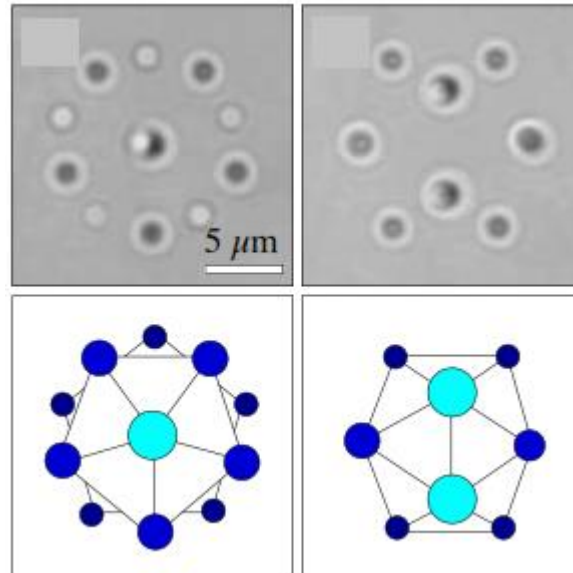


Figure 4.3. Two views of a rotating icosahedron of colloidal spheres (Grier; Roichman, 2006).

Curtis et al. (2012) used the Gerchberg-Saxton (GS) algorithm (Gerchberg; Saxton, 1972) in their experiments. They calculated a phase parameter and used it as an estimate at each iteration of the algorithm in order to arrive at the field of each trap, and from there the desired intensity distribution was calculated. With an experimental setup similar to that of Grier and Roichman's, the authors implemented an array of 400 functional optical traps. In another experiment, they implemented a dynamic, step-wise trapping pattern by rapidly replacing the hologram with another one whose reconstruction is slightly displaced, effectively translating the spheres into new geometrical configurations. See Figure 4.4 below:

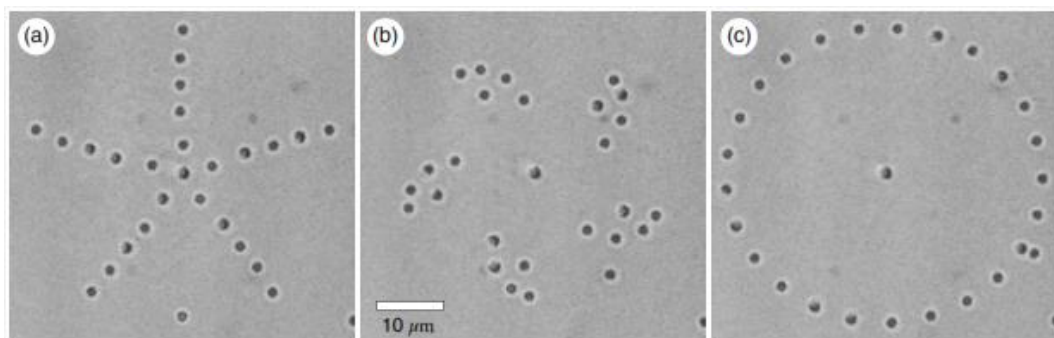


Figure 4.4. A pentagonal pattern of 26 colloidal silica spheres of  $0.99 \mu\text{m}$  in diameter is dynamically transformed into a circular pattern. (a) Original configuration. (b) After 16 steps. (c) Final configuration after 38 steps (Curtis et al., 2012).

Holographic optical trapping does not come without limitations, however. As shown in Figure 4.1, one inherent issue in HOTs in which amplitude SLMs are used is the presence of a central bright spot in the trapping plane, which results from the fact that practical DOEs diffract only a portion of the light into the intended modes (Polin et al., 2005; Woerdemann, 2012). This can be solved by making the input beam slightly convergent, and spatially filtering the undiffracted light. This procedure also eliminates the appearance of “ghost traps”, or undesired intensity peaks strong enough to trap particles. However effective, this solution increases the complexity of the optical setup.

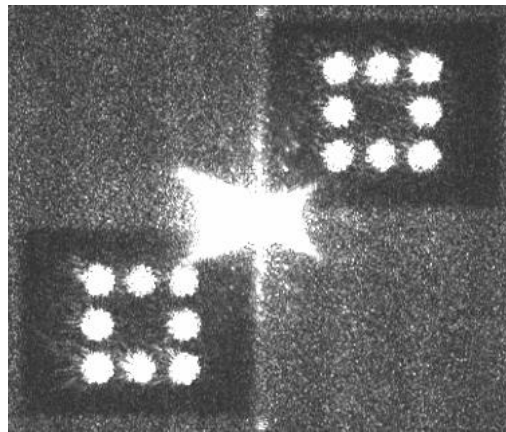


Figure 4.5. Reconstructed optical trapping pattern from a binary hologram produced at the Telecommunications lab at the EESC. The strong central peak corresponds to undiffracted light from the LCTV. The twin image is generated by the presence of complex conjugate of the original trapping pattern.

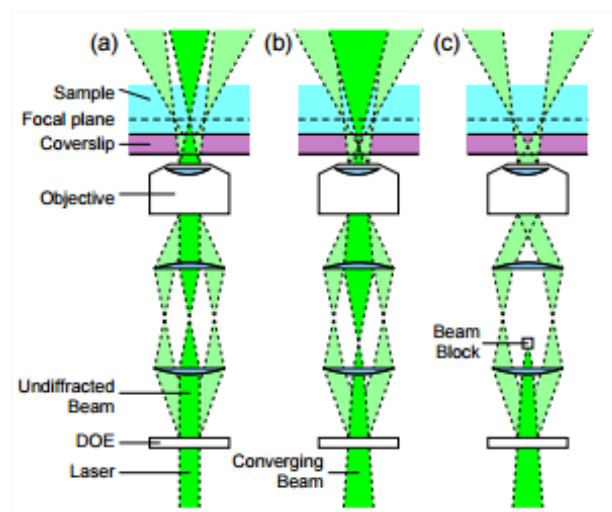


Figure 4.6. Spatial filtering of undiffracted central beam in a HOT system. (a) System with collimated laser input. (b) System with slightly converging beam. Notice how the focal point is displaced from the higher mode planes and the change in the profile at the sample plane. (c) Blocking of the central mode (Polin et al. 2005).

## 4.2. The Generalized Phase Contrast Technique (GPC) in Optical Trapping

The Generalized Phase Contrast technique, proposed by Glückstad and Palima (2009), takes into account that the input phase modulation in a phase contrast system may not always be limited to a small-scale perturbation, and thus, the Zernike approximation (see Eq. 3.2) may not be sufficient to accurately represent the phase-modulated input. In the generalized regime, higher-order terms in the Taylor series expansion of the input phasor need to be taken into account, given that the spatially varying terms can contribute to the undiffracted light even for weak phase objects ( $a(x,y) \leq \pi/3$ ). However, phase objects with shallow depth of modulation have a small effect on the constant first term of the Taylor series expansion, which can therefore be neglected without the introduction of errors. In contrast, objects with larger modulations depths can result in spatially varying terms that do significantly contribute to the on-axis light. Equation 4.1 shows a few of the higher-order terms of the Taylor series expansion of the transmittance of the input phase object:

$$t(x, y) \approx 1 + ja(x, y) - \frac{1}{2}a^2(x, y) - \frac{1}{6}ja^3(x, y) + \frac{1}{24}a^4(x, y) + \dots \quad (4.1)$$

The contribution for the spatially varying higher-order terms can constructively or destructively interfere with the on-axis light, resulting in an attenuation of the focused light amplitude. The GPC technique uses Fourier analysis in order to take into account phase objects that break the first-order Zernike approximation. Let us consider again the phase object  $\exp[ja(x, y)]$ , where  $(x, y) \in \Omega$  defines the spatial boundary of the phase object:

$$\exp[ja(x, y)] = \left( \iint_{\Omega} dx dy \right)^{-1} \iint_{\Omega} \exp[ja(x, y)] dx dy +$$

"higher frequency terms" (4.2)

In Eq. 4.2 above, the first term is a complex-valued constant linked to the on-axis focused light from the phase object, which is defined within the spatial region  $\Omega$ , and the second terms corresponds to the light scattered away from the optical axis by the spatially varying features of the phase object.

The GPC technique can be implemented in the same fashion as the zero order phase contrast technique, that is, in the path of a  $4f$  correlator (see Figure 3.1). Glückstad and Palima arrive at an expression for the field distribution at the image plane of the correlator (which can also be considered as a common path interferometer, CPI), which takes into account the non-

negligible contribution of higher order terms at phase modulation values higher than those allowed by the Zernike approximation. The final irradiance expression in the GPC technique contains two main terms: the first one contains the input transmittance multiplied by a spatially limiting *circ* function, and the second one contains the contribution of a central, complex weighted function, which in the CPI corresponds to the synthetic reference wave (SRW) of the interferometer. It is worth noting that the mathematical analysis is rather complex and out of the scope of this analysis. Furthermore, in order to design the appropriate Fourier filter, the GPC technique requires careful consideration of the SRW function of the phase object, which can have different effects on the quality of the reconstructed image.

Glückstad and Palima have implemented the GPC technique in several applications such as wavefront sensing and analysis, wavefront engineering, light shaping, and optical encryption and decryption. One of the most prominent applications is GPC-based optical micromanipulation, in the implementation of static and dynamic multi-trap systems. The authors note that one of the main advantages of the GPC technique is its simplicity of encoding, given that each point in the trapping plane corresponds to a unique point in the programmable LCTV. This feature is shared with the zero order phase contrast technique, and is different from holographic tweezers, wherein a change in the trapping plane inherently requires a global change in the projected pattern on the LCTV.

The GPC technique can be used for generating static and dynamic multi-beam optical tweezers of low and high-index particles. This constitutes a clear advantage for applications in which the sorting of particles with heterogeneous refractive index properties is necessary. Figure 4.7 below shows the optical arrangement of a system implemented in order to trap such particles. The authors of this work used a CW, 830 nm laser and a reflective SLM as the core components of this experimental setup. The output from the path of the GPC system is coupled into an inverted microscope via a dichroic mirror (DM). The output from the microscope objective (MO) is adjusted so as to match the location of the sample plane. Figure 4.8 shows the 2D intensity patterns and 3D profiles using the GPC technique.

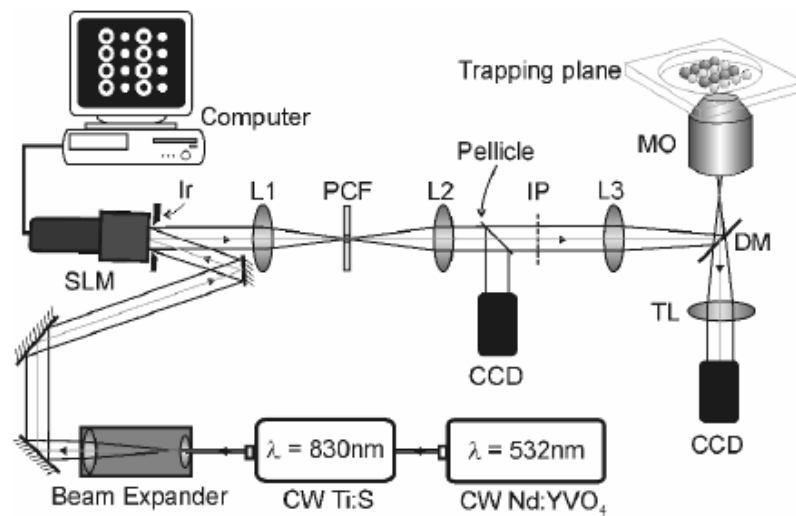


Figure 4.7. Experimental setup for the simultaneous trapping of high and low-index particles. Arbitrary phase patterns are encoded onto the SLM, and a high-contrast intensity pattern is observed in the image plane (IP). A standard inverted brightfield is used to trap and observe the particles (Glückstad; Palima, 2009).

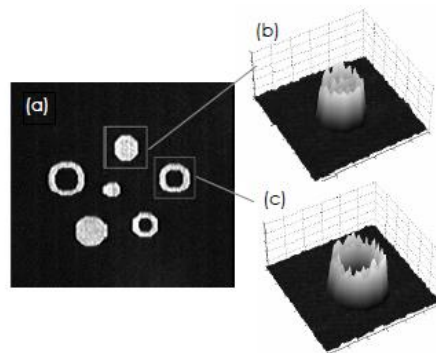


Figure 4.8. (a) High-contrast intensity pattern at the IP for high and low-index particles. (b) Nearly top-hat profile used for trapping high-index particles, and (c) doughnut profile for trapping low-index particles (Glückstad; Palima, 2009).

Taking advantage of the fast response time of the SLM used in their experiments, the authors demonstrated the optical steering of air-filled, hollow soda lime glass spheres, which effectively act as low refraction index particles ( $n_p = 1.33$ ). The particles ranged from 2-20  $\mu\text{m}$  in size. Considering the intensity profile in Figure 4.8(c), the low-index particle is enclosed within the unstable region of the intensity pattern due to its repulsion from the surrounding region of stronger light intensity. By encoding consecutive patterns onto the SLM, the particle can be steered to different regions of the sample plane.

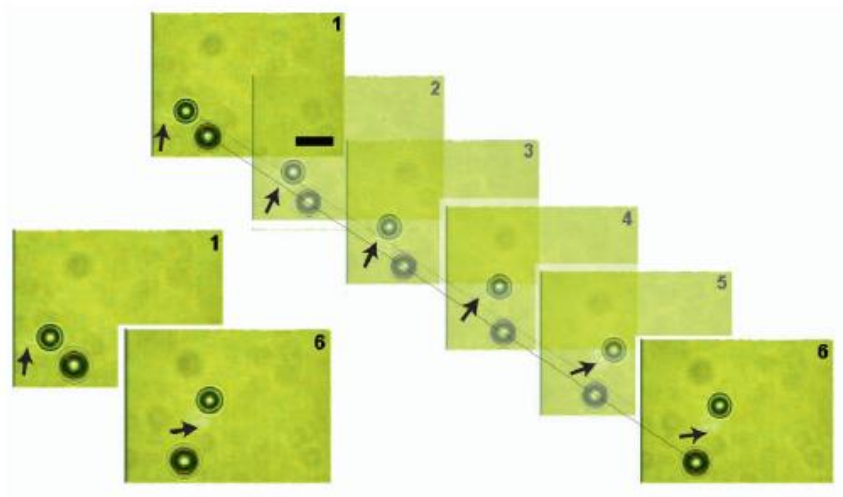


Figure 4.9. Optical steering of hollow soda lime glass spheres with a doughnut-shaped beam. The arrow indicates the user-controlled displacement of the particle at each frame. Scale bar: 10  $\mu\text{m}$  (Glückstad; Palima, 2009).

In another instance of the GPC technique, Eriksen *et al.* (2002b) used a liquid crystal SLM with a response time of 40 ms to simultaneously trap eight polystyrene micro-spheres (2  $\mu\text{m}$  in size) in six and two-fold trap arrangements. Both geometries were then controlled dynamically.

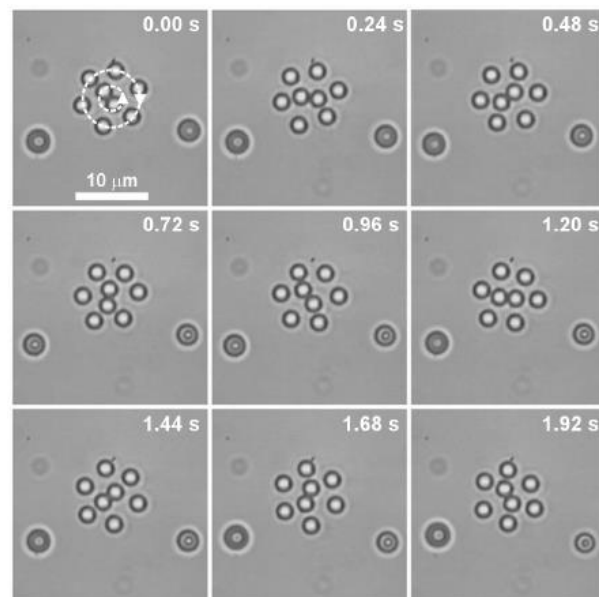


Figure 4.10. Image sequence showing dynamic rotation of six and two-fold trapping geometries using the GPC technique. The outer six spheres rotate clockwise 1/8 of a full rotation while the inner two spheres rotate counter-clockwise nearly one full rotation (Eriksen *et al.*, 2002b).

Due to its relative simplicity and versatility, the GPC technique has a variety of different applications, and recent developments published by Bañas et al. (2015) cite the generation of efficient shapes for illumination or excitation as having the biggest potential beyond research experiments. In their work, the authors demonstrate how the optical reconstruction of computer-generated holograms can be performed with up to three times higher intensity, and how the number of optically-generated spots in the image plane of a  $4f$  correlator can be increased without sacrificing brightness. The authors also demonstrate light shaping of a supercontinuum laser over the visible range with the use of a so-called GPC light shaper. Given that the GPC technique and the zero order phase contrast technique are somewhat similar in their practical implementation, it is then very probable for the zero order phase contrast technique to be applicable in many of the same applications as the GPC technique.



## 5 METHODS AND MATERIALS

In the first section of this chapter, we describe in detail the optical setup used to implement a single optical trap using a 632.8 nm HeNe laser. The following section describes the characterization of the LCTV used in our experiments, and is sequenced by the description of the optical setup used to implement the zero order phase contrast technique. The culmination of this chapter treats the integration of the zero order phase contrast technique into an upright bright field microscope for optical trapping.

### 5.1. Single Optical Trap

As mentioned in Section 2.2, a necessary condition for effectively trapping a particle is that the axial gradient force pulling the particle towards the focus of the beam must overcome the axial scattering force pushing the particle away from it. This is achieved by the generation of a very steep light intensity gradient, which is produced by sharply focusing the trapping laser beam to a diffraction-limited spot using an objective of high numerical aperture (NA) (Neuman; Block, 2004). Since light rays located in the extremes of the light beam contribute disproportionately to the axial gradient force, whereas central rays are the main agent of the scattering force, it is common practice to slightly overfill the entrance pupil of the objective in order to improve trapping efficiency. In other words, taking full advantage of the numerical aperture of the objective provides the stiffest trap possible (Appleyard et al., 2007). Neuman and Block (2004) state that the beam is typically expanded such that the  $1/e^2$  points intensity points match the objective aperture, resulting in ~87% of the incident power entering the objective. In the implementation of a single optical trap, we use a 632.8 nm, 17 mW HeNe laser from JDS Uniphase (Model 1135P, California, USA), with a beam diameter of 0.68 mm. Single optical traps were implemented using 60x and 100x magnification microscope objectives, respectively. The 60x microscope objective, manufactured by Newport Corporation (P/N M-60X, California, USA), has an NA of 0.85, a back aperture of 4.5 mm, and a working distance of 0.3 mm. The 100x objective lens is an oil immersion objective manufactured by Olympus (Model UPlanFL N, Japan), has an NA of 1.3, a back aperture of 6.0 mm and a working distance of 0.2 mm. In order to expand the laser beam, a Keplerian

beam expander was set up using a 50.0 mm effective focal length (EFL) bi-convex lens and a doublet lens with an EFL of 250.0 mm (L1 and L2, respectively, in Fig. 5.1 below). This lens combination expanded the laser beam by 5x, yielding a beam diameter of approximately 3.4 mm. We chose not to overfill the objective in order to minimize heating and thermal expansion of the objective, and also to avoid diffraction effects that might arise from light hitting the edges of the optic. Moreover, the 250 mm EFL doublet lens used offered better performance than other lenses available in our lab in terms spherical aberration effects.

The expanded laser beam was coupled into the optical path of a standard upright microscope (Edmund Optics, New Jersey, USA) using a 50:50 ratio beamsplitter, and the trapping plane was imaged onto a near-infrared and visible range sensitive CCD camera (Cohu Inc., California, USA) using a tube lens (L3 below). The tube lens was chosen depending on the microscope objective used. We used a bi-convex, 200 mm EFL lens when working with the 60x objective, and a 125 mm EFL lens for the 100x objective. Finally, a shortpass dielectric filter (P/N FES0600, Thorlabs Inc., NJ, USA) blocks light in the red spectrum from reaching the CCD camera. Below is a schematic of the optical setup:

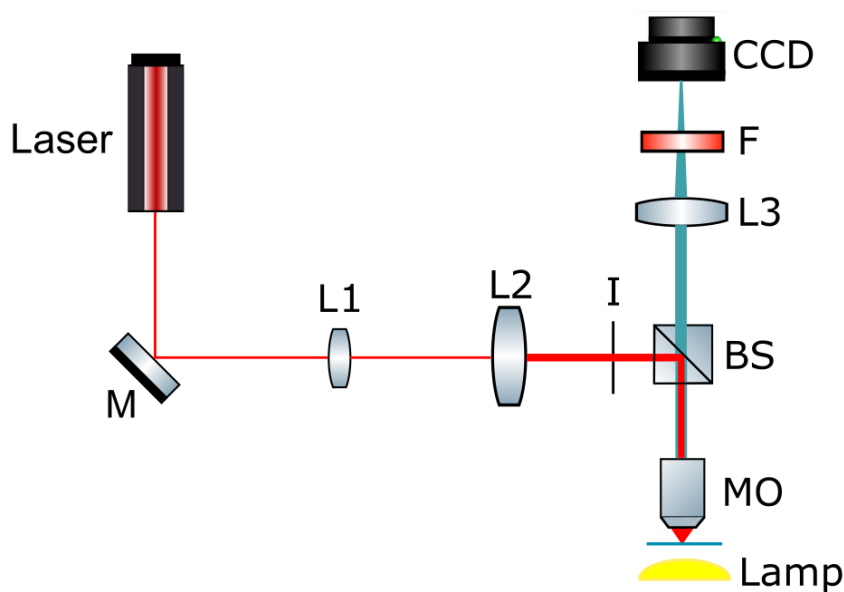


Figure 5.1. Schematic of optical path used to implement a single optical trap in the Telecommunications lab at the EESC. The laser beam bounces off a 45° mirror (M) and is expanded by lenses L1 (50 mm EFL) and L2 (250 mm EFL). After passing through an iris (I), the laser beam is coupled into the microscope by the beamsplitter (BS) and focused in the trapping plane by the microscope objective (MO). The tube lens (L3) focuses the light returning through the objective, and a shortpass filter (F) filters out any light in the red spectrum before reaching the CCD camera.



Figure 5.2. Experimental setup of optical path used to implement a single optical trap in the Telecommunications lab at the EESC.

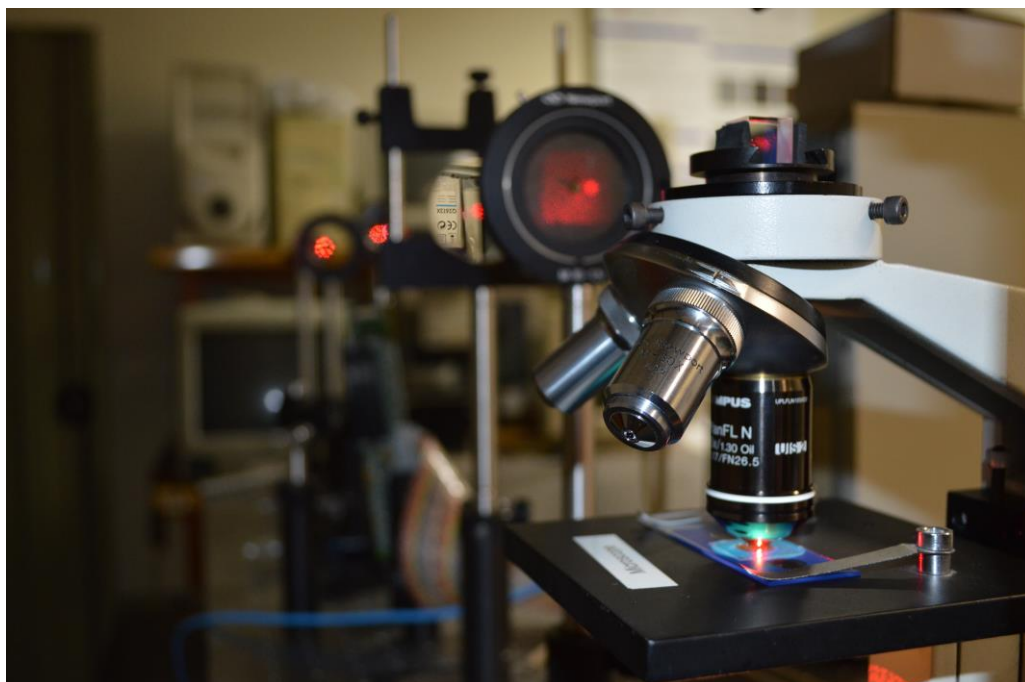


Figure 5.3. Close-up of microscope setup used in single optical trapping experiments. Light from the laser can be seen being focused onto the sample plane by the microscope objective.

A sample kit was purchased from Thorlabs Inc. (P/N OTKBTK, New Jersey, USA) for use in our optical trapping experiments. The kit consists of a solution of fused silica beads in deionized water (diameter: 2.06  $\mu\text{m}$ , density: 2 g/ml), microscope slides with 20  $\mu\text{m}$  deep reaction wells, 18 mm x 18 mm cover glass pieces, and other components for sample preparation.

With the sample mounted on the holder of the microscope, the axial range of the objective was adjusted so as to bring the micro-particles into focus on the CCD. In order to ensure that both the laser focal plane and the microscope focal plane are coplanar, the tube lens (L3) and CCD camera were adjusted in the z-direction until both the focused laser spot and the particles are imaged in focus on the CCD image screen. Although the shortpass filter used blocked most of the light in the red spectrum from reaching the CCD, a small percentage of light enough to visualize the laser focus was still visible on the monitoring screen. This greatly facilitated optical alignment of the particle and laser focus planes.



Figure 5.4. Sample preparation kit purchased from Thorlabs Inc. used in optical trapping experiments (Image taken from [www.thorlabs.com](http://www.thorlabs.com), 2017.)

## 5.2. Characterization of the Liquid Crystal Television

Before we describe the laboratory methods and materials used in the zero order phase contrast technique, it is necessary to describe in detail the LCTV used in our experiment, as it constitutes the central component in the projection of patterns used in the implementation of the zero order phase contrast technique. We use an LCTV extracted from a *Seiko-Epson InFocus TVT-6000* projector system in our experiments. The LCTV area measures 1.32 inches (3.4 cm) diagonally, and is comprised of an array of 480 x 440 pixels, for a total of 211,200 pixels. The pixel size is 31  $\mu\text{m}$ , with center-to-center spacing between each pixel of 45  $\mu\text{m}$  vertically by 55  $\mu\text{m}$  horizontally, for an active area of 33%. The SLM is electrically addressed by a VGA-resolution (640 x 480 pixels) driver from *Mytec Inc.* (Toronto, Canada), which controls the device through an active matrix thin-film transistor (TFT) drive system (Duffey et al., 1995). Images files saved in *.bin* format are displayed via software designed to read the files and subsequently modulate the LCTV.

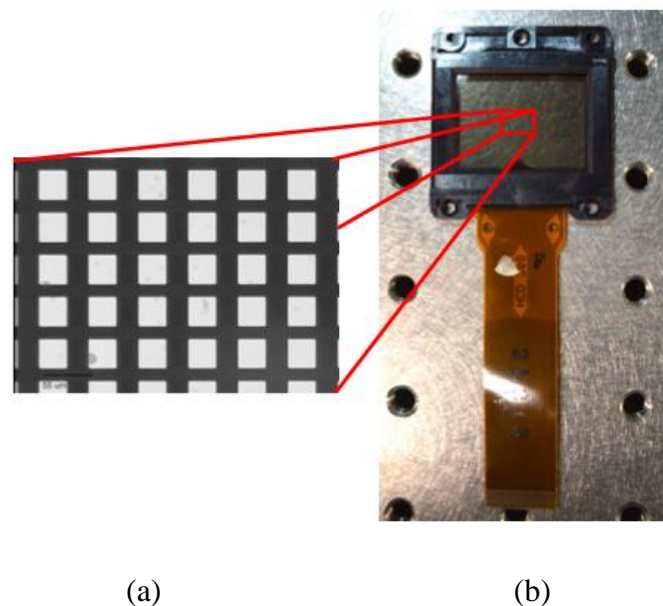


Figure 5.5. (A) 20x image of (b) Seiko-Epson LCTV used in the zero order phase contrast experiments. The LCTV panel measures 1.32 inches (3.4 cm) diagonally, containing 480 pixels in the horizontal direction, and 440 pixels in the vertical direction. The center-to-center spacing between each pixel is 45  $\mu\text{m}$  vertically by 55  $\mu\text{m}$  horizontally, for an active area of 33%.

In order to characterize our LCTV, we follow the method proposed by Neto et. al (1996). The goal is to determine the molecular director angle  $\psi_D$  and the twist angle  $\alpha$  of our device. We start by looking at the regime where the birefringence parameter  $\gamma=n\pi$ , with

$n=1,2,\dots$ . From Equation 3.35, we see that  $\gamma$  is a function of  $\alpha$  and  $\beta$ . When the orientations of the polarizer and analyzer are set parallel to each other, i.e.  $\psi_1=\psi_2=\psi$ , and both components are rotated simultaneously, we get the following result for Equation 3.41:

$$T = \left\{ \frac{\alpha}{\gamma} \sin\gamma \sin\alpha + \cos\gamma \cos\alpha \right\}^2 + \left\{ \frac{\beta}{\gamma} \sin\gamma \cos(\alpha - 2\psi + 2\psi_D) \right\}^2. \quad (5.1)$$

As  $\psi$  is rotated, maximum transmittance occurs when

$$\psi_{max} = \frac{\alpha}{2} + \psi_D \pm \frac{n\pi}{2}, \quad (5.2)$$

$$T_{max} = \left\{ \frac{\alpha}{\gamma} \sin\gamma \sin\alpha + \cos\gamma \cos\alpha \right\}^2 + \left\{ \frac{\beta}{\gamma} \sin\gamma \right\}^2. \quad (5.3)$$

Minimum transmittance occurs when

$$\psi_{min} = \frac{\alpha}{2} + \psi_D \pm \frac{(2n+1)\pi}{4}, \quad (5.4)$$

$$T_{min} = \left\{ \frac{\alpha}{\gamma} \sin\gamma \sin\alpha + \cos\gamma \cos\alpha \right\}^2. \quad (5.5)$$

According to Equations 5.2 and 5.4,  $\psi_{max}$  and  $\psi_{min}$  are independent of the coefficient of refraction  $\beta$ . This relation can be tested by rotating  $\psi$  in steps of  $5^\circ$  and measuring  $T$  at various gray levels. The results of these measurements for our LCTV are shown in Chapter 6. The resulting values for  $\psi_{max}$  and  $\psi_{min}$  should agree with the theoretical value  $|\psi_{max} - \psi_{min}| = 45^\circ$  in order for this method to hold (Neto et al., 1996).

Equation 5.1 dictates that when  $\gamma=n\pi$ ,  $T=\cos^2\alpha$  and is constant with the simultaneous rotation of  $\psi$ . Additionally, in this regime,  $T_{max} = T_{min}$ . The gray level at which  $T_{max} = T_{min}$  can be found by generating a plot of  $T_{min}/T_{max}$  vs. gray level, and determining the value of the abscissa at which  $T_{min}/T_{max}$  is a maximum. This value corresponds to  $\gamma=n\pi$ .

Now, we can relax the constraint of  $\psi_1=\psi_2$ . Considering again the regime in which  $\gamma=n\pi$ , we get the following expression for Equation 3.41:

$$T = \cos^2[\alpha + (\psi_1 - \psi_2)]. \quad (5.6)$$

The value for  $\alpha$  can be determined by setting  $\psi_1=0$  and measuring the output intensity as a function of the orientation  $\psi_2$ , and plotting a linear regression. With this result, the angle of the molecular director  $\psi_D$  can be obtained from Equations 5.2 or 5.4.

As mentioned in Section 3.3.2, we are interested in generating phase-modulated inputs that are then converted into amplitude distributions in the image plane of the phase contrast technique. In the phase-mostly modulation regime, the polarization axis of the input polarizer is parallel to the front molecular director of the LCTV, and the polarization axis of the analyzer is parallel to the axis of the rear molecular director of the LCTV (See Fig. 3.8). Therefore, we have that  $\psi_1 = \psi_D$ , and  $\psi_2 = \psi_D + \alpha$ , respectively. Subsequently, Equations 3.29 and 3.30 for  $T$  and, respectively, can be simplified as follows:

$$T = 1 - \alpha^2 \left( \frac{\sin\gamma}{\gamma} \right)^2 \quad (5.7)$$

$$\delta = \beta + \tan^{-1} \left( \frac{\beta}{\gamma} \tan\gamma \right) \quad (5.8)$$

The expressions above constitute the theoretical phase-mostly operation regimes for the LCTV. In order to determine  $T$  and  $\delta$  experimentally, we apply a technique used by Neto (1995) and Pizolato (2006). In this technique, the optimal angles for phase-mostly modulation of the LCTV are determined using a wedge shear plate interferometer (WSPI) placed in the optical path of the polarizer-LCTV-analyzer sandwich (see Figure 5.7). We use a red HeNe laser, the same used in most of our experiments, in order to carry out this procedure. By observing the interference pattern from the reflections of the wedged surfaces of the WSPI, it is possible to determine the phase difference between two different gray levels displayed by the LCTV, such as 0 and 255, for example. The relative phase  $\delta$  between fringes, in radians, is equal to  $2\pi$  multiplied by the interference fringe displacement  $\Delta$  divided by the fringe period  $\Lambda$  ( $\delta = 2\pi \Delta/\Lambda$ ) (Soutar et al., 1993). Phase-mostly modulation can be further optimized by rotating the polarizer and the analyzer until both gray levels display the same transmittance, while at the same time maintaining the maximum phase difference possible. The results for this procedure are shown on the next chapter.

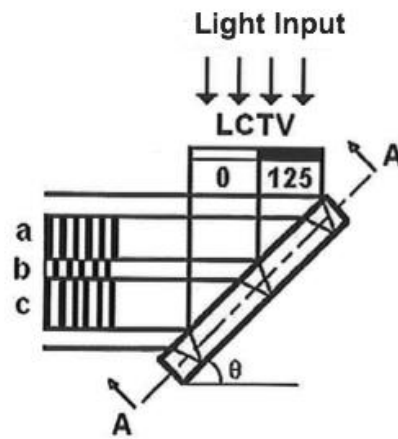


Figure 5.6. Optical arrangement for measuring phase difference between two gray levels using a wedge shear plate interferometer. Coherent light uniformly illuminates the LCTV, onto which regions with different gray levels have been programmed (0 and 125, respectively). Upon incidence on the interferometer, light passing through the different regions interferes in the central part of the interferometer due to the double reflection of the optical element. By measuring the shift between regions a and b, the phase difference between both gray levels can be inferred (Neto, 1995).



Figure 5.7. Wedged shear plate interferometer (WSPI) used for measuring the phase modulation range of our LCTV. The top diffused window is used for viewing the interference pattern generated after laser light is reflected from the front and back surfaces of the WSPI after passing through the Polarizer-LCTV-Analyzer sandwich.

### 5.3. The Zero Order Phase Contrast Technique

The zero order phase contrast technique is implemented experimentally as shown on Figure 5.7 below. We use the same laser used in our single optical trapping experiments as the coherent source (see Section 5.1). The laser is followed by polarizer P1 mounted in a rotation stage, which, according to the procedure described in Section 5.2, is adjusted in conjunction with analyzer P2 in order to maximize phase-mostly modulation of the LCTV. The output from P1 is followed by a 45° mirror (M), and the beam is redirected towards microscope objective MO1 (P/N M-40X, Newport Cor. CA, USA), which has a 40x magnification. The beam is then spatially filtered (SF) using a 25  $\mu\text{m}$  pinhole. The divergent light is collected and collimated by a 150 mm EFL plano-convex lens (L1), whose output uniformly fills the entire active area of the LCTV. The phase-modulated output of the LCTV is incident upon L2 (EFL = 100 mm), which forms a  $4f$  correlator with L3 (EFL = 50 mm). A 300  $\mu\text{m}$  diameter zero order filter ZOF is placed in the Fourier plane of the correlator, suppressing the first and higher diffraction orders. This diameter size was found to be the most appropriate after performing image contrast tests with several pinhole sizes (50, 100, and 200  $\mu\text{m}$ ). Finally, the resulting intensity distribution is imaged by a CCD camera.

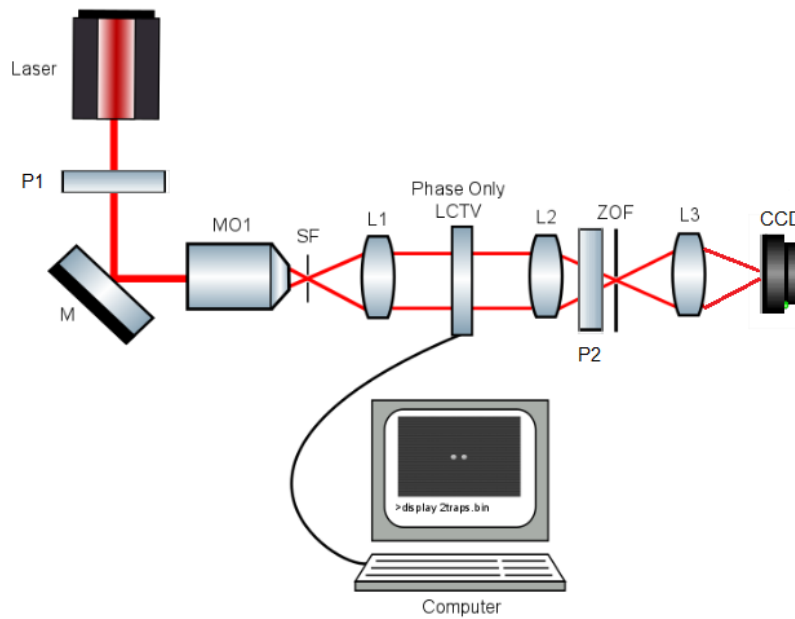


Figure 5.8. Experimental setup of the zero order phase contrast technique. The output from the laser is spatially filtered using a 40x microscope objective (MO1) and a 25 $\mu\text{m}$  pinhole (SF). Lens L1 collimates and uniformly distributes the light input onto the LCTV. The phase-modulated light of the LCTV is spatially filtered by the zero order filter ZOF in the Fourier plane of the  $4f$  correlator formed by lenses L2 and L3, producing intensity distributions in the image plane that can be recorded using a CCD camera. Polarizers P1 and P2 are used to maximize the phase modulation of the LCTV.

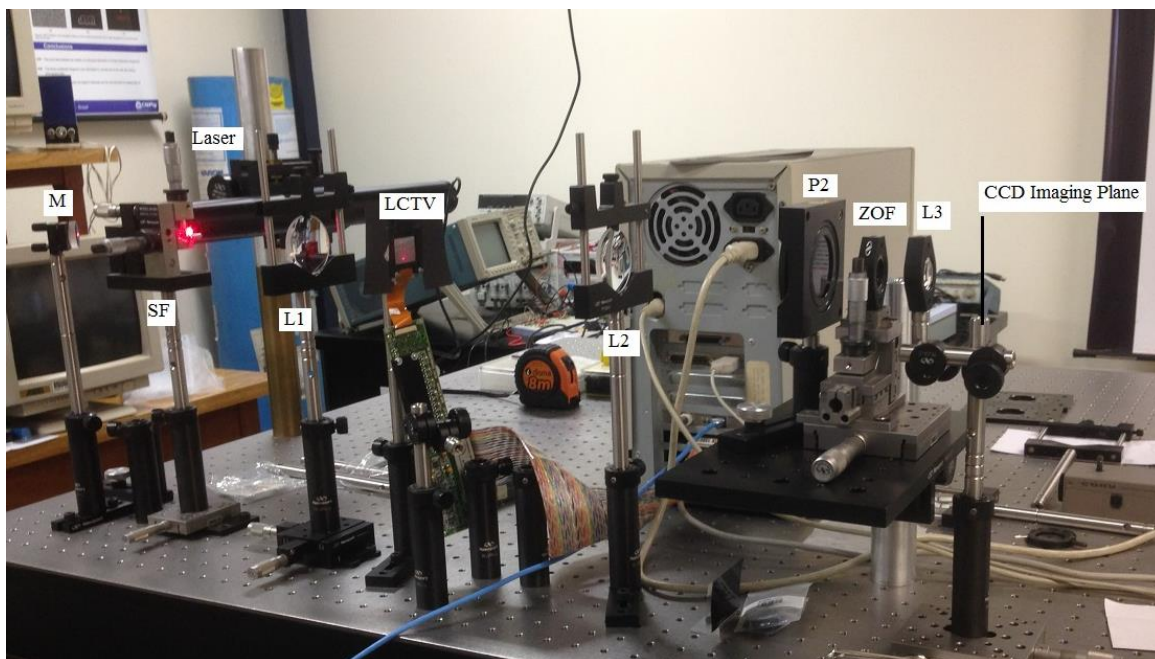


Figure 5.9. Experimental setup of the zero order phase contrast technique in the Telecommunications lab at the EESC. The zero order filter (ZOF) is located in back focal point of the first  $4f$  correlator lens L2. The imaging plane is located a focal distance away from lens L3.

As mentioned in Section 3.2, we use a macropixel configuration in order to code the phase information onto the LCTV. Each macropixel in the diffractive element is divided into two phase regions, one that is modulated in relation to the gray-level information  $a(x,y)$  contained in the image, and the other modulated by the phase value  $\exp(j\pi)$  (See Figure 3.3). In our experiments, we take an image formatted in *.jpg*, *.bmp*, or other image formats and use Matlab<sup>®</sup> (Mathworks, Inc.) in order to convert the pixels corresponding to the  $\exp(j\pi)$  phase modulation into the appropriate gray level value, which is determined from the results of the characterization procedure described in Section 5.2. The images are then saved in *.bin* format for reading and display on the LCTV. The following is an example of a phase image coded onto the liquid crystal television for implementation of the zero order phase contrast technique:

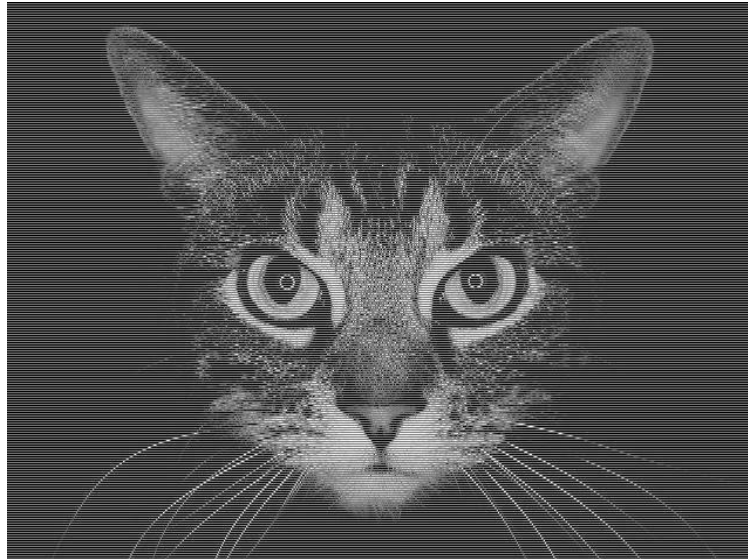


Figure 5.10. Image coded into LCTV for implementation of the zero order phase contrast technique. Every other row in the image has the gray level value corresponding to the phase modulation  $\exp(j\pi)$ . Size of image: 640 x 480 pixels.

## 5.4. Integration of the Zero Order Phase Contrast Technique in Optical Trapping System

Figure 5.11 illustrates the optical setup used in our multi-beam optical trapping experiments based on the zero order phase contrast technique. In order to achieve enough power density in the trapping plane using the zero order phase contrast technique, it was necessary to use a different, more powerful laser source. To that end, we replaced the previously used 632.8 nm HeNe laser with a 976 nm semiconductor butterfly laser (P/N BL976-SAG300, Thorlabs, Inc., New Jersey, USA), which can output a maximum of 300 mW at a typical operating current of 470 mA. The current and temperature of the laser were controlled by compatible stand-alone drivers (P/N LDC205C, TED200C, Thorlabs, Inc., New Jersey, USA) which ensured stable operation of the device. This change in operating wavelength of the system does come with a disadvantage: given that the local birefringence  $\beta$  of the LC cell is inversely proportional to the source wavelength (see equation 3.25), a larger wavelength results in a smaller change in birefringence, which implies a shorter modulation range  $\delta$  (see equation 5.8). This translates into a loss of contrast in the image plane. Nevertheless, this was a necessary sacrifice given that we did not have any other shorter-wavelength lasers available in our lab.

The fiber-coupled output from the laser is connected to a beam collimator (P/N F810FC-780, Thorlabs Inc., New Jersey, USA) via an FC/APC fiber connector, producing a beam of approximately 7.5 mm in diameter. After being redirected by a 45° mirror, the beam is incident upon a half wave-plate, which is used to control the polarization orientation. It is worth noting that this component is essential in optimizing the phase modulation range of the LCTV. Irises Ir1 and Ir2 located before the LCTV and after L2, respectively, are used in order to optimize the contrast of the intensity distribution, and to remove undesired halo light resulting from the phase contrast path (Eriksen et al., 2002). After passage through the LCTV, the modulated output is focused by lens L1 (EFL=100 mm), forming a  $4f$  correlator with lens L2 (EFL=50 mm). Polarizer P, located between L1 and L2, is used to optimize the phase modulation contrast. A 300  $\mu\text{m}$  diameter pinhole located in the back focal plane of L1 performs the higher diffraction order filtering operation, resulting in the formation of an intensity distribution at the back focal plane of L2.

The output from the zero order phase contrast system is coupled via lens L3 (EFL=300mm) into an adapted upright microscope (Edmund Optics, New Jersey, USA). A

shortpass dichroic mirror DM (P/N DMPS805, Thorlabs Inc., New Jersey, USA) with an average transmission of 90% in the 400-788 nm range and a reflectivity of 95% in the 823-1300 nm range reflects the 976 nm optical tweezer intensity pattern while transmitting visible light, thus allowing visualization of the sample plane by the CCD camera. Through careful alignment, the infrared light is coupled to the back aperture of an Olympus UPlanFL N oil immersion microscope objective (MO). This microscope objective, previously used in our single trap experiments, has a magnification of 100x, a numerical aperture of 1.3, and a working distance of 0.2 mm. The total demagnification of the pattern projected onto the SLM is 1/300. Therefore, a single 31- $\mu\text{m}$  LCTV pixel corresponds to 0.10  $\mu\text{m}$  in the optical trapping plane. Finally, lens L4 (EFL=150 mm) is used to couple the sample plane images onto a CCD camera. Figures 5.12, 5.13, and 5.14 show the actual setup implemented in the lab.

Once the system is aligned, we followed the same procedure as that described in Section 5.1 for preparing and optically aligning the sample.

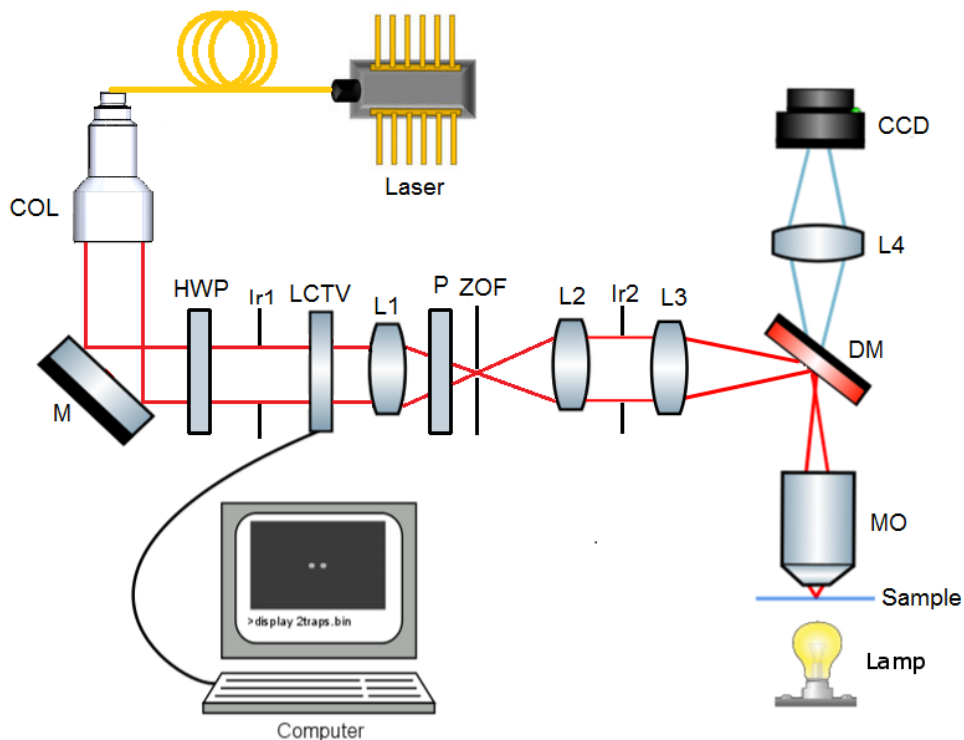


Figure 5.11. Optical path for optical trapping system based on the zero order phase contrast technique. The intensity distributions generated by the phase contrast system are coupled by lens L3 and dichroic mirror DM into an adapted upright microscope for projection onto the sample plane.



Figure 5.12. Experimental setup of the integrated zero order phase contrast and optical tweezers system. The laser source is not shown. The laser output from collimator COL (left side of figure) is directed into the zero order phase contrast system by mirror M. The 4f correlator is formed by the LCTV, L1, and L2. The zero order filter ZOF is located in the back focal plane of L1.

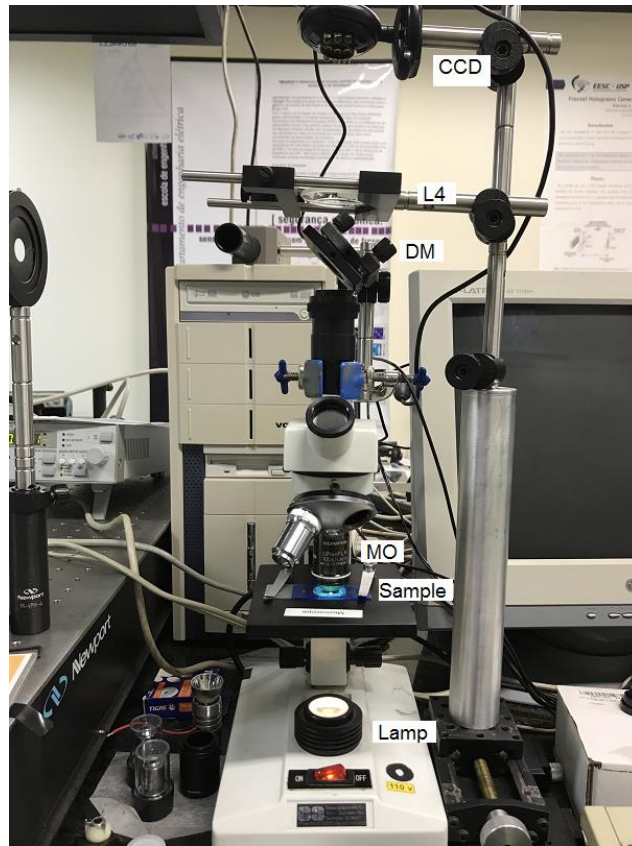


Figure 5.13. Adapted microscope setup for optical trapping. The output from the phase contrast system is coupled from the left onto the dichroic mirror (DM) fixed on a tip/tilt mount for alignment. The sample holder is adjusted vertically in order to position the sample in the focal volume of the light focused by the microscope objective (MO).



Figure 5.14. The butterfly type, fiber coupled laser source, shown mounted on the top left side, is driven by stand-alone current and temperature controllers.

Since our experiment was mainly proof-of-principle, the focus of our tests consisted on obtaining static, dual optical tweezers in the sample plane. To that end, we experimented with two dots, ranging in diameter from 11 to 19 pixels, which corresponds to an approximate range in the tweezer plane of 1.1-1.9  $\mu\text{m}$ . We also experimented with an edge-to-edge separation between the dots ranging from 7 to 15 pixels, which corresponds to a range of 0.7 to 1.5  $\mu\text{m}$ . Figure 5.15 shows the dual pattern used for the bulk of our experiments.

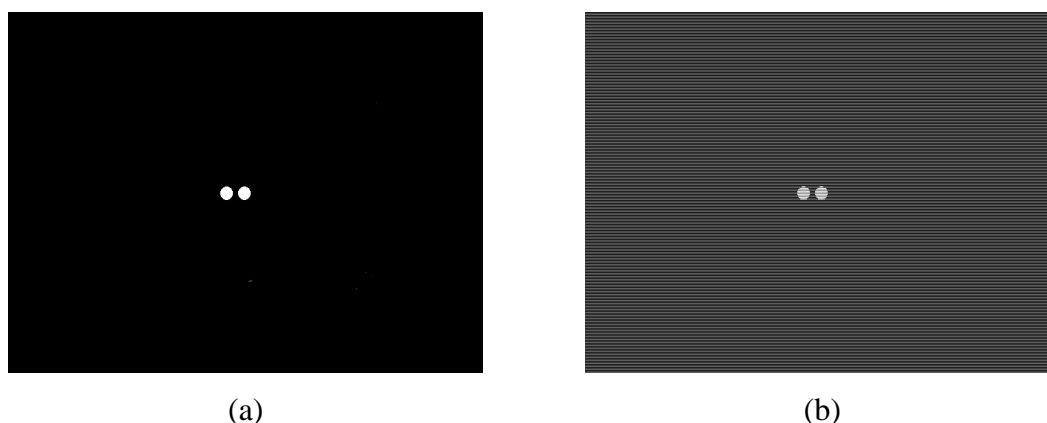


Figure 5.15. Dual pattern used in most trapping experiments (640 x 480 pixels). The diameter of each dot is 18 pixels. (a) Original image. (b) Image projected onto LCTV.

Other patterns were also tested. However, we did not pursue them due to the relatively low concentration of beads in the sample, and the rather coarse method of moving particles onto the trapping field, which consisted of lightly tapping the sample slide from all four sides.



Figure 5.16. (a) 3-dot and (b) 4-dot patterns projected in trapping experiments (640 x 480 pixels).

## 6 RESULTS

In this chapter, we present the results of our experiments, which include measurements, optical images, and simulations. The sections are organized in the same order as the Methods and Materials chapter (Ch.5), starting with the experimental results of the single optical trap, followed by the characterization results of the LCTV used in our experiments. We then present the optical results for the zero order phase contrast technique, followed by the results obtained from the multiple optical tweezers experiments.

### 6.1. Single Optical Trap

Figure 6.1 below shows sequential optical results for the single optical trap implemented using the 60x objective described in the Methods and Materials section (see Figure 5.1). In this short sequence, the particle is trapped in the laser focus in (a). Upon briefly blocking the trapping beam path the particle is released from the trap in (b), allowing visualization of the focal spot of the trapping beam. The trap exerts a transversal force onto the particle within a limited range of the laser focus, bringing the free particle (c) back towards the optical tweezer field, trapping the particle again (d). Figure 6.2 shows non-sequential single optical trap images obtained with the 100x objective. In order to bring particles closer to the laser focus, the sample slide was gently displaced in its mount. In both experiments, we observed that when briefly blocking the beam path, the trapped particle would almost immediately leave the trapping area, quickly returning to the location of the beam focus once the beam path was unblocked. However, we noticed that the 60x trap had a higher trapping efficiency than the 100x trap. A plausible explanation for this effect is that while the trapping beam filled 78% of the back aperture of the 60X objective, it only filled 58% of the back aperture of the 100X objective, which very likely decreased the stiffness of the trap by affecting the balance between the gradient and scattering force components.

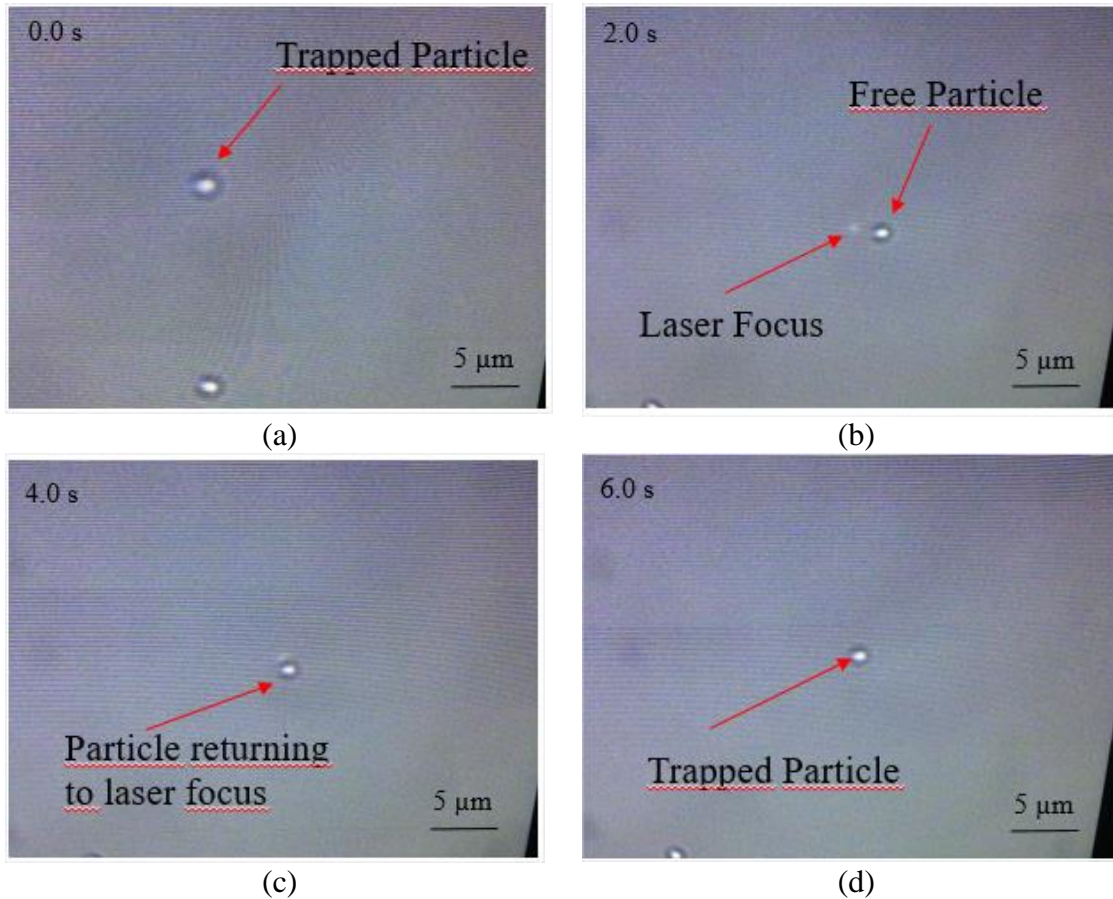


Figure 6.1. Sequential optical results for single optical trap using 60x, 0.85 NA microscope objective. The particle is trapped in (a). Upon briefly blocking the trapping beam path the particle is released from the trap in (b), allowing visualization of the focal spot of the trapping beam. The trap exerts a transversal force onto the particle within a limited range of the laser focus, bringing the free particle (c) back towards the optical tweezer field, trapping the particle again (d).

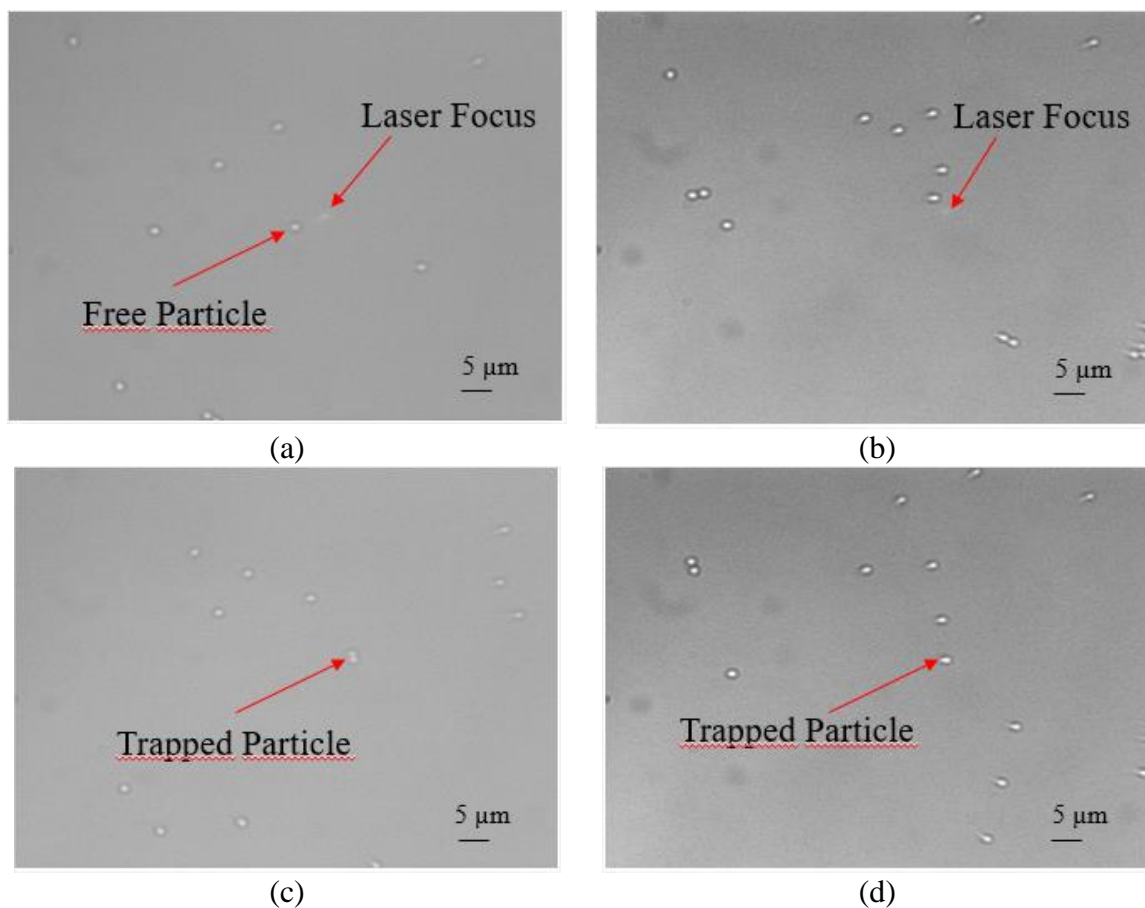


Figure 6.2. Non-sequential optical results for single optical trap using 100x, 1.3 NA microscope objective. The particles are brought close to the laser focus by gently tapping on the sample slide. The laser focus can be observed in (a) and (b). In (c), two particles are trapped in the laser focus field.

### 6.1.1. Qualitative Evaluation of Trapping Stiffness as a Function of Laser Power

A simple experiment was devised in order to measure the optical power available at the sample plane and the minimum power at which a trap can be observed in our 60x system. We placed a polarizer in the path of the linearly-polarized HeNe laser source (P in Figure 6.3 below), allowing us to control the power available at the sample plane for optical trapping. Starting with the polarization orientation of the laser, the polarizer, and the polarization-sensitive beam splitter aligned, we measured the power available at the sample plane from  $0^\circ$  to  $80^\circ$ , observing the stiffness of the optical trap after each measurement at each angle step. Figure 6.4 shows how the measurement was performed.

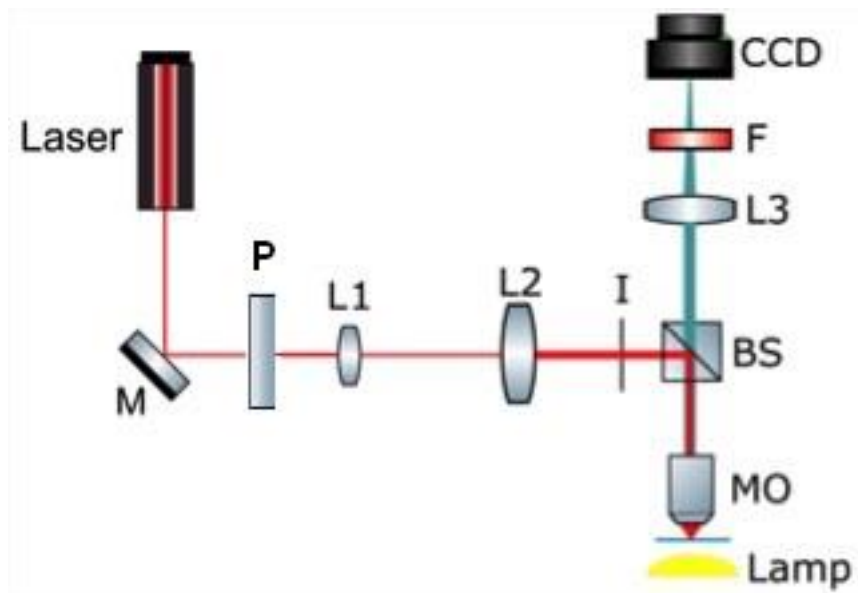


Figure 6.3. Optical setup for qualitative evaluation of single trap stiffness as a function of power at the sample plane. By rotating polarizer P from  $0^\circ$  to  $80^\circ$ , the power at the sample plane was adjusted. The trap stiffness was evaluated at several power levels.



Figure 6.4. The power measurements at the sample plane were performed using a beam profiler (P/N BP209-VIS, Thorlabs Inc, New Jersey, USA) placed at the focus of the microscope objective (MO in Figure 6.3). It was necessary to remove the sample stage in order to collect the data.

The maximum available power at the sample plane was 3.50 mW, which, while delivering sub-pN force (Neuman; Block, 2004), was still enough to efficiently trap the fused silica particles without any visible jitter. A qualitative stiffness value of 1.0 was assigned to the most stable, efficient trap, while a value of 0.0 was assigned to the absence of optical trapping. Figure 6.5 below shows the results of our measurements:

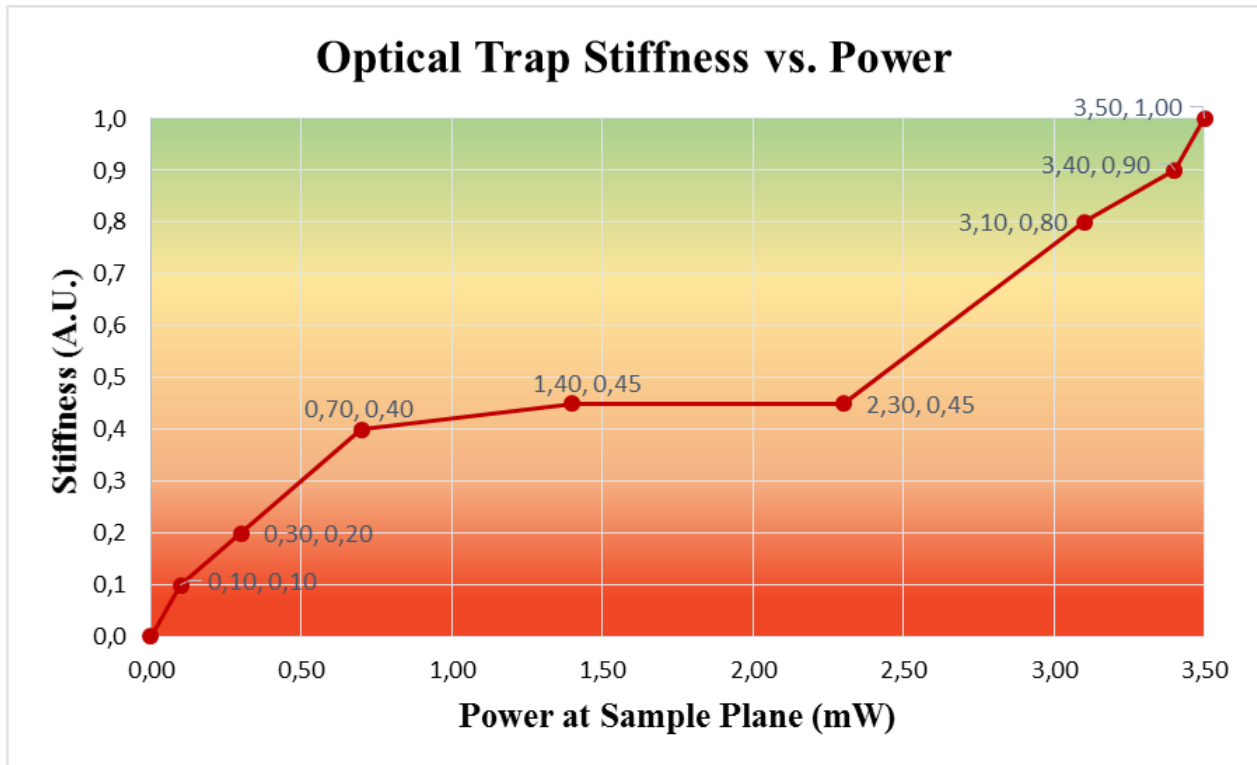
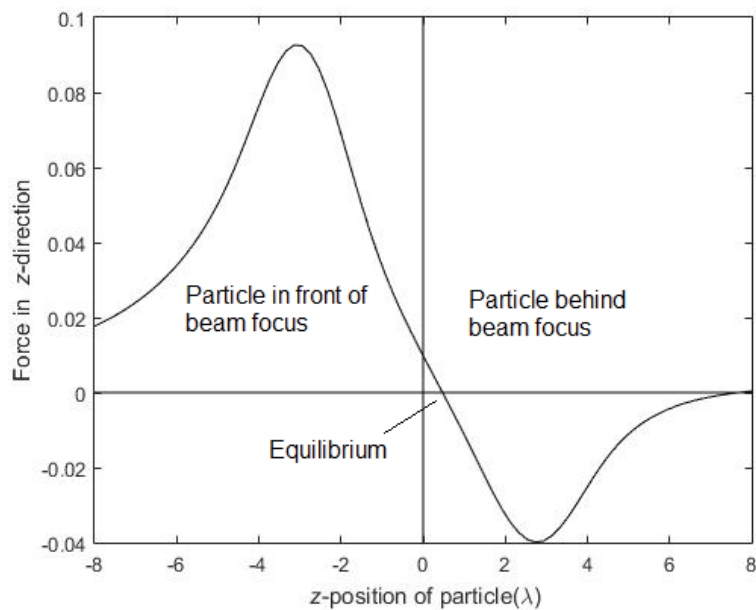


Figure 6.5. Qualitative results for trap stiffness as a function of power available at the sample plane. Measurements in the green gradient field are considered to imply stable optical trapping. The observed stiffness of the optical trap was somewhat constant in the yellow-orange power range (0.70-2.30 mW), albeit with some mechanical jitter. Trap stiffness falls sharply at power values below 0.50 mW.

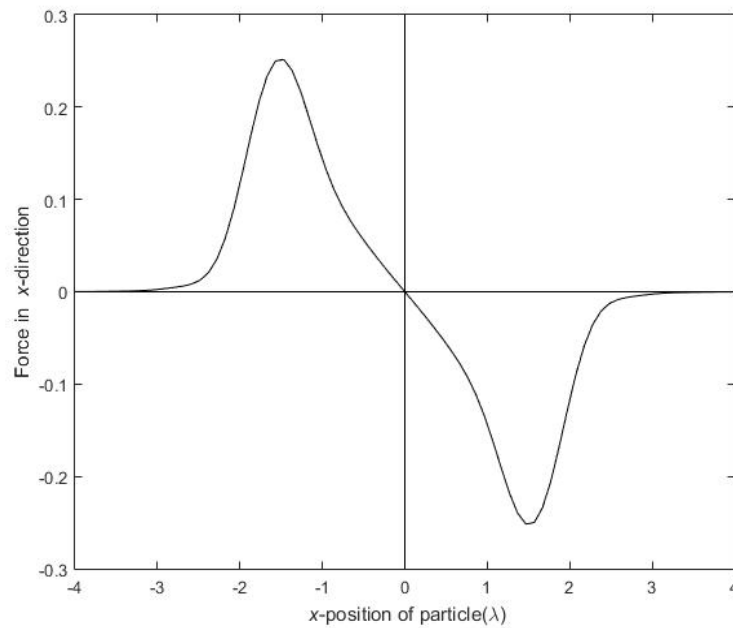
We found that the optical trap was the most stable at power values between 3.00 and 3.50 mW, with small differences in jitter. The lowest value for which a constant, yet jittery, trap could be observed was 700  $\mu$ W. Lower values presented increase jitter and did not result in constant, lasting traps.

### 6.1.2. Quality Factor of the Forces Acting on a Micro-Particle near the Beam Focus

Nieminen et al. (2007b) published a very useful computational toolbox compatible with Matlab<sup>®</sup> that can be used to calculate, among other parameters, quality factors of the axial and radial forces acting on a micron-sized particle near the focus of a Gaussian trapping beam. The toolbox uses the T-matrix method, which, based on the assumption of linearity between incident and scattering light fields, describes the forces acting on a trapped particle through relatively simple matrix operations. Trappability and maximal reverse axial and radial forces can be calculated based on particle size, the refractive indices of the medium and the particle, the numerical aperture of the microscope objective, and the wavelength of the laser source. This toolbox can be useful in determining the feasibility of implementing an optical trap for a given set of experimental conditions. We performed this simulation for our 60x system, and obtained the following results:



(a)



(b)

Figure 6.6. Quality factors for the asymmetrical (a) axial ( $z$ -direction) and symmetrical (b) radial ( $x$ -direction) forces as functions of particle position for 60x optical trapping system. Calculated from (Nieminen et al. 2007b)

A quick analysis of Figure 6.6(a) reveals that the axial force is negative for a range of distances beyond the beam focus, and it is smaller than either the maximum forward scattering force or the maximum radial force (b). This negative force is the force responsible for optical trapping (Nieminen et al. 2007a). Furthermore, applying this model to our 60X system, we can deduce that the equilibrium position is located approximately  $0.5\lambda$  downstream from the beam focus, that is,  $0.5(0.6328 \mu\text{m}) = 0.3164 \mu\text{m}$  beyond the equilibrium position.

## 6.2. Characterization of Liquid Crystal Television

As mentioned in Section 5.2, the goal in the characterization of our LCTV is to find the parameters of the twist angle  $\alpha$  and molecular director  $\psi_D$ . In the method used, we empirically find the values for  $\Psi_{max}$  and  $\Psi_{min}$  (see equations 5.2 and 5.4) and solve for the unknowns. We found these values by setting the orientations of the input and output polarizers parallel to each other (i.e.  $\psi_1 = \psi_2 = \psi$ ) and measuring the transmission every 5 degrees for increasing gray level values from 0 to 175. Figure 6.7 shows the results of our measurements. The vertical lines correspond to the  $\Psi_{max}$  and  $\Psi_{min}$  angles, which are  $42^\circ$  and  $90^\circ$ , respectively. These were averaged from the maximum and minimum transmission from all the gray levels. This method holds given that the result  $|\psi_{max} - \psi_{min}| = 42^\circ$  is not far from the required theoretical value of  $45^\circ$ .

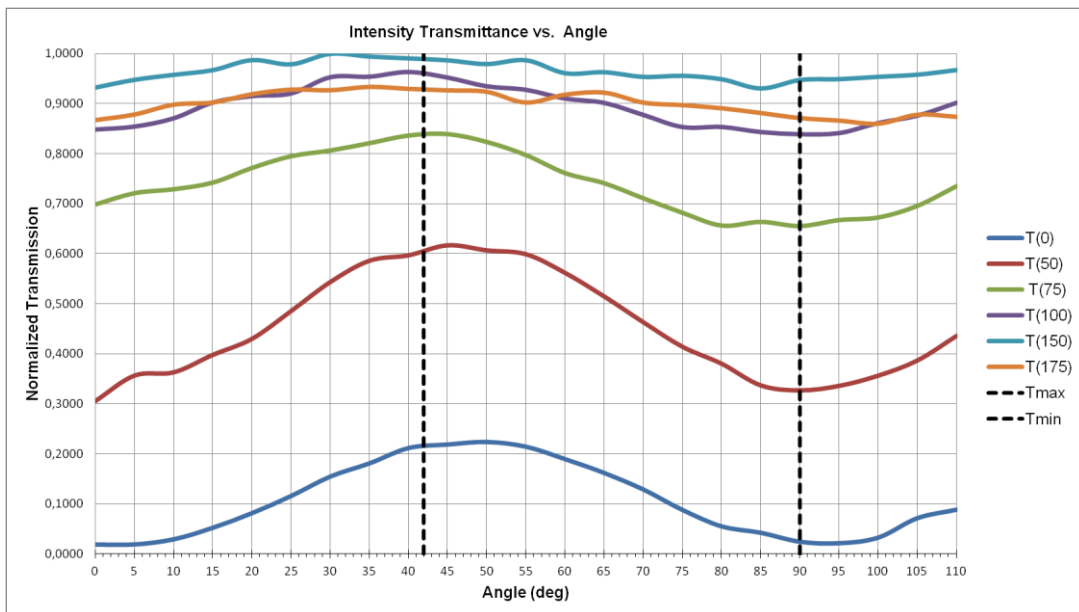


Figure 6.7. Normalized transmission curves for gray levels between 0 and 175. The orientations of the polarizer and analyzer were set parallel to each other and rotated simultaneously. The dashed lines correspond to the angles  $\Psi_{max} = 42^\circ$  and  $\Psi_{min} = 90^\circ$ .

The next step requires finding the gray level at which  $T_{max} = T_{min}$ , which corresponds to  $\gamma = n\pi$ . Using the results from our transmission measurements, we plotted  $T_{min}/T_{max}$  vs. gray level, and determined the value of the abscissa at which  $T_{min}/T_{max}$  is a maximum. Figure 6.8. shows our results. The  $\gamma = n\pi$  value is 150. This value was chosen due to the decrease of  $T_{min}/T_{max}$  at 175 and subsequent increase at 200, which is a behavior that corresponds to values where  $\beta = 0$ , where the theory no longer holds (Neto et al. 1996).



Figure 6.8.  $T_{min}/T_{max}$  vs. gray level. The dashed line at gray level indicates the gray level at which  $\gamma=n\pi$ .

Now, the value for the twist angle  $\alpha$  was determined by projecting the gray level value of 150 onto the LCTV, setting  $\psi_1=0$  and measuring the output intensity as a function of the orientation  $\psi_2$ , and plotting a linear regression. The results are shown on Figure 6.9 below. The twist angle of our LCTV was found to be  $88^\circ$ . The high  $R^2$  value shows a good linear relationship between  $\cos^{-1}(T)^{1/2}$  and  $\psi_2$  (see equation 5.6).

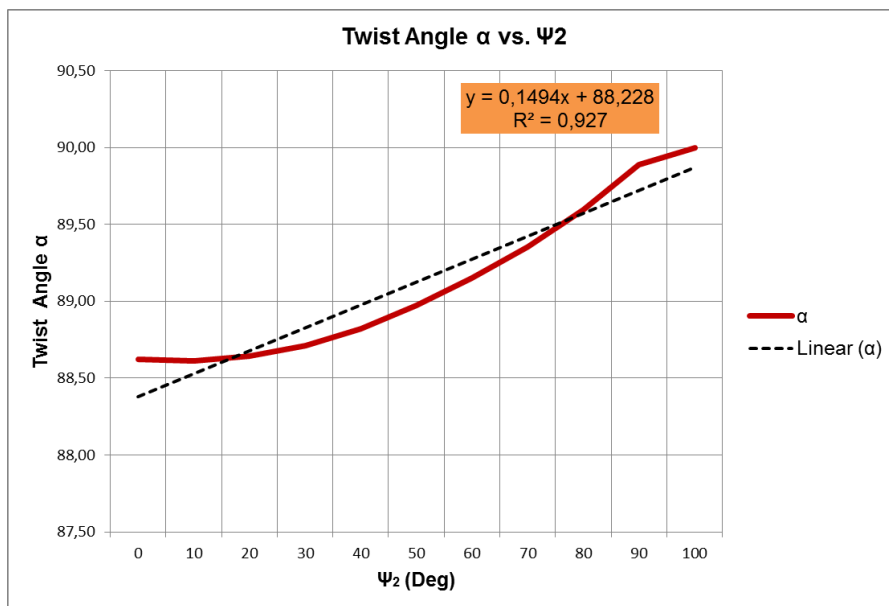


Figure 6.9. Determination of twist angle  $\alpha$ . The y-intercept value of 88 corresponds to the twist angle.

Using equations 5.2 and 5.4, it is a straight-forward operation to find the value for the molecular director  $\psi_D$ . For the LCTV used in our experiments, the molecular director was found to be  $88^\circ$ .

The last step in the characterization of our LCTV involves finding the modulation depth in the phase-mostly modulation regime based on GSL. By using the optical arrangement shown on 5.6 and finding the relative phase between the reference gray scale level of zero and subsequent levels up to 255, we found that when used with a 633 nm laser source, our LCTV has a maximum modulation depth of 4.5 radians. The input and output polarizer angles were aligned at  $-10^\circ$  and  $117^\circ$ , respectively, which coincide with the angles used by Pizolato in (2006). See Figure 6.10 below.

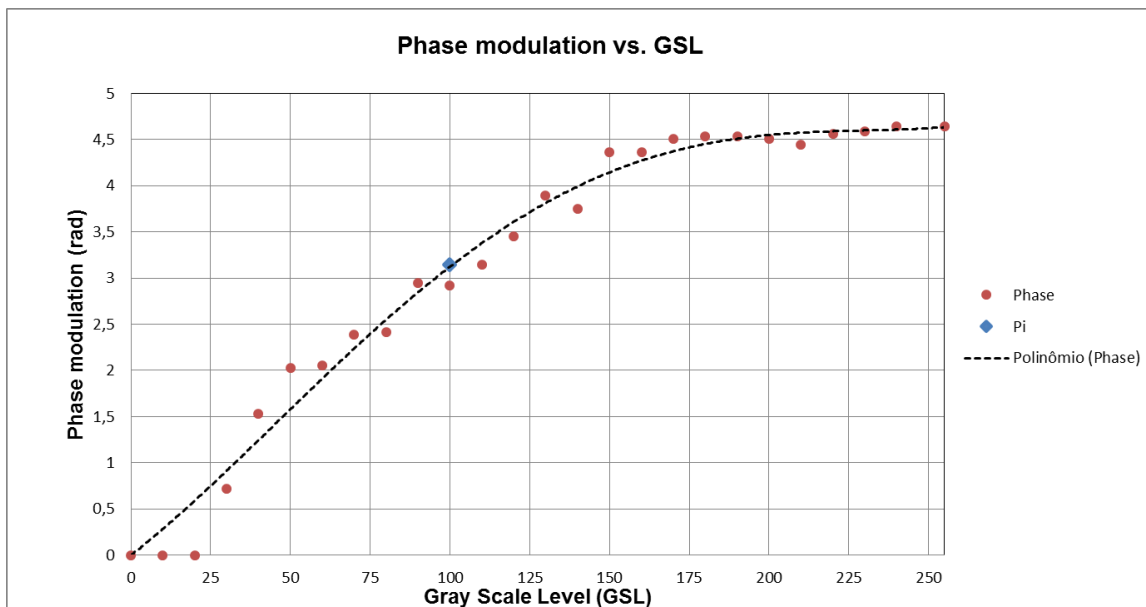


Figure 6.10. Phase modulation curve for LCTV used in our experiments with a 633 nm HeNe laser source. The input and output polarizer angles were aligned at  $-10^\circ$  and  $117^\circ$ , respectively, for phase-mostly modulation.

In the plot above, the point for  $\pi$  modulation is marked in blue. This point corresponds to the gray level value of 100 and therefore this GSL is used in the configuration of our images for macropixelation. See Figure 3.3 for reference.

As an example, below is a fringe interference image for levels 0 and 255 from our WSPI. With a measured fringe period of 4.52 mm and a fringe displacement of 3.34 mm, the resulting relative phase between the two gray scale levels is 4.64 rad.

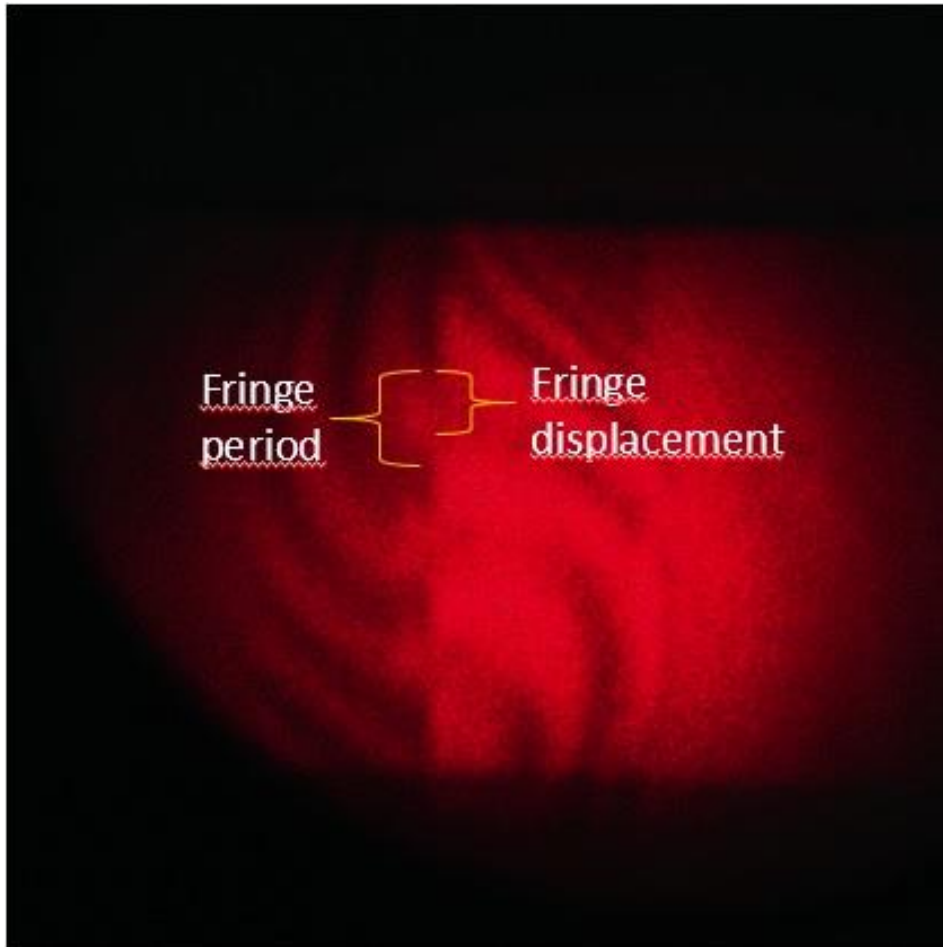


Figure 6.11. WSPI image for gray scale levels 0 and 255. There is considerable distortion of the fringes due to spherical aberration from the lens system. With a measured fringe period of 4.52 mm and a fringe displacement of 3.34 mm, the resulting relative phase between the two gray scale levels is 4.64 rad.

### 6.3. Optical Results of the Zero Order Phase Contrast Technique

In this section, we show optical results from the implementation of the zero order phase contrast technique. The images were recorded by a CCD camera in the image plane of the second lens in the  $4f$  correlator of the phase contrast system (L3 in Figure 5.8).

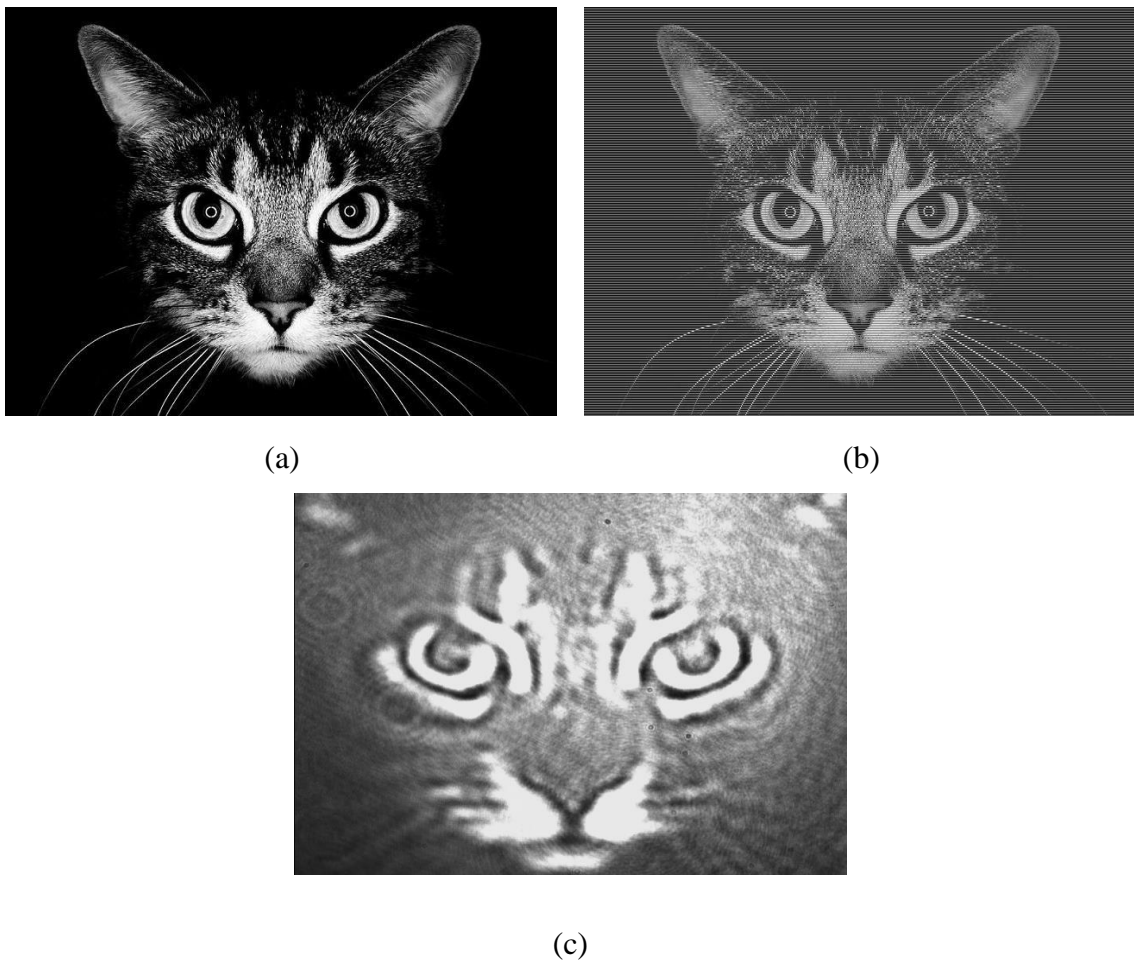


Figure 6.12. Zero order phase contrast results for image of cat (640 x 480 pixels). (a) Original GSL image. (b) Macropixel configuration image used for modulation of LCTV. (c) Optical result captured with CCD camera.

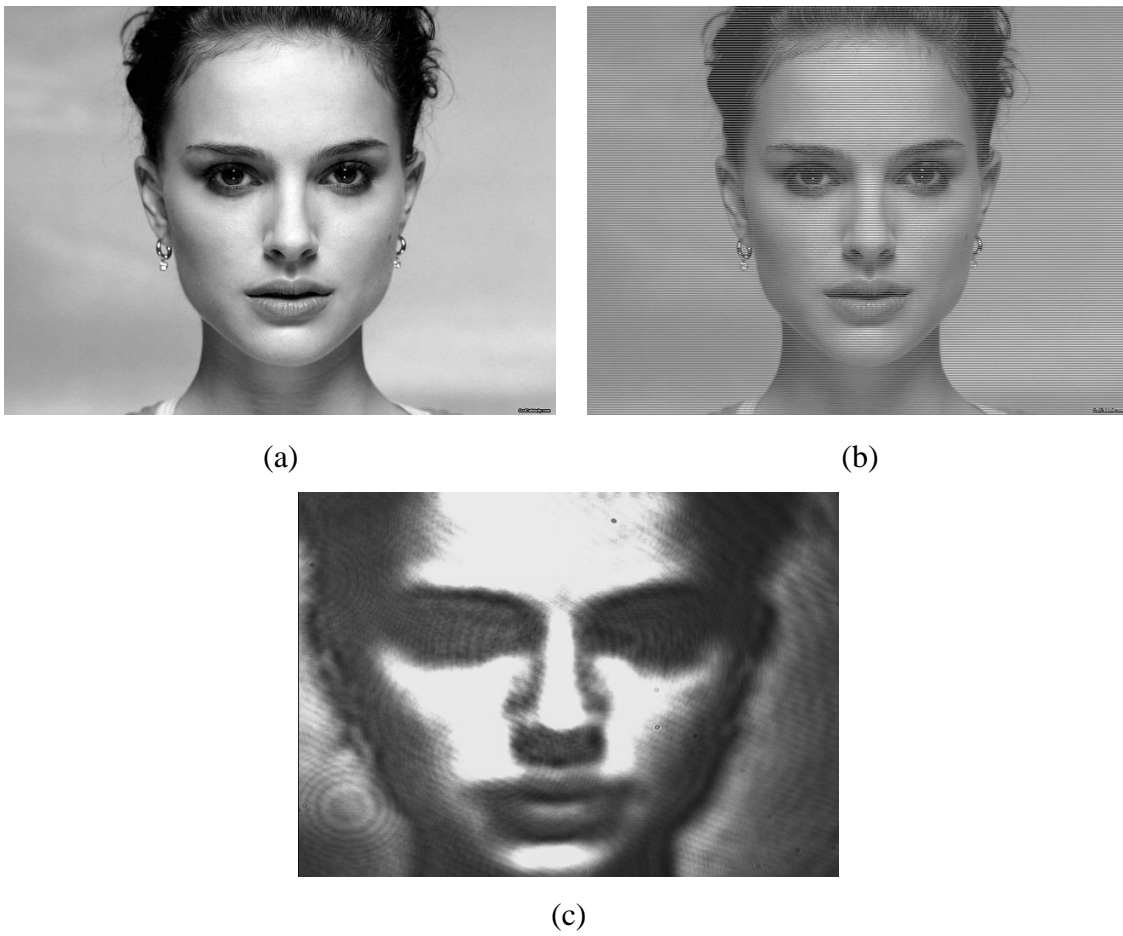


Figure 6.13. Zero order phase contrast results for image of woman (640 x 480 pixels). (a) Original GSL image. (b) Macropixel configuration image used for modulation of LCTV. (c) Optical result captured with CCD camera.

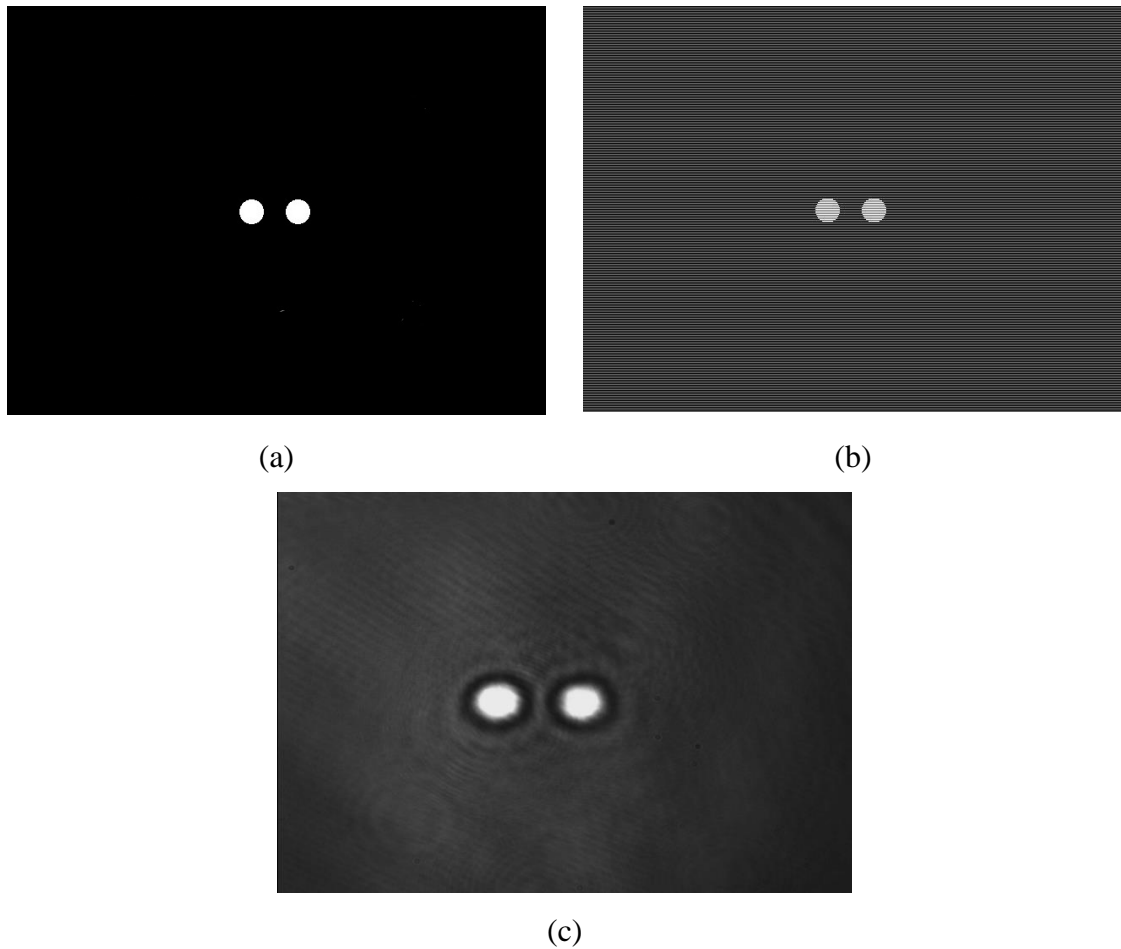


Figure 6.14. Zero order phase contrast results for image of 2-trap pattern (640 x 480 pixels). (a) Original binary image. (b) Macropixel configuration image used for modulation of LCTV. (c) Optical result captured with CCD camera.

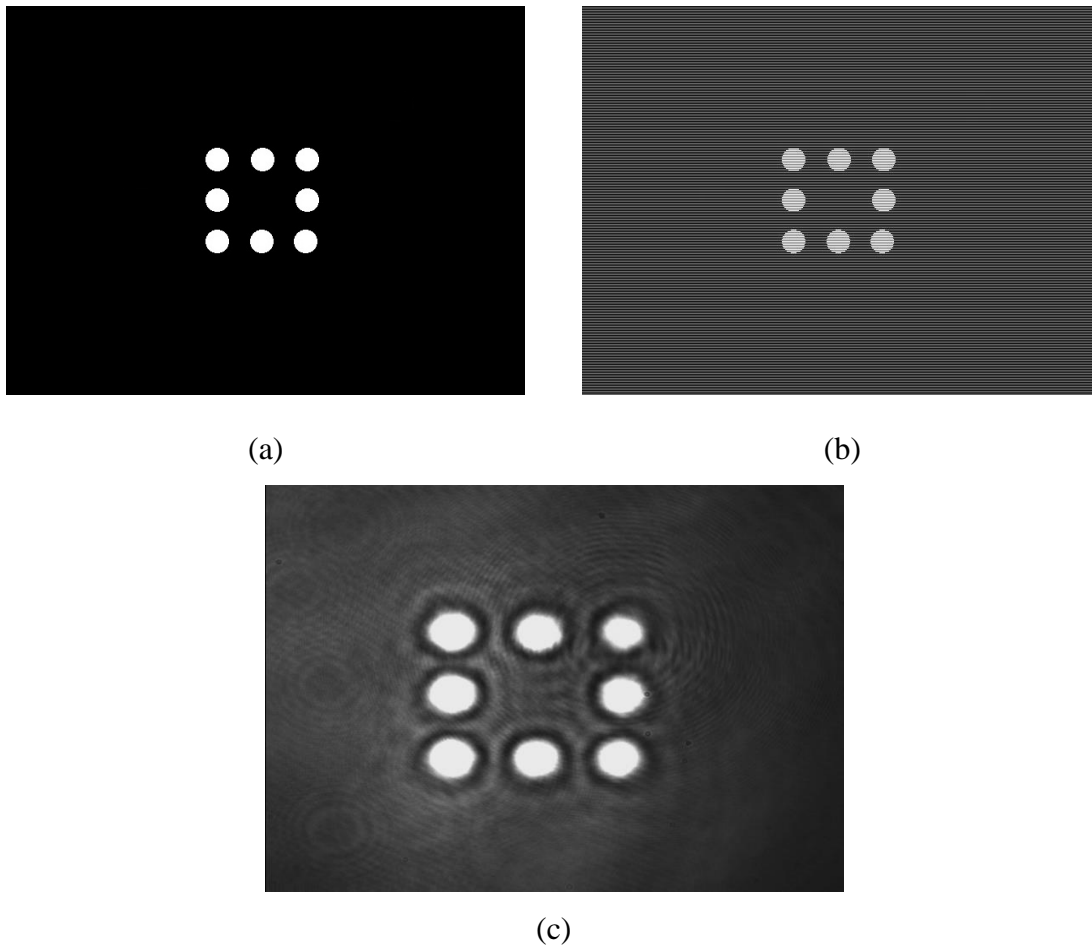


Figure 6.15. Zero order phase contrast results for image of 8-trap pattern (640 x 480 pixels).  
(a) Original binary image. (b) Macropixel configuration image used for modulation of LCTV.  
(c) Optical result captured with CCD camera.

The zero order efficiency  $e_{zero}$  was measured for each phase contrast image. Below are the results:

Phase Contrast Image	$e_{zero}$
Cat	30.0%
Woman	32.0%
Two-trap pattern	31.3%
Eight-trap pattern	31.5%

Table 6.1. Measured zero order efficiency for images obtained in the zero order phase contrast technique.

The relatively low zero order efficiency is primarily caused by the inter-pixel dead space of the LCTV, which results in transfer of energy to higher diffraction orders. Images projected onto the LCTV with high spatial frequency features such as that of the cat suffer from higher energy loss. Thus the lower zero order efficiency in our results. As an example, below is an image taken in our lab that shows the pattern generated by the LCTV for one of the zero order phase contrast images. The zero order filter located behind the infrared sensor card (ZOF in Figure 5.11) allows transmission of only the central diffraction order (i.e. the zero order).



Figure 6.16. Diffraction pattern generated by the LCTV used in our experiments projected onto an infrared-sensitive card. Energy is lost to higher diffraction orders due to the mesh structure of the LCTV.

## 6.4. Integration of the Zero Order Phase Contrast Technique in Optical Trapping System

In this part of our experiments, we start by evaluating the effect of macropixelation (i.e. modulating every other row in the LCTV with a fixed phase value of  $\pi$ ), which is a central part of the zero order phase contrast technique. Two dual trap images are projected onto the LCTV sequentially, one without macropixelation (Figure 5.15a) and one with macropixelation (Figure 5.15b.) The trapping field distribution is captured by the CCD in the microscope system. It is worth noting that none of the optical components were manipulated in order to obtain the images. Results below:

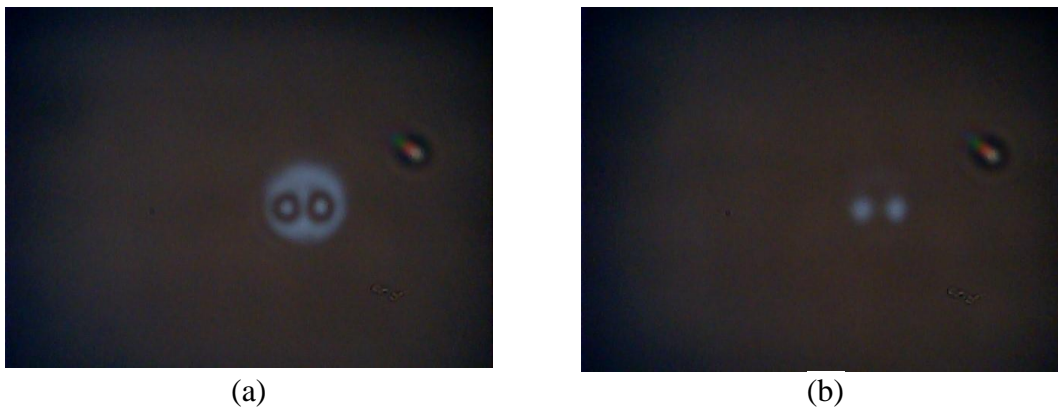


Figure 6.17. Optical trapping plane images collected by CCD camera of dual beam patterns without and with macropixelation. It is clear that pattern (b) displays the most contrast between the background and the actual structured light patterns.

The images above further validate the fact that the zero order phase contrast technique can produce high-contrast image distributions that can be used for optical trapping.

Figure 6.18 shows the trapping plane image distributions of three and four-dot optical trapping patterns:

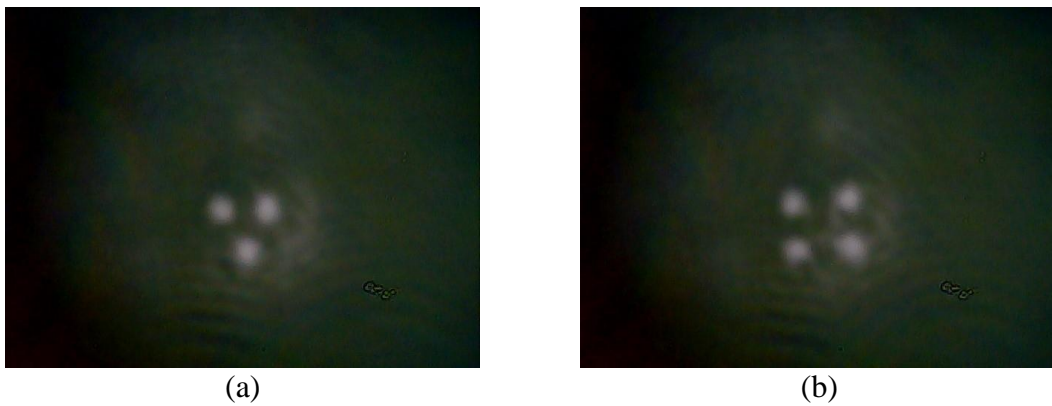
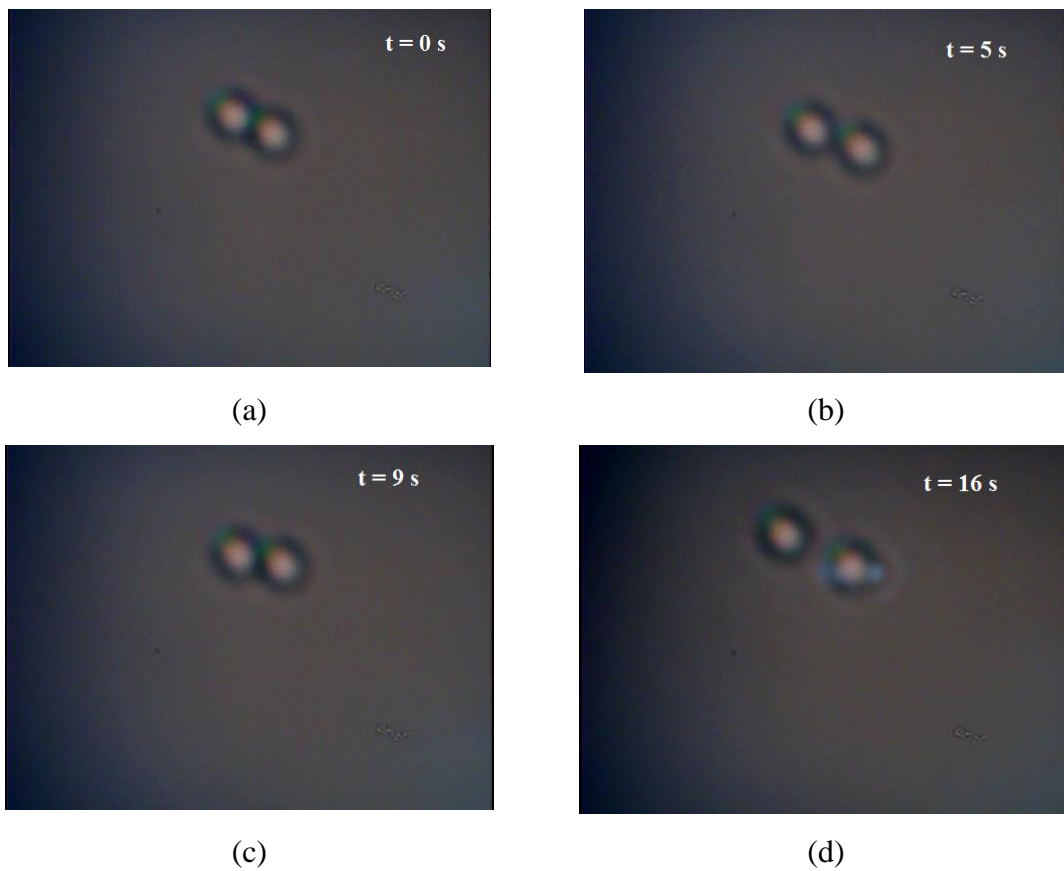


Figure 6.18. (a) three and (b) four dot pattern projections on trapping plane.

As mentioned in the Methods and Materials section, the bulk of our experiments in optical trapping consists in pursuing the implementation of static, dual beam optical traps. Figure 6.19 below shows the results from one of our most representative experiments. Although stable traps were not successfully implemented, we did observe weak trapping action generated by the structured light fields.



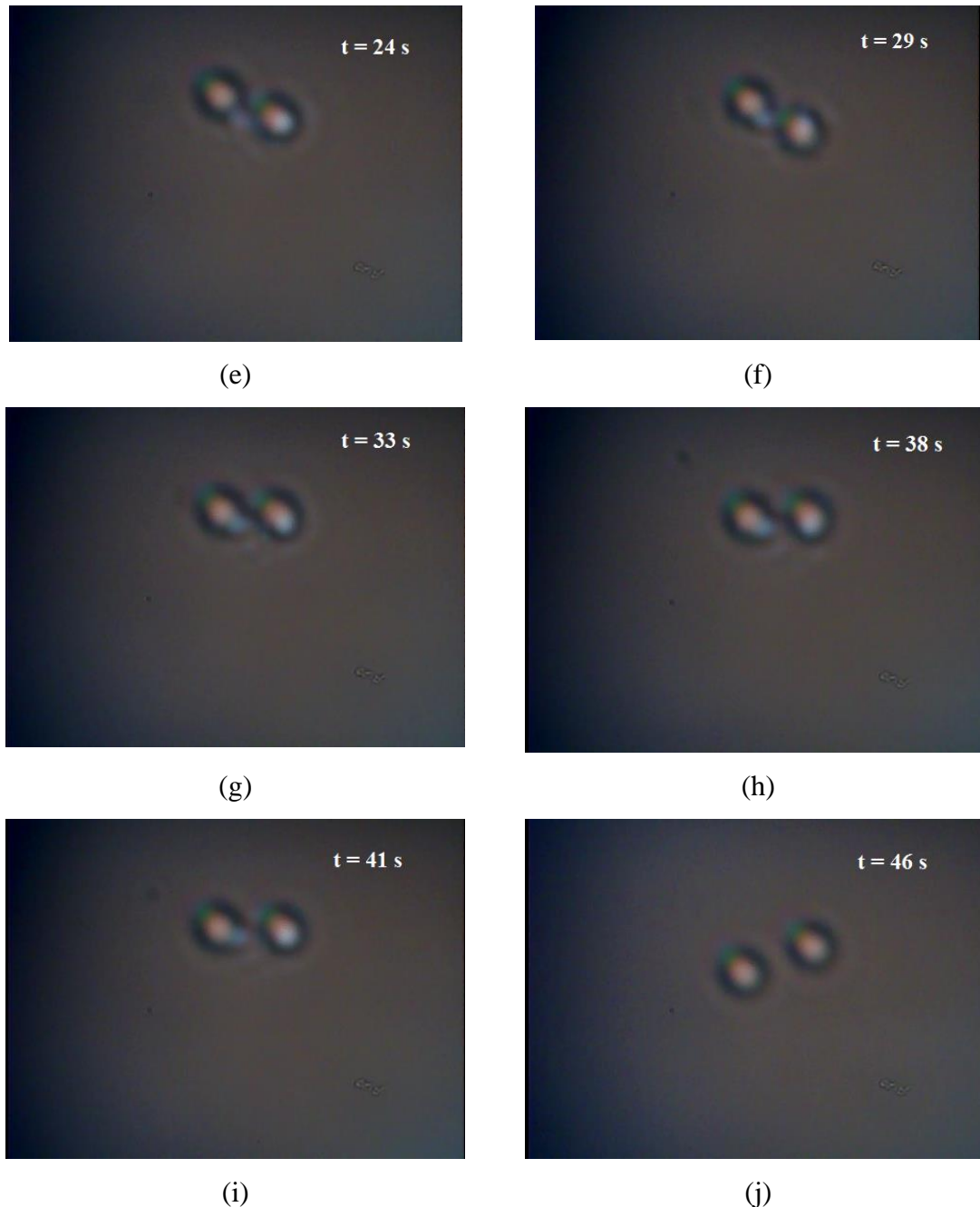


Figure 6.19. Implementation of weak trapping of two  $2\ \mu\text{m}$  beads. The trapping laser is turned off from (a)-(c). After laser turn-on, the beads slowly align with the trapping field in (d)-(i). The laser is turned off again and the beads dissipate in the sample through Brownian motion.

The image sequence in Figure 6.20 shows the effect of the pulling force of the trap in a slightly shorter time scale than that shown above. In this experiment, the orientations of the half waveplate and the polarizer (HWP and P, respectively, in Figure 5.11) were slightly adjusted in order to increase the intensity of the field. Thus, the appearance of the halo around the trapping patterns. Upon turning on the laser, the effect of the trapping field can be more readily seen on the particle on the left:

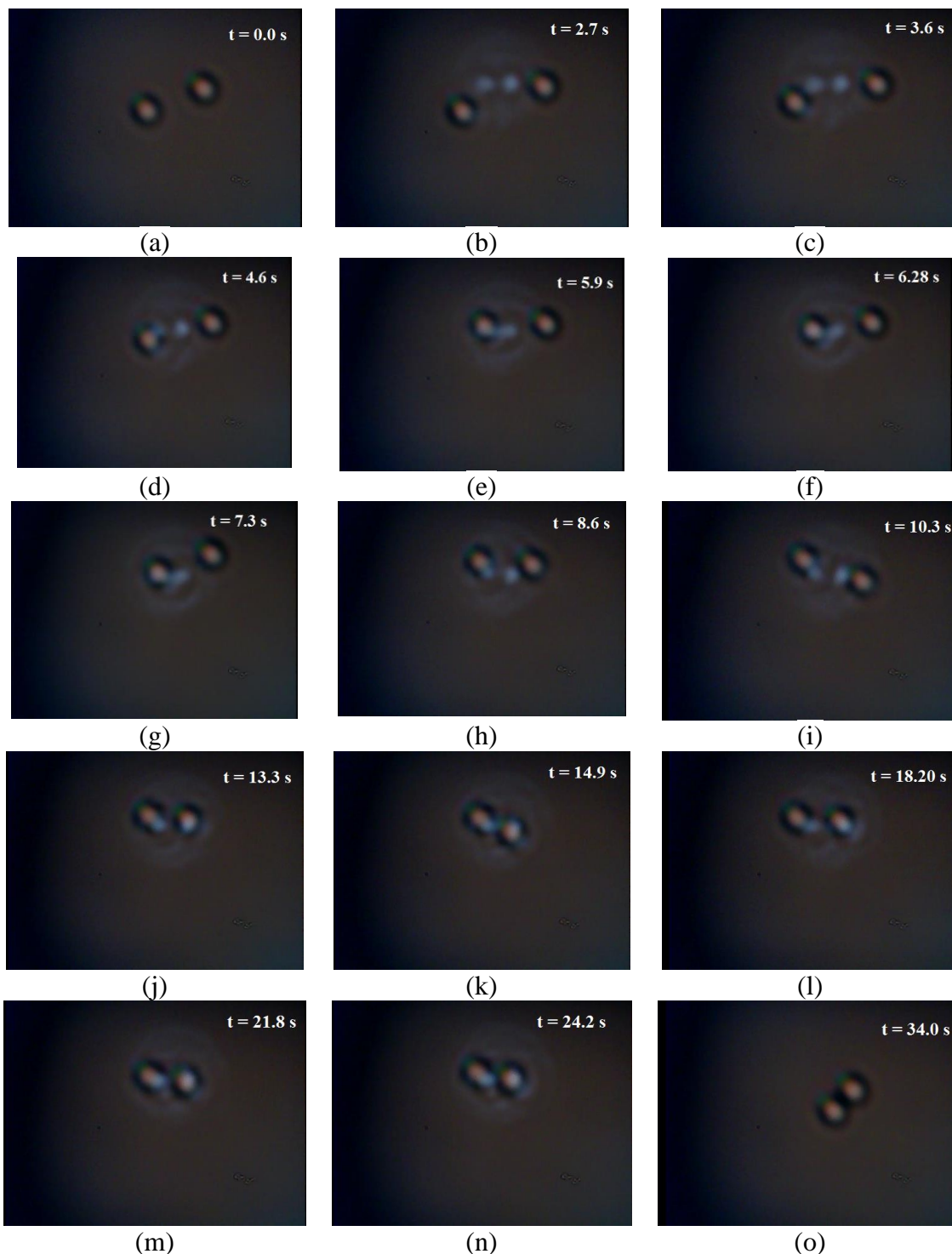


Figure 6.20. Response of two  $2\ \mu\text{m}$  particles to dual trapping field. (a) Laser is off at  $t = 0.0$  s. Upon turning on the laser, the particle on the left is pulled towards the trapping field in (b)-(g). Though unstably trapped, both particles maintain their overall positions (i)-(n) until the laser is turned off at (o).

The results shown in Figures 6.19 and 6.20 were obtained at a measured laser power in the sample plane ranging from 3.0 to 3.5 mW. This implies that each trap was operating in the vicinity of 1.5 mW. Referring to our qualitative analysis in Figure 6.3, a trap operating in

this power range is constant, albeit with significant jitter. The obtained results agree with this analysis.

In an attempt to further increase the power density of our laser, we integrated into our system a 2x beam reducer composed of a 150 mm EFL biconvex lens and a -75 mm EFL concave lens in a reverse Galilean beam expander configuration. This two-lens setup was placed at the output of the laser collimator COL (see Figure 5.11). Unfortunately, the narrowing of the Gaussian intensity distribution of the beam resulted in the formation of a ghost trap by undiffracted light from the LCTV. This beam reducer was consequently removed.

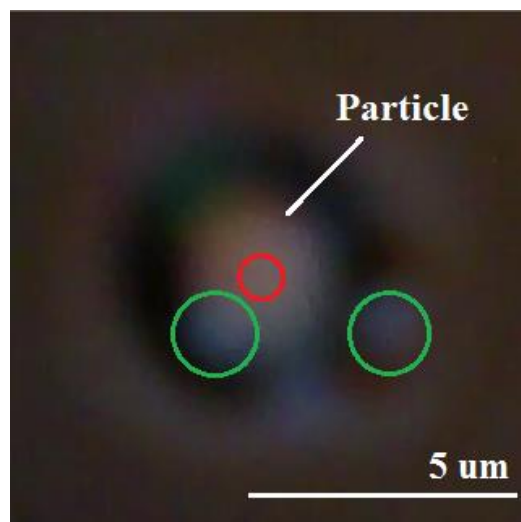


Figure 6.21. Ghost trap (in red) resulting from narrowing of Gaussian distribution of trapping laser. The green circles denote the location of the fields generated by the zero order phase contrast technique.

In the following chapter, we compare our results to the literature. We also discuss the overall efficiency of our system, and finally conclude our project.

## 7 DISCUSSION AND CONCLUSIONS

This chapter presents the discussion of the results obtained from the integration of the zero order phase contrast technique into an optical trapping system. We treat the limitations of our experiment and the steps taken to minimize them. Finally, we present our conclusions and perspectives for future development of this work.

### 7.1. Discussion

A review of optical trapping theory, followed by the careful consideration of several parameters during the implementation of the single-beam systems, such as preparation of the samples, alignment of the sample and laser focus planes, and the optimization of the optics used in the system (e.g. lenses, filters, etc.) facilitated the subsequent implementation of the multi-beam trapping system in this work. Moreover, the results obtained in Section 6.3 show that a properly characterized and aligned zero order phase contrast system is capable of producing high-contrast images that can subsequently be coupled into a microscope path in order to generate multi-beam optical traps, which, as shown on Section 6.4, were successfully implemented in this master's project. Nevertheless, there are several experimental parameters that can be optimized in order to improve the overall quality of the system, which could potentially graduate our proof-of-principle approach into a more practical one. With this in mind, we start by evaluating the total efficiency of our system. With the trapping laser operating at a full power of 300.0 mW, and a measured power at the sample plane of 3.0-3.5 mW, the overall efficiency of our system is around 1.0%, which is clearly very low, compared to other techniques published in the literature (Liesener et al., 2000; Eriksen et al., 2002b). For example, in (Eriksen et al. 2002b), the authors estimated an efficiency of 35% in their system, which implemented multiple stable optical traps using the GPC technique. Several attempts were made towards improving not only the efficiency of our system, but the optical quality of the obtained results, as well. The first significant change in the early stages of our experiments consisted of increasing the power input. Several lasers were tested, starting with a 532 nm diode-pumped solid state (DPSS) laser with a power output of 40.0 mW.

Nevertheless, after some tests, it became clear that a more powerful laser was needed. We were able to test a 976 nm, 300 mW butterfly semiconductor laser with successful results in single optical trapping. However, the lack of temperature control of the device made it unsuitable for use in the zero order optical trapping system, given that power fluctuations can lead to temporal fluctuation in the optical trap stiffness (Neuman; Block, 2004). Finally, we were able to secure the laser that was ultimately used in our experiments, which is temperature controlled, maximizing the power stability of the structured light fields.

The optical losses in our experiment are rather difficult to improve. Following the optical path of our system (see Figure 5.11), the next component with significant transmission loss is the half waveplate (HWP). Although the expected transmission loss from this component was expected to be around 10% due to the inherent transmission characteristics of calcite, the measured loss was closer to 40%. This very significant loss was most likely due to mechanical truncation of the beam from the size of the optic and mounting mechanism. Unfortunately, this component was indispensable and thus could not be removed or replaced by another optic. Further down the optical path, iris Ir1, placed in front of the LCTV, acts as a mask that aids in the removal of intensity noise at the sample plane that results from the phase contrast nature of the experiments. Given that only a small area of the LCTV was modulated with the trapping projections, the aperture diameter of the iris was set to 4.0 mm. Comparatively, the aperture set in the experiments by Eriksen et al. (2002a) was set to 2.0 mm in diameter. This resulted in an additional optical loss near 50%, which obviously constitutes a very significant loss. However, this component greatly enhances contrast intensity in the trapping plane, as halo light can generate unwanted interactions with the particles. Moreover, the most significant loss in our experiment comes from diffraction losses in the LCTV. After the laser light travels through the LCTV and is filtered by the zero order filter ZOF, the optical loss can be as high as 70%, depending on the phase distribution projected onto the LCTV. One way to improve the optical performance of this segment of our system would be by using an optically-addressed SLM, which features increased efficiency. For example, Grier and Roichman (2006) used an SLM in their holographic trapping experiments, which, according to the manufacturer (P/N X8267, Hamamatsu Photonics K.K., Japan), can reach up to 70% diffraction efficiency. Finally, given that most microscope objectives are designed for operation in the visible wavelength range, their transmission in the near infrared range is rather low. In our experiments, the measured transmission for our 100X objective around

64%. All of these optical losses, plus fractional losses due to the lenses and the mirrors in the system, account for the low efficiency of the system.

Regardless of the low the efficiency of our system, the intensity distributions obtained in the trapping plane of our optical setup should, according to the literature, be able to generate strong enough fields for stable optical trapping. Eriksen et al. (2002b) implemented a 4 x 4 array of optical traps, each at a laser power of 1.3 mW, and Curtis et al. (2002) implemented multi-beam HOT arrays with each trap powered at 1 mW. Consequently, we performed numerous tests involving the size and separation of the phase patterns projected onto the LCTV in an attempt to improve the quality of our traps, with mixed results. We found that dot sizes below nine pixels yield very poor contrast in the trapping plane, resulting in little to no interaction between the fields and the particles. Conversely, larger dot sizes appear to restrict particles in the trapping field to the edges, without any apparent gradient force action. These effects were observed not only with the dual phase modulation patterns used for most of our experiments, but with single, triple, and quadruple patterns, as well. Although it would need to be further investigated, we suspect that image distortion due to phase noise introduced by the polarizer in the system, for example, and loss of sharpness due to spherical aberration introduced by the singlet lenses in the optical path, adversely affected the quality of the trapping distributions.

## 7.2 Conclusions and Future Perspectives

To the best of our knowledge, this master's project constitutes the first implementation of an optical trapping system using the zero order phase contrast technique. Although much work needs to be done in order to make the system a practical tool in optical trapping, we were able to implement it as a proof of principle in our lab.

All the objectives we set out to accomplish were met in this project. The implementation of a single optical trapping system, followed by the careful characterization of the LCTV and the implementation of a system based on the zero order phase contrast theory were instrumental in achieving good results in our trapping experiments.

There is ample room in our experimental setup for improvements. Fractional optical losses can significantly be reduced by the use of anti-reflection coated lenses for the near infrared, and better phase performance should be achieved by a half waveplate with central wavelength in or near 976 nm. In fact, there are commercially-available achromatic waveplates in this range. Moreover, higher extinction ratio polarizers can also be found in the market. In addition, liquid crystal devices are continually improving their modulation range and diffraction efficiency performance specifications. As a result, an improved system might be able to overcome some, if not all, of the limitations of holographic trapping and maybe even generalized phase contrast systems discussed in this work.

Upon improving the trapping characteristics of the optical setup, a zero order phase contrast optical trapping system might be used to implement static arrays of optical traps of different sizes, which can be used to sort particles based on their affinity to the different structured fields. A dynamic trapping system would further increase the number of plausible applications, especially in biology, where optical trapping is a commonly used tool. Intracellular surgery, individual microbe selection, and *in vitro* fertilization are some of the myriad of applications for optical trapping (Grier, 2003). Therefore, a Fourier optics technique such as the zero order phase contrast technique could prove very useful in the development and implementation of such valuable, cutting-edge applications.

**BIBLIOGRAPHY**

APPLEYARD, D. et al. Optical trapping for undergraduates. **American Journal of Physics**, v. 75, n. 1, p. 5-14. ISSN 0002-9505. 2007.

ASHKIN, A. et al. Observation of a single-beam gradient force optical trap for dielectric particles. **Optics Letters**, v. 11, n. 5, p. 288-290. 1986.

ASHKIN, A. Acceleration and trapping of particles by radiation pressure. **Physical Review Letters**, v. 24, n. 4, p. 156. ISSN 0031-9007. 1970.

BANYAL, R.; PRASAD, B. Pixel size and Pitch measurements of liquid crystal spatial light modulator by optical diffraction. **Pramana-Journal of Physics**, v. 65, n. 2, p. 291-296. ISSN 0304-4289. 2005.

BAÑAS, A. et al. GPC: recent developments. **Opt. Data Process. Storage**. V.1. p. 22-37. 2015.

BLOCK, S. Making light work with optical tweezers. **Nature**, v. 360, n. 6403, p. 493-495. ISSN 0028-0836. 1992.

BRACEWELL, R.N. The Fourier Transform and Its Applications. Third Edition. **McGraw-Hill**. 2000.

COOLEY, J.; TUKEY, J. An algorithm for machine calculation of complex Fourier series. **Mathematics of Computation**, v. 19, n. 90, p. 297-301. 1965.

CURTIS, J.E.; KOSS, B.A.; GRIER, D.G. Dynamic holographic optical tweezers. **Optics Communications**. v. 207, n. 1-6, p. 169-175. 2002.

DUFFEY, J. N.; JONES, B. Evaluation of the InFocus TVT-6000 LCTV. **SPIE Optical Pattern Recognition V**, v. 2237. 1994.

DUFRESNE, E.; GRIER, D. Optical tweezer arrays and optical substrates created with diffractive optics. **Review of Scientific Instruments**, v. 69, n. 5, p. 1974-1977. ISSN 0034-6748. 1998.

DUFRESNE, E. et al. Computer-generated holographic optical tweezer arrays. **Review of Scientific Instruments**, v. 72, n. 3, p. 1810-1816. ISSN 0034-6748. 2001.

ERIKSEN, R.; MOGENSEN, P.; GLUCKSTAD, J. Multiple-beam optical tweezers generated by the generalized phase-contrast method. **Optics Letters**, v. 27, n. 4, p. 267-269. 2002a.

ERIKSEN, R.L.; DARIA, V.R.; GLUCKSTAD, J. Fully dynamic multiple-beam optical tweezers. **Optics Express**. v. 10, n. 14, p. 597-602. 2002b.

FALLMAN, E.; AXNER, O. Design for fully steerable dual-trap optical tweezers. **Applied Optics**, v. 36, n. 10, p. 2107-2113. ISSN 0003-6935. 1997.

- FRIESE, M. et al. Optical angular-momentum transfer to trapped absorbing particles. **Physical Review a**, v. 54, n. 2, p. 1593-1596. 1996.
- GERCHBERG, R.W.; SAXTON, W. Practical algorithm for determination of phase from image and diffraction plane pictures. **Optik**, v. 35, n. 2, p. 237-246. 1972.
- GRIER, D. G. A revolution in optical trapping. **Nature**, v. 424. 2003.
- GRIER, D.; ROICHMAN, Y. Holographic optical trapping. **Applied Optics**, v. 45, n. 5, p. 880-887, FEB 10. ISSN 1559-128X. 2006.
- GLÜCKSTAD, J.; MOGENSEN, P.C., ERIKSEN, R.L. New phase contrast methods for optical processing. **Optical Pattern Recognition XIII**. Proceedings of SPIE. v. 4734. 2002.
- GLÜCKSTAD, J.; PALIMA, D. Generalized phase contrast: applications in optics and photonics. **Canopus Academic Publishing Limited**. United States. 2009.
- GOODMAN, J. Introduction to Fourier Optics. Roberts and Company Publishers; 3rd Edition edition. 2004.
- HECHT, E. Optics. 4<sup>th</sup> Edition. San Francisco: **Addison Wesley**. 2002.
- LANG, M.; BLOCK, S. Resource letter: LBOT-1: Laser-based optical tweezers. **American Journal of Physics**, v. 71, n. 3, p. 201-215. ISSN 0002-9505. 2003.
- LIESENER, J. et al. Multi-functional optical tweezers using computer-generated holograms. **Optics Communications**, v. 185, n. 1-3, p. 77-82. ISSN 0030-4018. 2000.
- MACDONALD, M. et al. Creation and manipulation of three-dimensional optically trapped structures. **Science**, v. 296, n. 5570, p. 1101-1103. ISSN 0036-8075. 2002.
- MAZOLLI, A.; MAIA NETO P.A.; NUSSENZVEIG H.M. Theory of trapping forces in optical tweezers. **Proceedings. R. Soc. Lond. A**, v.459, p. 3021–3041. 2003.
- NEFF, J.; ATHALE, R.; LEE, S. Two-dimensional spatial light modulators - a tutorial. **Proceedings of the IEEE**, v. 78, n. 5, p. 826-855. 1990.
- NETO, L. Optical real-time holograms using liquid crystal television and computer iterative design. **Doctoral Thesis**. Faculté des Sciences et Génie, Université Laval, Canada. 1995.
- NETO, L.; ROBERGE, D.; SHENG, Y. Full-range, continuous, complex modulation by the use of two coupled-mode liquid-crystal televisions. **Applied Optics**, v. 35, n. 23, p. 4567-4576. 1996.
- NETO, L. G. Implementation of image encryption using the phase-contrast technique. **SPIE**, v. 3386, n. 0277-786X. 1998.
- NETO, L. G. et al. Implementation of Fresnel full complex-amplitude digital holograms. **Optical Engineering**, v. 43, n. 11, p. 2640-2649. 2004.
- NEUMAN, K.; BLOCK, S. Optical trapping. **Review of Scientific Instruments**, v. 75, n. 9, p. 2787-2809. 2004.

NICHOLS, E.; HULL, G. A preliminary communication on the pressure of heat and light radiation. **Physical Review**, v. 13, n. 5, p. 307-320. ISSN 0031-899X. 1901.

NIEMINEN, T. et al. Numerical modelling of optical trapping. **Computer Physics Communications**, v. 142, n. 1-3, p. 468-471. ISSN 0010-4655. 2001.

NIEMINEN, T.; RUBINSZTEIN-DUNLOP, H.; HECKENBERG, N. Calculation of the T-matrix: general considerations and application of the point-matching method. **Journal of Quantitative Spectroscopy & Radiative Transfer**, v. 79, p. 1019-1029. ISSN 0022-4073. 2003.

NIEMINEN, T. et al. Physics of optical tweezers. **Laser Manipulation of Cells and Tissues**, v. 82, p. 207-236. ISSN 0091-679X. 2007a.

NIEMINEN, T. et al. Optical tweezers computational toolbox. **Journal of Optics a-Pure and Applied Optics**, v. 9, n. 8, p. S196-S203. ISSN 1464-4258. 2007b.

OGURA, Y.; KAGAWA, K.; TANIDA, J. Optical manipulation of microscopic objects by means of vertical-cavity surface-emitting laser array sources. **Applied Optics**, v. 40, n. 30, p. 5430-5435. ISSN 1559-128X. 2001.

PADGETT, M. J.; MOLLOY, J. E.; MCGLOIN, D. **Optical tweezers: methods and applications**. United States: Taylor and Francis Group, LLC. ISBN 978-1-4200-7412-3. 2010.

PIZOLATO JR., J.C. Novas técnicas de contraste de fase para a verificação de padrões cifrados. **Tese (Doutorado)** – Escola de Engenharia de São Carlos, Universidade de São Paulo, São Carlos, 2006.

PIZOLATO, J. et al. Zeroth-order phase-contrast technique. **Applied Optics**, v. 46, n. 31, p. 7604-7613. 2007.

PIZOLATO, J.; NETO, L. Phase-only optical encryption based on the zeroth-order phase-contrast technique. **Optical Engineering**, v. 48, n. 9. ISSN 0091-3286. 2009.

POLIN, M. et al. Optimized holographic optical traps. **Optics Express**, v. 13, n. 15, p. 5831-5845. ISSN 1094-4087. 2005.

SALEH, B.E.A.; TEICH, M.C. **Fundamentals of Photonics**. New York: **Wiley**. 1991.

SOUTAR, C.; MONROE, S. E.; KNOPP, J. Complex characterisation of the Epson liquid crystal television. **SPIE Optical Pattern Recognition IV**, v. 1959. 1993.

SOUTAR, C.; LU, K. Determination of the physical-properties of an arbitrary twisted-nematic liquid-crystal cell. **Optical Engineering**, v. 33, n. 8, p. 2704-2712. ISSN 0091-3286. 1994.

VISSCHER, K.; BRAKENHOFF, G.; KROL, J. Micromanipulation by multiple optical traps created by a single fast scanning trap integrated with the bilateral confocal scanning laser microscope. **Cytometry**, v. 14, n. 2, p. 105-114. ISSN 0196-4763. 1993.

VISSCHER, K.; GROSS, S.; BLOCK, S. Construction of multiple-beam optical traps with nanometer-resolution position sensing. **Ieee Journal of Selected Topics in Quantum Electronics**, v. 2, n. 4, p. 1066-1076. ISSN 1077-260X. 1996.

WANG, M. et al. Stretching DNA with optical tweezers. **Biophysical Journal**, v. 72, n. 3, p. 1335-1346. ISSN 0006-3495. 1997.

WOERDEMANN, M. Structured light fields. Applications in optical trapping, manipulation, and organization. **Doctoral thesis**. University of Münster, Germany. Springer. ISBN 978-3-642-29322-1. 2012.

ZERNIKE, F. How I discovered phase contrast. **Science**, v. 121, n. 3141, p. 345-349. ISSN 0036-8075. 1955.

## APPENDIX 1: PROJECTION OF A FRAUNHOFER DIFFRACTION PATTERN USING A FOURIER LENS

In this section, we explain how positive lenses act as operators in the optical implementation of the Fourier transform of a light distribution. Starting with the Huygens-Fresnel principle, we derive an expression the light distribution in the back focal plane of a lens  $U_f$  as a function of the input field.

### A.1. Mathematical Expression of the Huygens-Fresnel Principle

Diffraction occurs whenever the amplitude and phase characteristics of a segment of a wavefront (sound, matter, or light) change when obstructed by an obstacle. The various segments of a wave that propagate beyond an obstacle interfere, creating a particular energy-density distribution known as the diffraction pattern (Hecht, 2002).

The first steps in establishing a theoretical basis for diffraction were taken by the Dutch mathematician Christian Huygens, in his proposal concerning the wave theory of light in 1678. Huygens expressed that if each unobstructed point of a wavefront of a disturbance is considered at a given instant to be a source of secondary wavelets, then the wavefront at a later instant can be found by the superposition, or envelope, of such secondary wavelets (Hecht, 2002; Goodman, 2004).

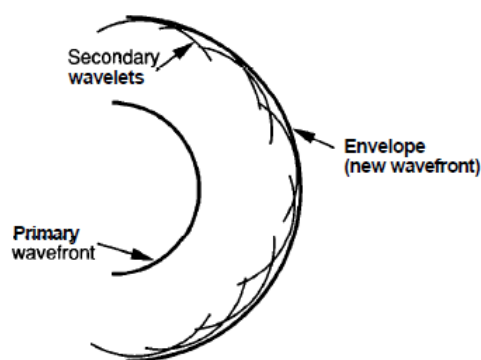


Figure A.1. Huygens envelope construction of secondary wavelets originated from a primary wavefront (Goodman, 2004).

Considering the diffraction geometry in Figure A.2, the Huygens-Fresnel principle can be mathematically stated as follows:

$$U(P_0) = \frac{1}{j\lambda} \iint_{\Sigma} U(P_1) \frac{\exp(jkr_{01})}{r_{01}} \cos \theta \, ds \quad (\text{A.1})$$

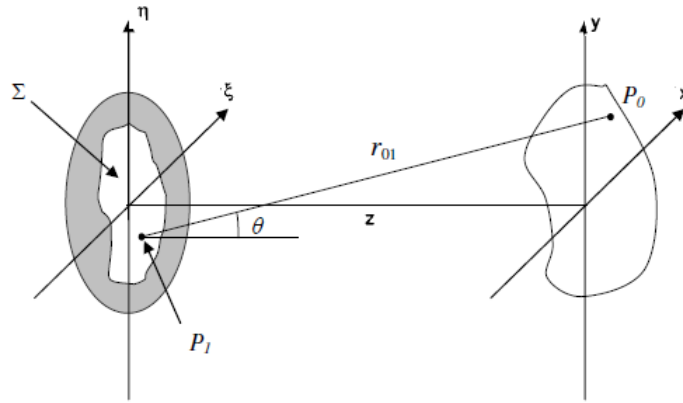


Figure A.2. Diffraction geometry used to define the Huygens-Fresnel principle (Goodman, 2004).

In Equation A.1,  $U(P_1)$  and  $U(P_0)$  represent the complex distributions at the input of the diffractive element, and after propagation through distance  $z$ , respectively.

Furthermore, we can define  $\cos\theta = z/r_{01}$  and

$$r_{01} = \sqrt{z^2 + (x - \xi)^2 + (y - \eta)^2} . \quad (\text{A.2})$$

Thus, we can rewrite the Huygens-Fresnel principle as follows:

$$U(x, y) = \frac{z}{j\lambda} \iint_{\Sigma} U(\xi, \eta) \frac{\exp(jkr_{01})}{r_{01}^2} d\xi d\eta . \quad (\text{A.3})$$

## A.2. The Fresnel Approximation

In order to reduce the Huygens-Fresnel principle, we can apply approximations to the expression for  $r_{01}$ , the distance between  $P_0$  and  $P_1$ . By factoring out  $z$  in (Eq. A.2) and considering only the first and second terms in the binomial expansion of the square root, we arrive at the following approximation [3]:

$$r_{01} \approx z \left[ 1 + \frac{1}{2} \left( \frac{x-\xi}{z} \right)^2 + \frac{1}{2} \left( \frac{y-\eta}{z} \right)^2 \right]. \quad (\text{A.4})$$

By retaining all the terms in this approximation and incorporating it into Eq. 3.15, and applying some mathematical manipulation, we arrive at the Fresnel diffraction integral:

$$U(x, y) = \frac{e^{jkz}}{j\lambda z} e^{j\frac{k}{2z}(x^2+y^2)} \iint_{-\infty}^{\infty} \left\{ U(\xi, \eta) e^{j\frac{k}{2z}(\xi^2+\eta^2)} \right\} e^{-j\frac{2\pi}{\lambda z}(x\xi+\eta y)} d\xi d\eta . \quad (\text{A.5})$$

A quick analysis of Eq. A.5 leads us to recognize that, aside from the multiplicative factors,  $U(x,y)$  is the Fourier transform of the product of the complex field just to the right of the aperture and a quadratic phase exponential. Thus, this approximation is valid in the *near field* of the aperture.

### A.3. The Fraunhofer Approximation

If we apply one further approximation to the Fresnel diffraction integral (A.5), namely

$$z \gg \frac{k(\xi^2+\eta^2)_{max}}{2}, \quad (\text{A.6})$$

we have that the multiplicative phase term inside the integral is approximately equal to unity, and, without taking into account the phase factor to the left of the integral, the field  $U(x,y)$  results directly from the Fourier Transform of the aperture distribution [3]:

$$U(x, y) = \frac{e^{jkz}}{j\lambda z} e^{j\frac{k}{2z}(x^2+y^2)} \iint_{-\infty}^{\infty} U(\xi, \eta) e^{-j\frac{2\pi}{\lambda z}(x\xi+\eta y)} d\xi d\eta . \quad (\text{A.7})$$

A fundamental result of this approximation is that in the region of *Fraunhofer diffraction*, the observation distance  $z$  must be much larger than 1,600 meters (Goodman, 2004). By incorporating a lens into the imaging system, this distance can be greatly reduced, allowing, in our case, for object reconstruction in a location a few centimeters from the hologram plane.

### A.4. Projection of a Fraunhofer Diffraction Pattern using a Fourier Lens

Let us consider the case of Fig. A.3 in which the transmissive diffractive element is located in front of the lens:

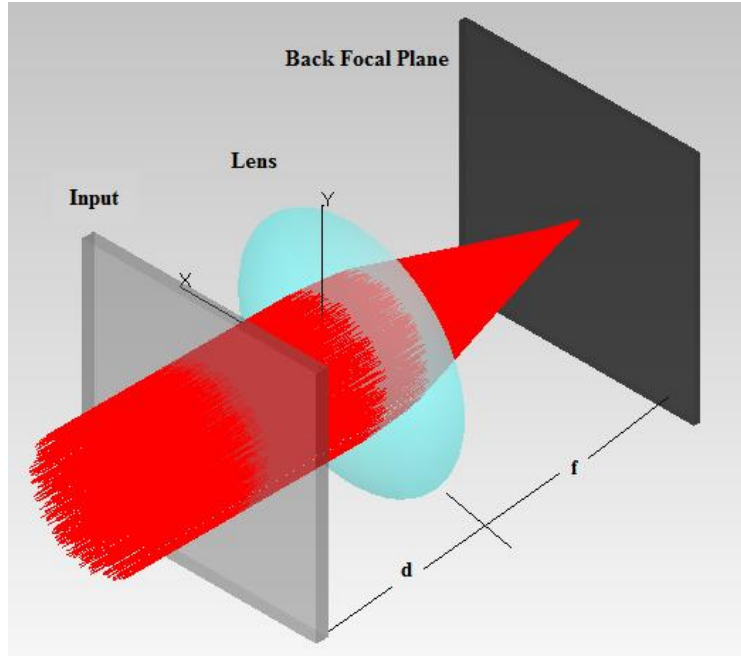


Figure A.3. Optical path with diffractive element located a distance  $d$  in front of lens.

Furthermore, let us define the following parameters:

$t_A \equiv$  amplitude transmittance of the input

$A \equiv$  amplitude of incident plane wave

$F_0(f_X, f_Y) \equiv$  Fourier spectrum of light transmitted by the DE

$F_l(f_X, f_Y) \equiv$  Fourier spectrum of light incident on lens  $U_l$

$U_f \equiv$  light distribution in back focal plane of lens

Thus, we have that

$$F_0(f_X, f_Y) = \mathcal{F}\{At_A\} \text{ and } F_l(f_X, f_Y) = \mathcal{F}\{U_l\} .$$

Now, assuming that the Fresnel approximation (A.5) is valid over the distance  $d$ , and dropping a constant phase delay factor, we can relate  $F_0$  and  $F_l$  as follows (Goodman, 2004):

$$F_l(f_X, f_Y) = F_0(f_X, f_Y) \exp[-j\pi\lambda d(f_X^2 + f_Y^2)] . \quad (\text{A.8})$$

Our goal is to define the disturbance  $U_f$  in the back focal plane of the lens in terms of the input parameters. To that end, we need to define another parameter,  $U_l'$ , the amplitude distribution behind the lens:

$$U'_l(x, y) = U_l(x, y)P(x, y)\exp\left[-j\frac{k}{2f}(x^2 + y^2)\right]. \quad (\text{A.9})$$

In Eq. A.9 above, the function  $P$  is the pupil function, which we shall equate to 1, and the exponential term is the phase transformation factor resulting from the presence of the thin lens in the optical path.

Considering again the Fresnel approximation equation (A.5), with  $U_f$  located in the  $u$ - $v$  coordinates ( $f_x = u/\lambda f$  and  $f_y = v/\lambda f$ ), and  $z = f$ , we have the following:

$$U_f(u, v) = \frac{\exp\left[j\frac{k}{2f}(u^2 + v^2)\right]}{j\lambda f} F_l\left(\frac{u}{\lambda f}, \frac{v}{\lambda f}\right). \quad (\text{A.10})$$

Substituting Eq. A.8 into Eq. A.10, we arrive at the following equation for  $U_f$ :

$$U_f(u, v) = \frac{A\exp\left[j\frac{k}{2f}\left(1 - \frac{d}{f}\right)(u^2 + v^2)\right]}{j\lambda f} \iint_{-\infty}^{\infty} t_A(\xi, \eta) \exp\left[-j\frac{2\pi}{\lambda f}(\xi u + \eta v)\right] d\xi d\eta. \quad (\text{A.11})$$

The Fourier transform of a function  $g(x, y)$  can be defined as follows:

$$\mathcal{F}\{g(x, y)\} = \iint_{-\infty}^{\infty} g(x, y) \exp\left[-j2\pi(f_x x + f_y y)\right] dx dy, \quad (\text{A.12})$$

We see from A.11 that if we let the distance  $d$  from the diffractive element to the lens equal the focal length of the lens  $f$ , then the phase curvature introduced by the exponential factor to the left of the integral above disappears, yielding an exact Fourier transform relation between the input transmittance and the disturbance in the back focal plane of the lens. Thus, we can conclude that the presence of the lens facilitates the projection of the Fraunhofer diffraction pattern.



## APPENDIX 2: JONES MATRIX CALCULUS OF A LIQUID CRYSTAL CELL

*Jones calculus* is a mathematical tool that facilitates the characterization of polarization-sensitive devices through the implementation of matrix operations. The output polarization of the device can be described by a 2 x 2 Jones matrix, so that it is related to the input polarization vector through the following equation (Goodman, 2004):

$$\vec{U}' = L\vec{U} = \begin{bmatrix} l_{11} & l_{12} \\ l_{21} & l_{22} \end{bmatrix} \vec{U}. \quad (\text{A.13})$$

The Jones matrix  $W_0$  of a single slice of an LC cell with  $N$  slices can be represented with the following matrix of an optical retarder:

$$W_0 = \begin{bmatrix} e^{j\frac{2\pi}{\lambda}n_e\frac{d}{N}} & 0 \\ 0 & e^{j\frac{2\pi}{\lambda}n_o\frac{d}{N}} \end{bmatrix}. \quad (\text{A.14})$$

Defining  $\phi$  as

$$\phi = \frac{\pi}{\lambda}d(n_e + n_o), \quad (\text{A.15})$$

and substituting  $\phi$  and  $\beta$  into Equation A.14, we get a more compact definition for  $W_0$ :

$$W_0 = e^{j\frac{\phi}{N}} \begin{bmatrix} e^{j\frac{\beta}{N}} & 0 \\ 0 & e^{-j\frac{\beta}{N}} \end{bmatrix} = e^{j\frac{\phi}{N}} W_L, \quad (\text{A.16})$$

where  $W_L$  is the matrix multiplying the exponential term  $e^{j\frac{\phi}{N}}$ .

The complete effect of the LC cell on incident light can be represented by a Jones matrix that uses a coordinate rotation operator to align the x-axis with the long axis of the LC molecules, a retardation matrix, followed by a second rotation matrix, which returns the x-axis to its original orientation with respect to the long axis of the molecules.

Defining  $\varphi$  as the angle between two coordinate systems, we can represent the rotator operator  $R[\varphi]$  as follows:

$$R[\varphi] = \begin{bmatrix} \cos\varphi & \sin\varphi \\ -\sin\varphi & \cos\varphi \end{bmatrix}. \quad (\text{A.17})$$

Thus, the Jones matrix  $M$  for an LC cell of  $N$  slices can be defined as

$$M = \prod_{m=1}^N R\left(-m\frac{\theta}{N}\right) W_0 R\left(m\frac{\theta}{N}\right). \quad (\text{A.18})$$

Furthermore, using the rotator identity  $R[a]R[b]=R[a+b]$  and the definition for  $W_L$ , we can simplify Equation A.18 as follows:

$$M = e^{j\phi} R[-\theta] \left[ W_L R\left[\frac{\theta}{N}\right] \right]^N. \quad (\text{A.19})$$

Expanding the results for each of the terms in Equation A.19, we get the following expression for  $M$ :

$$M = e^{j\phi} \begin{bmatrix} \cos\theta & -\sin\theta \\ \sin\theta & \cos\theta \end{bmatrix} \begin{bmatrix} \cos\left(\frac{\theta}{N}\right) e^{j\frac{\beta}{N}} & \sin\left(\frac{\theta}{N}\right) e^{j\frac{\beta}{N}} \\ -\sin\left(\frac{\theta}{N}\right) e^{-j\frac{\beta}{N}} & \cos\left(\frac{\theta}{N}\right) e^{-j\frac{\beta}{N}} \end{bmatrix}^N. \quad (\text{A.20})$$

The equation above can be further simplified by applying the *Chebyshev identity*:

$$\begin{bmatrix} a & b \\ c & d \end{bmatrix}^N = \begin{bmatrix} \frac{a \sin(Nk) - \sin[(N-1)k]}{\sin(Nk)} & b \frac{\sin(Nk)}{\sin(k)} \\ c \frac{\sin(Nk)}{\sin(k)} & \frac{d \sin(Nk) - \sin[(N-1)k]}{\sin(Nk)} \end{bmatrix}, \quad (\text{A.21})$$

where  $k = \cos^{-1}((a+d)/2)$ .

Applying this identity to Equation A.20, we have the following result for  $M$ :

$$M = e^{j\phi} \begin{bmatrix} \cos\theta & -\sin\theta \\ \sin\theta & \cos\theta \end{bmatrix} \begin{bmatrix} \cos\gamma + \frac{j\beta \sin\gamma}{\gamma} & \frac{\theta}{\gamma} \sin\gamma \\ -\frac{\theta}{\gamma} \sin\gamma & \cos\gamma - \frac{j\beta \sin\gamma}{\gamma} \end{bmatrix}, \quad (\text{A.22})$$

where  $\gamma$  is defined as

$$\gamma = \sqrt{\theta^2 + \beta^2}. \quad (\text{A.23})$$